Exploration of Earth's Deep Interior by Merging Nanotechnology, Diamond-Anvil Cell Experiments, and Computational Crystal Chemistry

Dissertation

Presented in Partial Fulfillment of the Requirements for the Degree Doctor of Philosophy in the Graduate School of The Ohio State University

By

Jeffrey Scott Pigott, M.S.

Graduate Program in Geological Sciences

The Ohio State University

2015

Dissertation Committee:

Professor Wendy R. Panero, Advisor

Professor W. Berry Lyons

Professor Michael Barton

Professor David R. Cole

Abstract

The structure, dynamics, and composition of Earth's deep interior have direct control on plate tectonics and surface-to-interior exchange of material, including water and carbon. To properly interpret geophysical data of the Earth's interior, accurate and precise measurements of the material properties of the constituent mineral phases are required. Additionally, experimentally derived data need to be augmented by computational chemistry and modeling of physical properties to elucidate the effect of compositional variations and deep storage of volatile components (e.g. H_2O and CO_2) within the crystalline phases.

This dissertation uses *in situ* high pressure, high-temperature experiments in the laser-heated diamond anvil cell (LHDAC) coupled with synchrotron-based x-ray diffraction. The thermal expansion and bulk modulus of Ni and SiO_2 are measured to P = ~110 GPa and T = ~3000 K. Nickel is a significant component of the Earth's core and SiO_2 is the fundamental building block of the Earth's mantle and crust. We have designed the first controlled-geometry samples of Ni and SiO_2, manufactured using nanofabrication techniques, and specifically tuned to reduce systematic errors in the measurement. Knowledge of the thermoelastic properties of Ni and SiO_2 has implications for subduction rates, plume buoyancy, dynamics of the Earth's convective heat engine, and planetary formation. Complimentary to the Ni/SiO_2 experiments, the energetics of

different hydrogen defect mechanisms in garnet ($MgSiO_3$-$Mg_3Al_2Si_3O_{12}$) and associated geophysical properties (P- and S-wave velocities) are calculated using atomistic simulations and first-principles calculations to a depth of 700 km. Garnet accounts for as much as 40 percent of the rock volume at 500 km. By calculating and comparing the defect energies associated with charge-balanced substitutions of hydrogen for magnesium or silicon, the hydrogarnet defect, $[\square_{Si}(OH)_4]^X$, has the lowest energy and is therefore predicted to be the most favorable in the garnet structure. The fundamental question of the planet's water budget has implications for the formation history of the planet and the cycling of volatile compounds between the surface and the interior.

Dedication

For Mary Theresa Pigott

Acknowledgments

I would like to sincerely thank my advisor, Dr. Wendy Panero. I wouldn't have made it to where I am now without Wendy's selfless mentoring and exceptional advising. I would also like to thank my committee members, Berry Lyons, Michael Barton, and David Cole for their friendly discussions and constructive feedback.

I would like to thank the many collaborators that helped to make this dissertation research materialize. In this regard, I would like to express extraordinary gratitude to Daniel Reaman, Kate Wright, Julian Gale, Rebecca Fischer, Ross Hrubiak, Derek Ditmer, Robert Davis, and Yue Meng.

Funding for this research was provided by the grants, NSF EAR: EAR 09-55647, DOE-CDAC-4-3253-04, OSU-IMR-FG0122, and OSC-PAS0238-1 awarded to Wendy Panero. Part of this work was supported by NSF IIA #1308656 and the Australian Academy of Science as part of my East Asia and Pacific Summer Institute fellowship. I would also like to acknowledge support from the Ohio State University Presidential Fellowship, the School of Earth Sciences McCaughey Fellowship, and Friends of Orton Hall fund. Additional thanks goes to CDAC for allocating beamtime for this dissertation research.

I would like to acknowledge the facilities and support staff that enabled this research. Much of this research was performed at HPCAT (Sector 16), Advanced Photon

Source, Argonne National Laboratory and Nanotech West Laboratory at OSU. The FIB/EDS/TEM work was done at the OSU Center for Electron Microscopy and AnalysiS with the technical support of Isabel David, Dan Huber, and Henk Colijn. I would like to thank the Subsurface Energy Materials Characterization & Analysis Laboratory at OSU for use of their SEM and technical support from Julie Sheets and Sue Welch.

I would like to acknowledge Andy Campbell for helpful discussions about LHDAC experiments, Steven T. Goldsmith for his professional mentoring, and my participation in the 2010 CIDER summer program which inspired parts of my research. I also would like to thank Joseph Smyth and three anonymous reviewers for their helpful comments and feedback that served to improve chapters 2 and 4.

Finally, my incredible wife, Mary, deserves special thanks for her unwavering support throughout this endeavor. She has had a deeply profound impact on both my personal and professional life and I truly couldn’t have done this without her.

Vita

June 21st, 1979……..…….……Born – Youngstown, Ohio

June 1997.....Graduated – East Liverpool High School, East Liverpool, Ohio

March 2002..... B.A. Sociology, The Ohio State University, Columbus, Ohio

March 2011……..……...M.S. Earth Sciences, The Ohio State University, Columbus, Ohio

March 2011 – present……..…...Graduate Teaching Associate, Graduate Research Associate, Graduate Fellow, The Ohio State University

Publications

Pigott, J.S., Wright, K., Gale, J.D., and Panero, W.R. (2015), Calculation of the energetics of water incorporation in majorite garnet. American Mineralogist, 100, 1065-1075.

Panero, W.R., Pigott, J.S., Reaman, D.M., Kabbes, J.E., and Liu, Z. (2015) Dry $(Mg,Fe)SiO_3$ Perovskite in Earth's Lower Mantle. Journal of Geophysical Research, 120, 1-15.

Unterborn, C.T., Kabbes, J.E., Pigott, J.S., Reaman, D.M., and Panero, W.R. (2014) The role of carbon in extrasolar planetary dynamics and habitability. The Astrophysical Journal, 793, 10 pages.

Panero, W.R., Smyth, J.R., Pigott, J.S., Liu, Z., and Frost, D.J. (2013) Hydrous ringwoodite to 5 K and 35 GPa: Multiple bonding sites resolved with FTIR spectroscopy. American Mineralogist, 98, 637-642.

Pigott, J.S., Reaman, D.R., and Panero., W.R. (2011) Microfabrication of controlled-geometry samples for the laser-heated diamond-anvil cell using focused ion beam technology. Review of Scientific Instruments, 82, 115106.

Goldsmith, S.T., Carey, A.E., Johnson, B.E., Welch, A.E., Lyons, W.B., McDowell, W.H., and Pigott, J.S. (2010) Stream geochemistry, chemical weathering and CO_2 consumption potential of andesitic terrains, Dominica, Lesser Antilles. Geochemica et Cosmochemica Acta, 74, 85-103.

Fields of Study

Major Field: Geological Sciences

Table of Contents

List of Tables

List of Figures

Chapter 1: Introduction

1.1 Background

The outer shell (~100km) of the Earth is composed of rigid, mobile plates. The movement of these plates is described by the unifying theory of plate tectonics. The motion of the plates is generated by solid-state deformation of the underlying mantle as a result of buoyancy forces arising from density variations due to compositional and thermal heterogeneities. Thermal expansion and compressibility, and the change in these properties with pressure and temperature, dictate the density of materials at the high pressures (P > 10 GPa or >100,000x atmospheric pressure) and high temperatures (T > 1500 K) of planetary interiors. Additionally, water has a first-order effect on the compressibility and deformation of the crust and mantle (e.g., Smyth et al. 2004; Xu et al. 2013). The amount of water stored in deep crustal and mantle rocks is largely unconstrained, and may account for a quantity of water comparable to or in excess of the amount contained in the present oceans (Hirschmann 2006).

Stishovite (SiO_2), majorite ($Mg_4Si_4O_{12}$) and nickel (Ni) are significant components of Earth's interior. Stishovite is stable in subducted oceanic crust below 300 km depth (Irifune and Ringwood 1993). Majorite is the high-pressure garnet phase stable at mid-mantle depths (410–660 km) and is the second most abundant phase after the high-pressure olivine polymorphs (Frost 2008). The Earth's core contains ~5% Ni

alloyed with iron along with some amount of light elements (C, O, Si, S, H) (Birch 1952; Allegre et al. 1995; McDonough and Sun 1995). Therefore, proper interpretation of seismic variations in wave speeds in the deep mantle require accurate knowledge of the relationship between the pressure, volume, and temperature (*P*-*V*-*T*) for major minerals, that is, the equations of state (EOS), of silica and majorite. Furthermore, the EOS of nickel is essential to constrain the density and thus the composition of Earth's core.

High pressures and temperatures can be created through the use of the laser-heated diamond-anvil cell (LHDAC), in which a sample is compressed between the tips of two gem-quality diamonds, and an infrared (IR) laser is passed through each diamond to heat the sample. Mineral physics experiments that combine the LHDAC and synchrotron-based X-ray diffraction (XRD) can be used to experimentally determine the EOS of the constituent minerals of Earth's interior. However, the accuracy of measured thermoelastic properties is limited by spatial and chemical heterogeneities in the sample environment. Errors may be systematic due to steep temperature gradients compounded by the uncertainty of alignment of the laser-heated spot with respect to the x-ray beam (Kavner and Panero 2004).

Majorite garnet synthesized at transition zone pressures and temperatures can contain up to ~700 ppm H_2O (Bolfan-Casanova et al. 2000; Katayama et al. 2003), a quantity sufficient to radically change the deformation characteristics of garnet. Based on the infrared absorption spectra, OH is likely incorporated into majorite by the hydrogarnet defect mechanism (Katayama et al. 2003) in which 4 hydrogen atoms substitute for a Si atom in the tetrahedral site leaving a vacancy (Lager et al. 1989). However, the OH-defect mechanism may be more complex (Williams and Hemley 2001)

based on water concentrations in natural garnet samples brought to the surface from the mantle (Bell and Rossmann 1992) and infrared spectroscopy of both natural garnet (Beran and Libowitzky 2006) and synthetic majorite (Bolfan-Casanova et al. 2000).

1.2 Computational methods

The structure and energetics of charge-balanced hydrogen substitution into $Mg_4Si_4O_{12}$ majorite have been calculated (Chapter 4). By calculating and comparing the defect energies associated with 2 different site substitutions of hydrogen, the most favorable mechanism, that is the one with the lowest energy, can be identified. The reaction energies have been calculated for 2 mechanisms of hydrogen incorporation into the structure; substitution of 2 hydrogen atoms for Mg and substitution of 4 hydrogen atoms for Si. The energies were calculated using classical atomistic simulations implemented in the General Utility Lattice Program (GULP) software (Gale and Rohl 2003) with complementary first-principles calculations using the Vienna Ab Initio Simulation Package (VASP) (Kresse and Furthmüller 1996a, 1996b). Classical atomistic calculations describe the total energy of a system in terms of atomic positions and uses interatomic potential energy functions. VASP is based in quantum mechanical Kohn-Sham density functional theory (DFT) and solves the time-independent Schrödinger equation to find the ground state electron density and compute the total energy. The DFT energy minimizations are static, zero-temperature calculations. The vibrational frequencies are not calculated therefore I do not correct for the zero-point energy, a result of the Heisenberg uncertainty principle.

1.3 Experimental methods development

I established nanofabrication techniques to create samples with 2 different chemistries as a controlled "double-hot plate". In this sample arrangement, 2 opaque, metal, IR-laser absorbers are on opposing sides of an IR-transparent, oxide or silicate insulator (Hirose et al. 1999; Pigott et al. 2011). This allows heating of the insulator via heating of the metal. Samples of Ni and SiO_2 were mass manufactured ($>10^4$ samples) using a combination of physical vapor deposition, photolithography, acid etching, and plasma etching (Chapter 3). The controlled-geometry samples have dimensions of 50 μm × 50 μm × 1.4 μm thick and are arranged as a double-hot plate. The double hot-plate arrangement, coupled with the chemical and spatial homogeneity of the laser absorbing layers, addresses problems caused by mixtures of transparent and opaque samples. The application of nanofabrication of controlled-geometry samples for use in diamond-anvil experiments is a novel advance in mineral physics and will have applications in a broad range of high-pressure experiments, including measurements of melting temperatures and thermal conductivity. Conversely, the fabrication techniques used here are applied to materials and length scales not generally encountered in nanofabrication.

Microfabricated samples of a simpler geometry, with a metal layer surrounded by a single oxide crystal, were also synthesized. These samples were tested with high *P-T* synchrotron-based XRD. Pt metal layer thicknesses of ≤ 0.8 μm absorb the laser and produce accurate measurements on the relative equations of state parameters of Pt and PtC (Pigott et al. 2011) (Chapter 2). Thin samples encapsulated by an oxide with low thermal conductivity reduces axial and radial temperature gradients inside of the diamond-anvil cell sample chamber such that the hottest region of the laser-heating

hotspot becomes wider (Panero and Jeanloz 2001a). An ideal sample to heating laser spot size ratio of >0.7 was determined through thermal modeling of the sample chamber using finite volume calculations carried out with the TempDAC code (Rainey et al. 2013).

1.4 Results

LHDAC x-ray diffraction experiments were conducted using nanofabricated samples at beamline 16-ID-B of the Advanced Photon Source. The experiments cover a pressure range of 10–110 GPa from 300 K to 3000 K. 200 nm thick metal layers coupled with a 1 μm thick oxide layer produce quality diffraction that can be used for *P-V-T* studies. From the XRD, the volume as a function of temperature and pressure of both the metal and oxide were calculated thus allowing for precise absolute and relative measurements of the EOS for Ni and SiO_2.

The defect energetics associated with hydrogen incorporation into tetragonal $MgSiO_3$ (majorite) garnet calculated at mantle pressures using atomistic simulations and first-principles calculations show that the hydrogarnet substitution is more favorable at all pressures between 0 and 25 GPa. The enthalpy difference between the two defect mechanisms, $[\square_{Si}(OH)_4]^X$ and $[\square_{Mg}(OH)_2]^X$ was calculated as;

$$Mg_{32N-2}Si_{32N}O_{96N}H_2 + 2MgO \leftrightarrow Mg_{32N}Si_{31N-1}O_{96}H_4 + SiO_2 \quad (1.1)$$

to determine the more favorable mechanism. Hydroxyl groups are predicted to be bound to Si vacancies as $[\square_{Si}(OH)_4]^X$ hydrogarnet defect complexes, where the Si vacancies are located at the tetrahedral sites (Pigott et al. 2015). This configuration supports the observations from IR spectroscopy (Katayama et al. 2003). OH defects affect the seismic ratio, $R = d\ln v_s/d\ln v_p$, in $MgSiO_3$ majorite (ΔR = 0.9–1.2 at 20 GPa for 1400 ppm wt H_2O) differently than ringwoodite at high pressure, yet may be indistinguishable from the

thermal $d\ln v_s/d\ln v_p$ for ringwoodite. The incorporation of 3.2 wt% Al_2O_3 also decreases $R(H_2O)$ by ~0.2–0.4.

1.5 Significance

To accurately estimate transition zone compositional and thermal anomalies, hydrous majorite needs to be considered when interpreting seismic body wave anomalies. Determination of the degree to which major mantle mineral phases such as majorite garnet participate in the global water cycle is crucial for understanding the nature of the dynamic interior of our planet. In particular, the motion and cycling of material that gives rise to plate tectonics at the surface is strongly affected by the presence of water.

To model and predict the structure, dynamics, and composition of Earth's deep interior, accurate and precise measurements of thermal equations of state are required. Modeled density profiles derived from the experimental Ni EOS require a higher proportion of a light element to match the density profile generated by the 1-D global seismic model (Dziewonski and Anderson 1981) of the inner core, and the results of this work thus having implications for the composition of the Earth and for planetary formation. A precise equation of state for SiO_2 has implications for interpretation of the fate of subducted slabs as well as for modeling of possible compositional differences between the upper and lower mantle based on the style of mantle convection.

Chapter 2: Microfabrication of Controlled-Geometry Samples for the Laser-Heated Diamond-Anvil Cell Using Focused Ion Beam Technology

The material in this chapter was reproduced with permission from the American Institute of Physics. The original article can be found at: http://dx.doi.org/10.1063/1.3658482

2.1 Introduction

The laser-heated diamond-anvil cell (LHDAC) coupled with synchrotron-based x-ray diffraction (XRD) is a powerful tool to probe materials at pressures in excess of 2 Mbar and temperatures >5000 K (Tateno et al. 2010). Second and third generation light sources have facilitated routine collection of high-resolution XRD data in seconds (Andrault and Fiquet 2001) opening up a new horizon of possible experiments. However, control of the initial sample, both chemically and spatially, is a limiting factor in high-pressure experiments. To accurately model and predict the structure and physical properties of materials at extreme conditions, we require accurate and precise measurements of a material's thermoelastic properties, phase relationships, transport properties, and melting curves. Accuracy of measured thermoelastic properties is limited by the uncertainty of alignment of the laser-heated spot with respect to the x-ray beam in which a misalignment of a few microns can result in systematic errors when measuring thermoelastic properties as a result of overestimating the sample temperature. An offset

of <5 μm, for instance, can lead to an underestimate of thermal expansion of tens of percent (Kavner and Panero 2004), thereby overestimating the bulk modulus. Large, thick, heterogeneous samples are subject to large axial and radial temperature gradients due to the extremely high thermal conductivity of the diamond anvils (Panero and Jeanloz 2001a, 2001b; Kiefer and Duffy 2005). Published melting curves and phase relationships (Boehler 1993; Shen et al. 1998) have varied from lab to lab for the same materials and using the LHDAC, which can be attributed to temperature gradients, variations in the sample dimensions, insulating media, and pressure standards. By developing methods that allow for the fabrication of controlled-geometry samples, these systematic uncertainties can be reduced. Focused ion beam (FIB) technology is currently paired with diamond-anvil cell work by drilling sample holes in metal gasketting material (Orloff et al. 2000) and thinning quenched samples to electron transparency for analysis using transmission electron microscopy coupled with energy-dispersive x-ray spectroscopy analysis (Wirth 2004; Irifune et al. 2005). Thin film chemical vapor deposition and photolithography techniques have been used to fabricate electrodes for resistivity measurements (Han et al. 2005). Using similar techniques, one can generate controlled geometry metal samples embedded in insulating crystals. Here, we report successful FIB fabrication of controlled geometry Pt layers embedded in MgO single crystals and the high *P-T* characterization of the deposited material.

2.2 Methods

Single-hot plate samples are fabricated using FIB microfabrication techniques. The samples consist of one thin (0.8–8 μm) laser-absorbing layer (Pt) deposited in a 5 × 5

or 10 × 10 μm^2 area. The Pt layer is encased in a relatively thick (10–36 μm) inert insulator (MgO).

Pure MgO single crystals are cleaved to create thin samples 10–36 μm and <250 μm wide then mounted on a SEM stub. Microfabrication of controlled geometry (5 × 5 μm^2 or 10 × 10 μm^2) Pt samples with thicknesses ranging from 0.8–8 μm are created using an FEI Nova 600 dual-beam FIB with a Ga liquid metal ion source operating with an accelerating voltage of 30 kV. Sample surfaces are cleaned with the ion beam using a current of I = 0.098 nA to remove contamination. Trenches of 5 × 5 μm^2 or 10 × 10 μm^2 are milled by ion bombardment to depths of 0.8–8 μm using I = 0.92–21 nA. Pt is deposited into the trench by ion bombardment of an organometallic precursor vapor directed over the sample surface using a current of I = 0.093 pA–0.92 nA.

The samples are loaded into a symmetric LHDAC with a ruby chip and Ar or MgO insulating medium (Fig. 1). X-ray diffraction (λ = 0.398–0.399 Å; 5–7 μm spot size) with *in situ* double-sided laser heating (λ = 1.064 μm; 15 μm HWHM at the sample surface) are conducted at HPCAT beamline 16-ID-B at the APS.

2.3. Results and discussion

Pt layer thicknesses ranging from 0.8 μm to 8 μm readily absorb the laser and produce x-ray diffraction with sufficient intensity relative to the MgO insulation. Therefore, the minimum thickness suitable to this type of sample design is determined to be ≤ 0.8 μm based on the quality of the XRD spectra from the thinnest layer tested. The Pt metal sample is deposited as a nanocrystalline material; grain growth upon laser heating is observed by narrowing of Pt diffraction lines at elevated temperatures (Fig. 2). Upon cooling and at 300 K after heating, several new peaks appeared. These peaks are

likely associated with high pressure-high temperature phases consisting of compounds of Pt, C, Ga, O, and or H. Pt deposition using a focused ion beam in conjunction with an organometallic precursor has been shown to have the following composition: 56% Pt, 26% Ga, 16% C, and 2% O and H (Gerstl et al. 2006). A loss of x-ray diffraction intensity (Shen et al. 1998) is observed at 2200(200) K and 15(5) GPa, and returns upon cooling to 1500(200) K, consistent with melting. Our observed melting temperature is lower than that determined in prior DAC studies (Kavner and Jeanloz 1998) and is attributable to melting point depression caused by impurities incorporated during deposition.

Incorporation of C is verified by the formation of PtC as a secondary phase. Diffraction from the most intense PtC reflection plane, (111), is observed in all but one of the experiments. However, in that experiment, there was strong diffraction from the (220) and (222) planes, assumed to be the consequence of preferred orientation. Due to the relatively low concentrations of PtC and the strong diffraction of the MgO single crystal and Pt, the intensity of the PtC peaks is consistently lower than the major phases. Combining our post-heating 300 K volume data (Table 1; Fig. 3) with previously published *P*-*V* data (Ono et al. 2005), we re-evaluate the PtC equation of state (EOS) according to the recent, high-quality Pt EOS by Fei et al. (2004) as the pressure standard. The uncertainties in pressure are calculated by propagation of the volume errors (Table 1) through the 3rd-order Birch-Murnaghan equation of state (BM-EOS). The large volume and pressure uncertainties in this study are a direct result of the uncertainty in the amount of C and Ga that was incorporated into the sample during the deposition process. The results from fits to the BM-EOS weighted according to both pressure and volume

uncertainties are shown in Table 2. The high *P-T Fm3m* PtC phase is synthesized here as low as P = 10(2) GPa and T = 1600(200) K, and remains stable up to P = 48(3) and T = 1500(200)–2300(200) K. We observe that the PtC phase is present upon cooling to 300 K, consistent with previous synthesis experiments at 85 GPa and 2600 K (Ono et al. 2005).

Using the definition of the 300 K bulk modulus, K_{300}, and differentiating the 3rd-order BM-EOS with respect to volume yields

$$K_{300} = -V\left(\frac{\partial P_{300}}{\partial V}\right)_T = K_0(1+2f)^{5/2}\left(1+7f-1.5(K'-4)f(2+9f)\right) \quad (2.1)$$

where f is the Eulerian strain

$$f = 0.5\left((V/V_0)^{-2/3}-1\right) \quad (2.2)$$

K_0 and K' are the zero-pressure, 300 K bulk modulus and its pressure derivative. From equation 2.1, the 300 K bulk modulus can be calculated at a given compression corresponding to a given pressure. At 15(5) GPa, the Pt and PtC bulk moduli are 343(6) GPa and 360(30) GPa based on the Pt EOS of Fei et al. (2004) and our PtC EOS (Table 2). The values for Pt K_0 and K_0' are based on the Pt equation of state of Fei et al. (2004).

Using the relationship

$$\Delta P = \alpha K_{300}\Delta T \quad (2.3)$$

where α is the coefficient of thermal expansion, we find that α_{Pt}/α_{PtC} = 1.04(8) at 15(5) GPa. This is consistent with the simultaneous unit-cell volume increase for both Pt and PtC predominantly as a result of thermal expansion under identical pressure and temperature conditions, consistent across multiple samples and upon heating and cooling (Fig. 4).

Uncertainties in V_0, V, K, and K' were propagated through all calculations and the resulting uncertainties are noted in parentheses. We assume a ±10% uncertainty in temperature to account for uncertainties arising from system response error, curve-fitting error, and axial and radial temperature gradients. The largest source of uncertainty in this method is the composition of the deposited material, which can vary from one experiment to the next.

During laser heating of samples in which Pt fully fills the depth of the MgO trench, the Pt sample evacuates the laser-heating spot as a consequence of temperature gradients. This tendency for Pt to spread was reduced by better confinement of the Pt sample by filling ~20%–65% the depth of the trench in the MgO.

2.4. Applications

Samples and laser-absorbing materials smaller than the heating laser will suffer reduced radial temperature gradients for the sample of interest by nature of being the only portion of the sample that absorbs the laser, even if the center of the heating laser is slightly misaligned. This guarantees that if the sample is diffracting, the volume sampled by the x-ray is at the peak measured hotspot temperature, even if slight misalignments occur during the experiment.

FIB techniques additionally can be combined with nanofabrication techniques similar to the methods employed for thin film deposition and computer chip fabrication to create more complex geometries for use in the diamond-anvil cell. These nanofabrication techniques will also allow for the deposition of metals, oxides, and silicates for both analysis and insulation using a double hot plate arrangement (Fig. 5) (Hirose et al. 1999) at extreme conditions. Secondary phases resulting from FIB deposited samples can

be eliminated using C-free Pt precursor material coupled with clean-room nanofabrication techniques, such as low-pressure vapor deposition and sputtering of >99.9% purity targets. The further development of controlled geometry samples will allow for measurements of thermal and chemical transport properties, as well as more precise measurements of thermoelastic properties and phase relationships.

Chapter 3: High-Pressure, High-Temperature Equations of State Using Nanofabricated Controlled-Geometry Ni/SiO_2/Ni Double Hot-Plate Samples

3.1 Introduction

Earth's core is composed of Fe metal alloyed with ~5 wt% Ni and a component of lighter elements (C, O, S, Si, H) (e.g., McDonough and Sun 1995). Earth's inner core spans a pressure range of 329–364 GPa (Dziewonski and Anderson 1981) with a likely temperature range of 4500–6500 K (Ngyuen and Holmes 2004; Hirose et al. 2013). The stable structure of iron at the conditions of Earth's inner core is likely the hexagonal close-packed (*hcp*) ε-Fe phase (e.g. Tateno et al. 2010). *Ab initio* calculations suggest that for pure iron, the face-centered cubic (*fcc*) γ-Fe phase is stable at P = 330 GPa if T > 6000 K (Côté et al. 2012), and the inclusion of Ni stabilizes *fcc* Fe at lower temperatures (Côté et al. 2012). A thermal equation of state of *fcc* nickel, a primary alloying element, in conjunction with equations of state (EOS) of iron and seismic observations, constrains the bulk composition of our planet's inner core, and allows for better understanding of the thermodynamics of the Fe–Ni system relevant to Earth's core.

Directly overlying Earth's core is the lower mantle where the volumetric majority (~80%) of minerals have octahedrally-coordinated Si (Stixrude and Lithgow-Bertelloni 2007). Stishovite is the stable phase of SiO_2 between ~300 km and ~1400–1700 km depth (Nomura et al. 2010). It consists of SiO_6 units emphasizing the fundamental importance

of determining the thermodynamic properties of stishovite. Stishovite also accounts for a significant proportion (10–16%) of subducted oceanic crust (Irifune and Ringwood 1993); therefore interpretation of seismic anomalies in regions of downwellings requires accurate measurements of the pressure-volume-temperature (*P*-*V*-*T*) equation of state of stishovite at mantle temperatures. Accurate determination of the density of stishovite is also essential for an understanding of mantle cycling associated with the dynamics of slab stagnation in and penetration through Earth's mantle transition zone (e.g., Fukao et al. 2009).

The laser-heated diamond anvil cell coupled with synchrotron-based XRD is a powerful tool to determine bulk modulus and thermal expansion, required for accurate interpretations of seismic wave speeds and reliable modeling of the structure, dynamics, and composition of Earth's deep interior. However, LHDAC experiments on transparent materials (e.g. SiO_2), which do not absorb the laser radiation to be heated directly, often rely on mixing the sample with a chemically inert laser absorbing material in order to reach high temperatures. The temperature determination in such experiments may be hampered by the non-uniform heating caused by the non-homogeneous mixing of the transparent materials with opaque laser absorbers. It has been shown that transparent samples can be sandwiched between two opaque laser absorbers in a double hot-plate formation where the two absorbers act as planar heat sources when irradiated by lasers from both sides (Hirose et al. 1999). Consideration must also be given to temperature heterogeneities due to both axial and radial temperature gradients that can exist in both homogeneous and heterogeneous samples.

We fabricated samples of Ni/SiO_2/Ni (Fig. 6) (Pigott et al. 2011) with a double hot-plate arrangement that provides uniform heating to the sample on both spatial (lateral and axial) and temporal scales (Fig. 7). With a heating spot size that is much larger than the XRD beam size, there should not be a radial temperature gradient (Fig. 8) within the x-ray volume. Due to sample thicknesses of ~1 μm, axial temperature gradients are negligible (Fig. 9). Our samples are mass produced and require ~20 hours to synthesize, suggesting an approach to address issues of reproducibility within and across laboratory groups employing LHDAC *in situ* methods. We use these samples to determine the *P*-*V*-*T* equations of state for nickel and stishovite that are free of issues arising from axial and radial temperature gradients as well as spatial heterogeneities due to opaque and transparent sample material that are not uniformly mixed.

3.2. Methods

We spin-coat a layer of polymethyl methacrylate (PMMA) on a 2″ Si-wafer substrate. A 0.2 μm Ni/1.0 μm SiO_2/0.2 μm Ni stack (>99.99% purity) is sputtered onto the PMMA. The sample is then spin-coated with Shipley 1813 photoresist. A photomask with a 50 μm × 50 μm grid is used for ultraviolet (UV) photolithographic patterning then developed for 2 minutes using MF-319 photodeveloper. Etching with dilute nitric acid and CF_4-plasma (Fig. 6) then removes the Ni-SiO_2-Ni layers not protected by the photomask resulting in ~40,000 50 μm × 50 μm × 1.4 μm samples (Fig. 6) to be lifted off of the substrate by dissolving the PMMA layer.

12 separate samples were compressed using symmetric diamond-anvil cells to *P* = 13–95 GPa (Fig. 6) with an MgO pressure medium. The MgO was fired at 1050 ºC for 2–3 hours to remove bound hydrogen. The MgO was baked at 115 ºC for 2–3 hours before

loading and the entire cell was oven-dried for 35–60 minutes at 75–80 ºC before closing to minimize adsorbed water.

Samples were heated to T = 1000–3100 K, while compressed in a DAC, using the double-sided laser-heating system at Sector 16-ID-B of the Advanced Photon Source (APS) with two Gaussian fiber lasers (λ = 1.064 μm). The FWHM of the thermal radiation image from a hotspot on a Pt foil heated at ambient pressure was 48 μm. Temperature measurements were conducted by collecting thermal radiation (between 600-800 nm wavelength) from a 4 μm spot on the sample in the center of the laser-heated spot (coaligned with the x-ray beam)(Fig. 10). The uncertainty in the sample temperature, δT_{sample} is assumed to be

$$\delta T_{sample} = \frac{\Delta T_{meas} + 100}{2} \tag{3.1}$$

where ΔT_{meas} is the difference between the upstream and downstream measurements. The additional 100 K accounts for uncertainty due to system response error, chromatic aberration, wavelength-dependent emissivity, axial and radial temperature gradients, and curve fitting errors. With a skin depth of <10 nm for Ni at a 1 μm wavelength, interaction of the lasers with the SiO_2 layer is not a source of uncertainty in the thermal measurements. *In situ* XRD (λ = 0.4066 Å; 6–7.5 × 6–7.5 μm FWHM for experiment numbers 8XXX; 5 μm × 5.5 μm FWHM for experiment numbers 10XXX) was collected (Fig. 11). We first heated our samples to high temperature and then measured the volumes while gradually decreasing the temperature, which was to anneal and relax the deviatoric stresses in the samples and result in a better EOS.

We fit our data to the finite-strain 3rd-order Birch-Murnaghan (BM) equation of state (Birch 1952)

$$P_{300K} = \frac{3}{2}K_0\left[\left(\frac{V_0}{V}\right)^{\frac{7}{3}} - \left(\frac{V_0}{V}\right)^{\frac{5}{3}}\right]\left[1 + \frac{3}{4}(K_0' - 4)\left(\left(\frac{V_0}{V}\right)^{\frac{2}{3}} - 1\right)\right] \quad (3.2)$$

with a Mie-Grüneisen-Debye (MGD) formalism based on lattice dynamics

$$P_{th} = \frac{\gamma(U_T - U_{300K})}{V} \quad (3.3)$$

$$U = 9nRT\left(\frac{T}{\theta}\right)^3 \int_0^{\frac{\theta}{T}} \frac{x^3}{e^x - 1} dx \quad (3.4)$$

for the thermal pressure (P_{th}) contribution to the total pressure (Jackson and Rigden 1996) in which

$$P(V,T) = P_{300K}(V) + P_{th}(V,T) \quad (3.5)$$

K_0 and K_0' are the bulk modulus and its pressure derivative, U is internal energy, γ is the Grüneisen parameter, n is the number of atoms per formula unit, R is the gas constant. θ is the Debye temperature, and q describes the compressional dependence of γ according to

$$\gamma = \gamma_0\left(\frac{V}{V_0}\right)^q \quad (3.6)$$

$$\theta = \theta_0 \exp\left(\frac{\gamma_0 - \gamma}{q}\right) \quad (3.7)$$

We also fit our data to the high-temperature Birch-Murnaghan (HTBM) equation of state (e.g., Angel 2000) in which:

$$K_0(T) = K_0(T_0) + (T - T_0)\left(\frac{\partial K}{\partial T}\right)_P \quad (3.8)$$

$$V_0(T) = V_0(T_0) \exp \int_{T_0}^{T} \alpha\,(T) dT \quad (3.9)$$

where T_0 = 300 K. The coefficient of volumetric thermal expansion, α, is assumed to have a linear temperature dependence (e.g., Angel 2000) such that

$$\alpha(T) = \alpha_0 + \alpha_1 T \quad (3.10)$$

We use the thermal equation of state of MgO (Speziale et al. 2001) to calculate the total pressure of the sample. For a cross-check, we also calculate the total pressure using the stishovite (Wang et al. 2012) and nickel (Campbell et al. 2009) equations of state. We assume that the volume-average effective temperature of the MgO within the x-ray is between the temperature measured by spectroradiometry and the temperature at the surface of the diamond anvils (Campbell et al. 2009). Given room temperature, T_{room},

$$T_{MgO} = (3T_{measured} + T_{room})/4 \quad (3.11)$$

We assume an uncertainty in T_{MgO} that is twice the uncertainty in the sample temperature. The temperature of the nickel and stishovite is taken to be the peak measured temperature. Uncertainties in the MgO equation of state, temperatures, and measured volumes are propagated through the total pressure calculations.

3.3. Results

Nickel and stishovite *P*-*V*-*T* data are fit to the BM, HTBM, and MGD equations of state to derive K_0, K_0', $(\partial K_{0,T}/\partial T)_P$, α_0, α_1, γ_0, and q. The nickel data are fit up to P = 109(5) GPa and T = 300–2900(500) K. The stishovite data span pressures up to 47(1) GPa and T = 300–2440(80) K. It should be noted that we include all of our *P*-*V*-*T* data in the fitting and we only exclude data points that do not have a *T*, *V*, or *P* associated with them. At P = 60–108 GPa, we document the observed d-spacing of the $CaCl_2$-structured SiO_2 (110) diffraction line. We observe no chemical interaction between the sample layers based on scanning transmission electron microscopy (STEM), energy dispersive spectroscopy (EDS) of a run product (Fig. 12), or anomalous diffraction from a new phase in the 2-D XRD patterns.

We fit our 300 K nickel data to the 3rd-order BM-EOS resulting in K_0 = 201(6) GPa and K_0' = 4.4(3) with V_0 fixed to the measured value of 6.579(1) cm^3/mol (Table 3). These fix the 300 K equation of state while we fit our high temperature data separately to thermal equations of state. Unweighted least-squares fitting to the MGD EOS yields γ_0 = 1.98(8) and q = 1.3(2) (Fig. 13a), while the HTBM-EOS yields $(\partial K_{0,T}/\partial T)_P$ = –0.026(2) GPa/K, $\alpha_0 = 2.7(2) \times 10^{-5}$ K^{-1}, and $\alpha_1 = 0.9(2) \times 10^{-8}$ K^{-2}.

As a cross check to our use of MgO as a pressure standard, we fit our nickel data up to 49 GPa using the Wang et al. (2012) 300 K and thermal equation of state for stishovite as the internal standard (Table 3) with the peak measured temperature as the SiO_2 temperature. The stishovite data do not cover a sufficient compression range to constrain q. Using stishovite as the pressure standard results in a broadly consistent Ni high-temperature equation of state, with γ_0 = 2.04(4), 7% greater than the MgO equation of state when assuming q = 1 (Table 3). Assuming a lower temperature for the MgO ($T_{meas}/2$) results in a Grüneisen parameter that is 40% less than when using the stishovite equation of state over an equivalent pressure range when all other parameters are the same. The inconsistency provides evidence that our T_{MgO} is reasonable. The HTBM-EOS yields $(\partial K_{0,T}/\partial T)_P$ = –0.063(2) GPa/K, $\alpha_0 = 0.9(4) \times 10^{-5}$ K^{-1}, $\alpha_1 = 6.6(7) \times 10^{-8}$ K^{-2}, inconsistent with our results from fitting over the entire experimental pressure range with the MgO pressure standard by a factor of 2.5–7. However, there is agreement between the two pressure standards if we fit the same smaller subset of data. Using MgO as the pressure standard up to 47 GPa, we find that $\alpha_0 = 0.5(5) \times 10^{-5}$ K^{-1}, $\alpha_1 = 6.6(7) \times 10^{-8}$ K^{-2}, and $(\partial K_{0,T}/\partial T)_P$ = –0.066(2) GPa/K thus validating our assumption of the average temperature in the MgO.

Our stishovite results based on the MgO pressure standard are consistent with Panero et al. (2003) with K_0 = 315(3) GPa when K_0' is fixed to 4.8. Using the Panero et al. (2003) 300 K equation of state with the Debye temperature fixed at 1109 K (Akaogi et al. 2011), the value determined from heat capacity measurements, in the MGD EOS leads to γ_0 = 1.36(2) for q = 1 (assumed) or γ_0 = 1.55(1) with q = 2.9 (Wang et al. 2012) (Table 3) (Fig. 13b). θ_0 is poorly constrained as a free parameter, decreasing from 1000(300) to 900(500) for q =1 and q = 2.9, respectively, while not affecting γ_0 within the uncertainty. The high-temperature BM-EOS produces $(\partial K_{0,T}/\partial T)_P$ = –0.058(1) GPa/K, $\alpha_0 = 1.94(8) \times 10^{-5}$ K^{-1}, and $\alpha_1 = 1.2(1) \times 10^{-8}$ K^{-1}. We compare the relative axial compressibility using a modified BM-EOS (e.g., Xia et al. 1998; Runge et al. 2006)

$$P = \frac{3}{2}K_0\left[\left(\frac{l_0}{l}\right)^7 - \left(\frac{l_0}{l}\right)^5\right]\left[1 + \frac{3}{4}(K_0' - 4)\left(\left(\frac{l_0}{l}\right)^2 - 1\right)\right] \quad (3.12)$$

where l is the length of the a or c axis and l_0 refers to the zero-pressure lattice parameter (Table 3). The axial compressibility is then

$$\beta_l = -\frac{1}{l}\left(\frac{\partial l}{\partial P}\right)_T = -\frac{1}{l}\frac{1}{\left(\frac{\partial P}{\partial l}\right)_T} = \frac{1}{3K_l} \quad (3.13)$$

The longer a axis is 57% more compressible than the c axis, with K_{0a} = 284(5) GPa and K_{0c} = 450(20) GPa. The linear axial thermal expansion coefficient (α_l) can be calculated by substituting a^3 and c^3 for V in the HT-BMEOS (Xia et al. 1998) with $\alpha_l = \alpha_V/3$. The thermal expansion coefficient, α_{0a}, is a factor of 2–3 greater than α_{0c}, 0.69(6) × 10^{-5} K^{-1}, compared to 0.3(1) × 10^{-5} K^{-1} and has a ~30% smaller temperature dependence expressed as α_1 (Table 3).

We also determine the stishovite equation of state using nickel as the pressure standard based on the Campbell et al. (2009) equation of state (Table 3). The Campbell et

al. (2009) study used the NaCl thermal insulation as the pressure standard. Using the MGD EOS we fit the *P*-*V*-*T* stishovite data to $\gamma_0 = 1.61(7)$ and $q = 2.5(6)$. The nickel layers as the pressure standard results in a stishovite Grüneisen parameter 6–7% greater than when using the MgO layers as the standard given the same values of q. $(\partial K_{0,T}/\partial T)_P = -0.044(5)$ GPa/K and $\alpha_0 = 1.5(2) \times 10^{-5}$ K^{-1} are also different from the values derived from the MgO equation of state by ~30%. We conclude that the discrepancies between the MgO and nickel pressure standard are not based on our assumed average temperature. This conclusion is based on the agreement between the MgO and stishovite pressure standards when determining the nickel equation of state over an equivalent pressure range. The stishovite equation of state (Wang et al. 2012) used as a pressure standard is derived from multi-anvil press experiments that do not require assumptions about average temperatures within the insulation. The slight disagreement between the results using the Ni and MgO as pressure standards for the stishovite EOS is a direct result of an inconsistency between the two equations of state. The inconsistency lies in the compressional rather than thermal factors of the equation of state (Fig. 14).

At pressures where $CaCl_2$-structured SiO_2 is stable (Andrault et al. 2003; Nomura et al. 2010; Yamakazi et al. 2014), we index the (110) reflection at high pressure and temperature, but are unable to index sufficient diffraction peaks to fit the orthorhombic cell parameters in all but one experimental run. The observed d-spacing of the (110) peak at 300 K begins to deviate to slightly smaller d-spacing (≤ 0.008 Å) than predicted based on the stishovite equation of state consistent with the greater compressibility of the *a*-axis relative to stishovite (Andrault et al. 2003) (Fig. 15). The high-temperature behavior of

the (110) reflection from the inferred $CaCl_2$ structure is indistinguishable from the stishovite extrapolation within uncertainty.

3.4. Discussion

We extended the nickel thermal equation of state to $P > 100$ GPa (Table 3). Refitting the Campbell et al. (2009) 300 K data (Fig. 16) yields $K_0 = 205(4)$ GPa modifying their γ_0 to 1.86(5), which agrees with our results and highlights the tradeoff between K_0 and γ_0. Our Ni zero-pressure, 300 K thermal expansivity is $3.0(2) \times 10^{-5}$ K^{-1} (equation 3.10), compared to $\alpha = 3.87 \times 10^{-5}$ K^{-1} determined using density functional theory (Zeng et al. 2012) and room-pressure experiments (Kollie 1977). Fitting our data using the 300 K isotherm from Dewaele et al. (2008) leads to $\alpha = 3.9(2) \times 10^{-5}$ K^{-1}.

We provide an extension of the stishovite equation of state to lower mantle temperatures (Table 3) using a complimentary technique. Our Grüneisen parameter for stishovite is in reasonable agreement with that obtained in a recent sintered-diamond multi-anvil press study (Wang et al. 2012), whose value was ~7% larger. However, excellent agreement is found when refitting the Wang et al. (2012) dataset with $q = 1$ (fixed) (Fig. 17). Plasma vapor deposition using an SiO_2 target results in deposited material that is oxygen deficient (e.g., Jorgenson and Wehner 1965). However, our measured zero-pressure volume, $V_0 = 13.98(1)$ cm^3/mol, is indistinguishable from the stishovite synthesized from fused silica ($V_0 = 13.82$–14.02 cm^3/mol) (Panero et al. 2003). Our 300 K thermal expansivity, $2.32(8) \times 10^{-5}$ K^{-1}, is about half the value found in molecular dynamics simulations (Luo et al. 2002) and much closer to the value of $1.86(5) \times 10^{-5}$ K^{-1} from the experimental work of Endo et al. (1986). The discrepancy between

experimental and computational results is likely a result of the force field parameterization leading to an overestimate of anharmonicity (Luo et al. 2002).

At inner core conditions, experiments and theory predict iron density to be 1% to 9% greater than the Preliminary Reference Earth Model (PREM) (e.g., Dewaele et al. 2006; Murphy et al. 2011; Yamakazi et al. 2012). Our Ni equation of state (Table 3) predicts *fcc* Ni to be ~14% denser than PREM and ~7–10% denser than *hcp* and *fcc* Fe at 5000 K (Fig. 18a) (Uchida et al. 2001; Tsujino et al. 2013), comparable to $Fe_{0.9}Ni_{0.1}$ alloy experimental results (+1.4% relative to Fe) (Sakai et al. 2014). Thus, alloying of Ni in the core requires more light elements to reconcile density models with experimental data. The density difference between Fe and Ni is only partially attributable to the higher molar mass of Ni relative to Fe (+5%) which should be considered when formulating compositional models of the inner core.

Having considered the density of nickel in Earth's core, it is also reasonable to look at the density of stishovite in Earth's mantle. Basaltic crust subducted into the lower mantle can contain >20% stishovite (Perrillat et al. 2006) and potentially more silica can be recycled into the mantle via continental crust subduction (Chopin 2003). Using our thermal equation of state (Table 3), stishovite is ~50% denser than PREM in the transition zone along a typical mantle geotherm (Stacy and Davis 2008), but at the top of the lower mantle, the density difference drops to <2% (Fig. 18b). By 59 GPa (~1400 km), stishovite is more buoyant than the average mantle, while along a hot slab geotherm, this crossover occurs at 64 GPa (~1500 km). In contrast, in extremely cold slabs such as the Tonga subduction zone where the temperature might be 600 K less than the mantle adiabat (e.g., Kirby et al. 1996; Bina and Navrotskty 2000; Syracuse et al. 2010),

stishovite remains denser than PREM throughout its stability field (Nomura et al. 2010). Slab stagnation and slab avalanche are complex phenomena that depend on temperature, composition, mineralogy, and rheology (e.g. Hirose et al. 2005; Fukao et al. 2009; Marquardt and Miyagi 2015). Considering large variations in subducted sediment thickness and chemistry (Poli and Schmidt 2002) and the potential for the subducted crust to sink separately from the subducted mantle lithosphere (e.g., Niu et al. 2003), it is likely that the SiO_2 component plays a role in slab stagnation and avalanche.

In addition to the application demonstrated here, in which we have used the samples to produce a controlled 3-dimensional thermal regime in the diamond-anvil cell, the nanofabrication techniques utilized in this study provide the ability to specifically tune samples to high-pressure experiments. For example, controlled-geometry samples can be designed for diamond-anvil cell studies of diffusion and elemental partitioning (e.g., Reaman et al. 2012) between oxides, silicates, and iron alloys. Nanofabricated samples with precisely known dimensions are particularly suited for experiments related to thermal and electrical conductivity. More sophisticated deposition techniques such as pulsed laser deposition and molecular beam epitaxy can be used for more complex compositions. Samples can be produced for melting experiments in which the nanofabricated samples could be contained in a single crystal by milling a trench with a focused-ion beam (Pigott et al. 2011). Finally, the mass-production of chemically and spatially uniform samples can promote community-wide “round-robin” projects where equations of state are measured on samples from a common source across different beamlines.

Chapter 4: Calculation of the Energetics of Water Incorporation in Majorite Garnet

The material in this chapter was reproduced with permission from the Mineralogical Society of America. The original article can be found at:

http://dx.doi.org/10.2138/am-2015-5063

4.1. Introduction

The amount of water stored in deep crustal and mantle rocks is largely unconstrained, yet may account for a quantity of water comparable to or in excess of the amount contained in the present oceans (Hirschmann 2006). Water has a first-order effect on the compressibility and deformation of the crust and mantle (e.g., Smyth et al. 2004; Xu et al. 2013), in addition to melting temperature and electrical and thermal conductivity (e.g., Hirschmann 2006; Thomas et al. 2012; Panero et al. 2013). Since water is incorporated into the nominally anhydrous mineral phases of Earth's mantle in the form of H defects (e.g., Wright 2006), a clear understanding of the atomic-scale behavior and substitution mechanism of hydrogen in high-pressure silicates is critical to our knowledge of mantle processes.

Majorite, $(Mg,Fe)SiO_3$, is the high-pressure garnet phase stable at transition-zone depths (410–660 km) and is the second most abundant phase after the high-pressure olivine polymorphs, accounting for as much as 40% of the rock volume (Frost 2008). The

defect-free, tetragonal Mg-endmember garnet, majorite (space group $I4_1/a$), has a structure consisting of three unique tetrahedral sites (Si1, Si2, and Si3) each linked by corner O atoms to octahedral sites, Mg3 and Si4, and two interstitial distorted dodecahedral sites, Mg1 and Mg2 (Fig. 19) (Angel et al. 1989). The three tetrahedral sites are distinguished from each other based on the occupancy of the nearest neighbor octahedral sites. The Si1 tetrahedra are linked to Mg3 octahedra, the Si2 sites are linked to Si4 octahedra, and Si3 tetrahedra are linked to two Mg3 octahedra and two Si4 octahedra. The interstitial Mg1 dodecahedral site is more distorted than the Mg2 site. There are six unique oxygen sites (Table 4). The O1 and O2 sites have the same bonding environment but O1 is bonded to octahedral Mg and O2 is bonded to octahedral silicon. The O3 and O4 sites are both doubly bonded to the Mg1 distorted cubic site. Finally, the O5 and O6 sites are both involved in two cubic environments and one tetrahedra but O6 is bonded to the octahedral Si and O5 is bonded to the Mg octahedra.

The dominant carriers of hydrogen in the transition zone are the high-pressure polymorphs of $(Mg,Fe)_2SiO_4$ (olivine), wadsleyite, and ringwoodite, which can incorporate significant amounts of hydrogen (1–3 wt% H_2O) into their structures (e.g., Kohlstedt et al. 1996; Smyth and Jacobsen 2006). Partitioning experiments in the MgO-SiO_2-H_2O system at transition zone P-T conditions show that the olivine polymorphs (wadsleyite and ringwoodite) dissolve ~1 order of magnitude more than $MgSiO_3$ (majorite, clinoenstatite, akimotoite) (Bolfan-Casanova et al. 2000) such that $D^{Mg2SiO4/MgSiO3}$ = ~10. Because the solubility of water in the olivine polymorphs decreases with temperature and the partitioning of water between wadsleyite and ringwoodite may be close to $D^{wad/ring}$ = 1 at high temperature (Bolfan-Casanova 2005),

majorite solubility and partitioning may play an important role throughout the entire thickness of the transition zone. Water solubility in majorite garnet synthesized at transition zone pressures and temperatures can contain up to ~700 ppm wt H_2O (Bolfan-Casanova et al. 2000; Katayama et al. 2003), a quantity sufficient to radically change the deformation characteristics of garnet. For a more complete understanding of the implications of OH defects in garnet in the deep mantle, systematic computational studies of hydrogen incorporation into majorite are required.

At low pressures, H substitution in andradite garnet ($Ca_3Fe_2Si_3O_{12}$) takes place via the hydrogarnet defect in which four hydrogen atoms charge balance a vacancy ordinarily occupied by a Si atom in the tetrahedral site (Lager et al. 1989). However, the hydrogarnet defect is associated with a volume expansion of the tetrahedral site (e.g., Lager et al. 1989; Purton et al. 1992) due to the change in Coulomb forces caused by the Si vacancy and also to accommodate the hydrogen bonded network. This volume expansion should be less energetically favorable at high pressure. Infrared absorption spectra indicate that OH is potentially incorporated into majorite by formation of the hydrogarnet defect (Katayama et al. 2003). However, water concentrations in natural garnet samples brought to the surface from the mantle (Bell and Rossmann 1992a, 1992b) and infrared spectroscopy of both natural garnet (Amthauer and Rossman 1998; Beran and Libowitzky 2006) and synthetic majorite (Bolfan-Casanova et al. 2000) indicate that hydrogen incorporation in majorite may be complex (Williams and Hemley 2001). Therefore a systematic investigation of the hydrogen uptake mechanism in majorite is necessary to clarify the situation.

Lateral variations in seismic body wave velocities throughout the mantle are caused by temperature and compositional (i.e., water concentration, iron content, partial melting) heterogeneities (Karato 2006). The hydration of transition zone minerals affects the seismic data used to infer high- and low-temperature anomalies and interpretation of mantle plumes and subducted slabs. The seismic ratio, $R = d\ln v_s / d\ln v_p$ can be used to differentiate between thermal and compositional effects (Karato and Karki 2001). Indeed variations in seismic velocities, expressed as $d\ln v_s / d\ln v_p$, have been used to suggest a strategy to disentangle the effects of temperature and water content for ringwoodite and wadsleyite (Panero 2010; Li et al. 2011). The temperature and pressure dependence of majorite sound velocities have been established experimentally (Sinogeikin and Bass 2002; Irifune et al. 2008). Constraining the effect of water on majorite elasticity is critical to the accurate interpretation of seismic velocities in Earth's transition zone.

By analogy with other H defects in high-pressure silicates, H is likely incorporated into the dodecahedral, octahedral, and tetrahedral sites of the majorite structure. While interstitial hydrogen incorporation is possible in olivine (Balan et al. 2014), it is not likely in the denser garnet structure at high pressure. Thus, we present a computational investigation of the energetics and associated geophysical properties (P- and S-wave velocities) resulting from hydrogen incorporation in majorite via $[\square_{Mg}+2OH_O]^X$ and $[\square_{Si}+4OH_O]^X$ defects. By comparing the defect energies associated with these different site substitutions of hydrogen, we determine the most favorable hydrogen-defect mechanism. Additionally, we further investigate the influence of aluminum on hydrogen incorporation and wave speeds.

4.2 Computational methods

The energies associated with hydrogen and aluminum incorporation in tetragonal majorite garnet ($MgSiO_3$) were calculated as a function of pressure up to P = 25 GPa using classical atomistic simulations based on the Born model of solids, as implemented in the General Utility Lattice Program (GULP) (Gale and Rohl 2003).

The initial majorite structure was generated according to the experimental single-crystal structure refinement (Angel et al. 1989). Mg and Si are assumed to be ordered over the two symmetry unique octahedral sites based on the low concentration of aluminum (< ~8 wt% Al_2O_3) and temperature (T = 0 K) (Nakatsuka et al. 1999; Vinograd et al. 2006). Majorite lattice energy minimizations were performed using the full body-centered tetragonal unit cell, which consists of 160 atoms.

Interatomic potential functions were used to describe the total lattice energy in terms of the atomic positions. We adopt the fractional charges of Vinograd et al. (2006) where ionic charges are scaled by 0.85 to improve transferability with respect to cation-cation distances. The internal lattice energy is dominated by the Coulomb interactions and evaluated using an Ewald summation. We modeled the short-range interactions between closed shell ionic species using a Buckingham potential of the form;

$$U_{sr} = \sum_{ij} A_{ij} exp\left(-\frac{r_{ij}}{\rho_{ij}}\right) - \frac{C_{ij}}{r_{ij}^6} \quad (4.1)$$

where A, ρ, and C are empirically derived parameters. The sum is over pairs of ions, i and j ($i \neq j$), with a separation distance, r_{ij}. Cutoffs for the Buckingham potentials are 10.0 Å for hydrogen interactions and 12.0 Å for oxygen-oxygen and cation-oxygen interactions. These potentials are tapered to zero over a range of 2.0 Å to ensure smoothness of the potential energy surface (Mei et al. 1991).

Due to the partial covalence of the Si-O bond (Pauling 1980), a harmonic angle-bending term was also included:

$$U_{ijk} = \frac{1}{2} k_\theta (\theta - \theta_0)^2 \quad (4.2)$$

This was applied for both the Si-O and Al-O tetrahedra and octahedra to add an energy penalty when there is a deviation from the coordination-dependent equilibrium bond angle. Three-body terms applied to the majorite Si-O and Al-O polyhedra were defined based on bonding between ions, which was defined to be fixed during relaxation, rather than cutoff distances. The three-body contribution to the optimized total energy was confirmed to ensure that the bonding was correctly defined for each system such that no spurious terms were present. A shell model (Dick and Overhauser 1958) was adopted to account for the polarizability of the oxygen anions. The O core-shell interactions are described by spring constants with the functional form:

$$U = \frac{1}{2} k_2 r^2 + \frac{1}{24} k_4 r^4 \quad (4.3)$$

The short-range bonded O-H interaction was described using a Coulomb-subtracted Morse potential (Saul et al. 1985)

$$U_r = D_e \left[\left(1 - \exp\left(-a(r - r_0)\right) \right)^2 \right] - \frac{q_i q_j}{r} \quad (4.4)$$

where r_0 is the equilibrium bond length, q is the charge of the species, D_e and a are both fitted parameters physically related to the molecular dissociation energy and vibrational frequency. Here the Coulomb term is expressed in atomic units. The Morse potential is cutoff at 1.3 Å, while the Buckingham potential is excluded for the intramolecular interaction within the hydroxyl group.

Interatomic potential parameters (Table 5) developed for the anhydrous majorite-pyrope solid solution (Vinograd et al. 2006) were augmented with force field parameters derived by fitting to experimental structural and elastic properties of brucite, $Mg(OH)_2$, at both 0 GPa and high pressure (Catti et al. 1995; Jiang et al. 2006). Due to the different fractional charge of the hydroxyl oxygen ($O^{-1.2}$) compared to the non-hydroxyl oxygen ($O^{-1.7}$), we derived the Buckingham potential parameter, *A*, by fitting to data for brucite. The two-body potentials for the interaction between the hydroxyl oxygen and both Al and Si were generated from those for the equivalent interaction for non-hydroxyl oxygen using scaling of coefficients (Schröder et al. 1992) by 0.709 assuming

$$\frac{A_{Mg-O^{-1.2}}}{A_{Mg-O^{-1.7}}} = \frac{A_{Si-O^{-1.2}}}{A_{Si-O^{-1.7}}} = \frac{A_{Al-O^{-1.2}}}{A_{Al-O^{-1.7}}} \tag{4.5}$$

Validation of the potential model was accomplished through calculation of the structural relaxation, including unit-cell parameters, and elasticity of majorite for pressures between 0 and 25 GPa. Additionally, we calculate the structure and elasticity of superhydrous B, $Mg_{10}Si_3O_{14}(OH_4)$, for pressures between 0 and 25 GPa and the zero-pressure structure and bulk modulus of pyrope, corundum, α-quartz, coesite, stishovite, MgO, brucite, kaolinite, and lizardite using the interatomic potentials in Table 5.

A Newton-Raphson optimizer, with Broyden-Fletcher-Goldfarb-Shanno (BFGS) updating of the Hessian matrix, was used for energy minimization. When the gradient norm reached 0.1, we switched to rational function optimization (RFO) to ensure that the final state attained had positive definite curvature. The phonon density of states was also calculated to verify the absence of imaginary modes within the Brillouin zone.

Energy minimizations were performed on the majorite structure with both charged and charge-neutral point defects. Intrinsic vacancies were created by removal of a single

atom or bound Mg-O pairs where the Mg and O are nearest neighbors. Using the Kröger-Vink defect notation, the intrinsic vacancy defects are expressed as $\square_{Mg}''$, $\square_{Si}''''$, and $\square_{O}^{\cdot\cdot}$. We calculated Schottky defect energies in the form of vacancies where the negatively charged cation vacancy is balanced by a positively charged oxygen vacancy. For mass balance, the atoms that are removed are assumed to form a crystalline solid whose lattice energy also contributes to the Schottky defect energy. The extrinsic defects $OH_O^{\cdot}$, Al_{Si}', $Al_{Mg}^{\cdot}$, $[\square_{Mg}+2OH_O]^X$, $[\square_{Si}+4OH_O]^X$, $[Al_{Si}+Al_{Mg}+\square_{Mg}+2OH_O]^X$, and $[Al_{Si}+Al_{Mg}+\square_{Si}+4OH_O]^X$ were introduced by generating vacancies and introducing impurities as appropriate. For the $OH_O^{\cdot}$ defect, the H atom was initially placed at three different positions relative to each oxygen site and energy minimization calculations were run to determine the lowest energy configuration. The lowest energy configuration was then used for the high-*P* calculations and we do not see a change in the relaxed hydrogen configuration up to 25 GPa. The difference in energy between the defective and the defect-free majorite lattice was taken to be the defect formation energy. Calculations with a single $[\square_{Mg}+2OH_O]^X$ or $[\square_{Si}+4OH_O]^X$ defect complex per unit cell contain 0.56–1.1 wt% H_2O and thus additional simulations were performed using 2 × 2 × 2 supercells (1280 atoms) for a more realistic concentration of hydrogen within the system (700–1400 ppm wt H_2O) and to assess the influence of defect-defect interactions through the periodic boundary conditions. The initial atomic positions of impurities were determined visually using GDIS (Fleming and Rohl 2005) and confirmed after optimization. The lattice parameters for the pressure of interest were generated from constant pressure optimizations of the defect-free bulk cell. Charged defect calculations are performed in the presence of a uniform neutralizing background charge at constant volume. The initial

fractional coordinates for the high-pressure calculations involving charged defects were taken from the optimization at the previous lower pressure. This ensures that a consistent configuration is being considered as a function of pressure. Calculations involving majorite with charge-neutral defect complexes or any calculation involving a defect-free phase were performed at constant pressure.

Complementary first-principles simulations were conducted at zero-pressure and P = 20 GPa for the most energetically favorable charge-balanced defect complexes as determined by the atomistic simulations. Static, DFT calculations were performed with VASP (Kresse and Furthmüller 1996a, 1996b). Ultrasoft pseudopotentials were used and calculations were performed using the Perdew-Wang 1991 (PW91) formalism of the generalized gradient approximation (GGA) for the exchange-correlation functional (Perdew 1991). All first-principles calculations were performed using a planewave cutoff of 600 eV with an energy convergence criterion of 0.001 eV for optimization. The majorite calculations are performed at the Γ point for Brillouin zone sampling due to the size of the unit cell. In contrast, the MgO and SiO_2 calculations are averaged over Monkhorst-Pack grids of dimensions 16 × 16 × 16 and 8 × 8 × 8 **k**-points, respectively. To increase computational efficiency, all structures were first relaxed at constant volume then subsequently relaxed at constant pressure.

The relative stability of the two defect mechanisms, $[\square_{Mg}+2OH_O]^X$ and $[\square_{Si}+4OH_O]^X$ was determined by calculating the enthalpy according to the reactions

$$Mg_{32N-2}Si_{32N}O_{96N}H_4 + 2MgO \leftrightarrow Mg_{32N}Si_{32N-1}O_{96N}H_4 + SiO_2 \quad (4.6)$$

and

$$Mg_{32N-3}Al_2Si_{32N-1}O_{96N}H_4 + 2MgO \leftrightarrow Mg_{32N-1}Al_2Si_{32N-2}O_{96N}H_4 + SiO_2 \quad (4.7)$$

where N is the number of unit cells, with the assumption that the $[\square_{Mg} + 2OH_O]^X$ defects are non-interacting. The enthalpy of SiO_2 was calculated while accounting for the α-quartz→coesite→stishovite phase transitions as a function of increasing pressure. The MgO and SiO_2 calculations were performed using the same interatomic potentials (GULP) and pseudopotentials (VASP) as for the majorite calculations, and the initial unrelaxed structures were taken from the American Mineralogist Crystal Structure Database (AMSCD) (Hazen 1976; Levien et al. 1980; Levien and Prewitt 1981; Ross et al. 1990). This reaction does not involve free H_2O due to the difficulty of modeling the energetics of supercritical water.

4.3 Results

4.3.1. Validation of calculations

The calculated majorite structure (Fig. 19) (Table 6) reproduces the experimentally determined structure (Angel et al. 1989) as we find good quantitative agreement between our calculated results and those previously determined from both theory and experiment (Table 7). The structural parameters are within 0.6% of the experimental values, while the errors are <6% for most elastic constants with the exception of C_{12} and C_{16} (Table 8). Our calculated zero-pressure bulk modulus and shear modulus are within the spread of experimental results and at P = 10 GPa deviate from experimental data (Sinogeikin and Bass 2002) by <3.5% (Table 8; Fig. 20). Results from our static lattice-energy calculations (SLEC) and the results from Vinograd et al. (2006) were obtained using essentially the same potential models, except for changes to the truncation of the Buckingham potentials and the inclusion of a fourth-order spring constant in the shell model. Hence, the agreement here is to be expected. For phases other

than majorite, we find agreement between our calculations and experimentally determined values (Table 9; Fig. 21), with differences of less than ~5% for all structural parameters and ~13% for most bulk moduli. The greatest differences in bulk moduli are for MgO and brucite due to the inability of a simple shell-model to capture the well-known Cauchy violation ($C_{12} \neq C_{14}$) in periclase (Catlow et al. 1976) and the limited transferability of the interatomic potentials to non-silicates. Our first-principles calculations reproduce the experimental structure and are consistent with previous DFT-GGA results (Table 6; Table 7). The generalized gradient approximation used here tends to lead to a systematic overestimation of structural parameters when compared to experiment, consistent with the observations in the present study. The axial ratio calculated at P = 20 GPa using DFT results is only 0.3% smaller than the force field approach.

4.3.2. Defect energies in the absence of water incorporation

The enthalpy of charged Mg, Si, and O, vacancy formation in $MgSiO_3$ garnet were calculated up to P = 25 GPa. The ^{VIII}Mg2 and ^{IV}Si2 sites are found to have the lowest energetic cost for forming Mg and Si vacancies (Table 10; Fig. 22). The octahedral site is significantly less favorable for both Mg and Si vacancy defects. The Schottky defect with the lowest energy ($E_{Schottky}$ = 4.48–7.24 eV) is the $[\square_{Mg2}+\square_{O5}]^{X}$ defect (Table 10) in which the Mg-vacancy and O-vacancy are nearest neighbors with an additional energy cost of 0.07–0.26 eV when Mg2 and O5 vacancies are not nearest neighbors. Formation of a vacancy at the Mg1 site, which is bonded to all 6 O atoms, has a greater Schottky defect energy at zero-pressure when the vacancies at the O1 and O2 sites are not nearest neighbors. Conversely at high pressure, lower

Schottky defect energies tend to be associated with Mg and O vacancies that are nearest neighbors with the exception of $\square_{Mg1}''$ neighboring $\square_{O1}^{\cdot\cdot}$ or $\square_{O6}^{\cdot\cdot}$. When considering the silicon sites, ^{IV}Si2 vacancies have the lowest Schottky defect energies (Table 10).

4.3.3. Protonation mechanism

Protonation of the O1, O4, and O5 sites have energies 0.3–0.6 eV lower than O2, O3, and O6 at zero pressure (Fig. 23). The protonation energetics can be explained by whether Si (higher energy) or Mg (lower energy) occupies the octahedral site to which the protonated oxygen is bonded. Among the octahedral-Mg oxygen sites, the O5 site is the most favorable site for protonation with a defect formation energy 0.09–0.1 eV lower than O4 and O1. Protonation of the O6 site is 0.20–0.21 eV less favorable compared to the other two sites (O2 and O3) involved in Si octahedra.

At all pressures, the O5 site is the most likely to bind a hydrogen atom and the O5 protonation enthalpy increases with pressure at a smaller rate than for the other oxygen sites (Fig. 23). Furthermore, protonation of the oxygen sites involved in Si octahedra become less favorable with pressure relative to the sites involved in Mg octahedra.

Based on the energetics associated with creating charged cation and oxygen vacancies, neutral Schottky defects, and protonating the oxygen sites, we propose four distinct charge-balanced hydrogen incorporation mechanisms in majorite. These mechanisms are $[\square_{Mg2}+2OH_{O5}]^X$, $[\square_{Mg3}+2OH_{O5}]^X$, $[\square_{Si2}+4OH_{O6}]^X$, and $[\square_{Si4}+2OH_{O2}+2OH_{O3}]^X$. The proposed mechanisms include the tetrahedral, octahedral, and dodecahedral sites. The defect structures, as optimized at zero-pressure using the force field approach, are shown in Fig. 24. We consider hydrogen incorporation into the dodecahedral site as $[\square_{Mg2}+2OH_{O5}]^X$, into the octahedral sites as either

$[\square_{Mg3}+2OH_{O5}]^X$ or $[\square_{Si4}+2OH_{O2}+2OH_{O3}]^X$, and into the tetrahedral site as the hydrogarnet-type defect $[\square_{Si2}+4OH_{O6}]^X$. The optimized hydrogarnet defect consists of the 4 H atoms lying outside of the Si-vacant tetrahedra along the edges and this configuration is confirmed by the DFT calculations. The other three optimized defects show the H atoms pointing inward toward the vacancy and region of negative charge. The DFT calculations also result in the H atoms pointing inward for the $[\square_{Mg3}+2OH_{O5}]^X$ defect. However, there is a difference in direction that the H atoms point. The force field calculations yield a configuration in which the H atoms lie in the plane formed by the O4 and O5 atoms with the H atoms pointing toward opposite O4 atoms (∠O5-H-O1 = ~110°). The DFT optimization results in the H atoms pointing toward opposite O1 atoms (∠O5-H-O1 = ~160°).

The $[\square_{Mg3}+2OH_{O5}]^X$ octahedral-based defect has formation energy 0.07 eV less than the dodecahedral-based $[\square_{Mg2}+2OH_{O5}]^X$ defect at zero-pressure (Fig. 25). The formation enthalpy difference between the two different Mg defects decreases to 0.01 eV at P = 25 GPa. Thus, our interpretation is that H-substitution balanced by Mg vacancies is as likely to occur at octahedral sites as it is to occur at dodecahedral sites. At P = 0 GPa, the hydrogarnet defect $[\square_{Si2}+4OH_{O6}]^X$ is 3.56 eV more favorable than hydrogen incorporation into the octahedral site that is normally occupied by silicon (Fig. 25). The enthalpy difference between the Si-based hydrogen defects increases with increasing pressure to 3.96 eV at 25 GPa, and therefore the octahedral defect is not expected at any relevant pressure. The enthalpy for reaction 4.6, which is used to compare the relative stability of the hydrogarnet defect with the $[\square_{Mg3}+2OH_{O5}]^X$ defect, is negative at all pressures (Fig. 26) indicating that the hydrogarnet defect should be significantly more

stable in majorite at mantle pressures. The stability of the hydrogarnet defect is verified by the DFT calculations (Table 11). The partitioning of hydrogen between the Mg3 sites and Si2 sites can be calculated from the equilibrium constant, *K*, of reaction 4.6 as

$$D^{Si2/Mg3} = K = \exp\frac{-\Delta G}{RT} \sim \exp\frac{-\Delta H}{RT} \quad (4.8)$$

Because of a greater number of configurations with the Mg site over the Si site, entropic effects will increase ΔG at high temperatures. Therefore, as an upper bound, the partition coefficient at 20 GPa and 1800 K is $D^{\mathrm{Si2/Mg3}} \approx 200$.

4.3.4. Effect of Al on OH incorporation

Al is most likely to be incorporated into the majorite structure at either the Si2 tetrahedral or the octahedral sites: the Al_{Si4}' defect has a formation enthalpy that is only 0.13 eV less than that of the Al_{Si2}' defect at zero-pressure and their enthalpies are equal to each other at 25 GPa. The $Al_{Mg3}^{\cdot}$ defect has a formation enthalpy that is at least 1.1 eV less than the enthalpy associated with Al substitution for dodecahedral Mg over the entire pressure range. Therefore, we propose that Al is incorporated into majorite via a coupled substitution with octahedral Mg and either octahedral Si4 or tetrahedral Si2. We calculate the formation enthalpy of the $[\square_{Mg3}+2OH_{O5}]^X$ defect and the $[\square_{Si2}+4OH_{O6}]^X$ hydrogarnet defect in the presence of a coupled Al-substitution either as $[Al_{Mg3}+Al_{Si2}]^X$ or $[Al_{Mg3}+Al_{Si4}]^X$. Based on the mass-balanced reactions

$$Mg_{32N\text{-}1}Si_{32N}O_{96N}H_2 + Al_2O_3 \leftrightarrow Mg_{32N\text{-}1}Al_2Si_{32N\text{-}1}O_{96N}H_2 + MgSiO_3 \quad (4.9)$$

and

$$Mg_{32N}Si_{32N\text{-}1}O_{96N}H_4 + Al_2O_3 \leftrightarrow Mg_{32N\text{-}1}Al_2Si_{32N\text{-}2}O_{96N}H_4 + MgSiO_3 \quad (4.10)$$

where Al_2O_3 is corundum and $MgSiO_3$ is majorite, both the $[\square_{Mg3}+2OH_{O5}]^X$ and the $[\square_{Si2}+4OH_{O6}]^X$ are more stable in the presence of a coupled Al-substitution at all

pressures (Fig. 27). Additionally, according to reaction 4.7 (Fig. 26), the presence of Al serves to further stabilize the hydrogarnet defect relative to the $[\square_{Mg3}+2OH_{O5}]^{X}$. The reaction enthalpy as a function of pressure for reactions 4.6 and 4.7 goes through a maximum due to the coesite-stishovite phase transition in SiO_2. The maximum in reaction 4.6 occurs at 10–15 GPa but in reaction 4.7 it occurs at 7.5–10 GPa. We interpret this as the hydrogarnet defect being more energetically favorable at lower pressures in the presence of Al.

4.3.5. Influence of defect-defect interactions

Comparison of the defect energies associated with both the single unit cell and 2 × 2 × 2 supercell of Al-free majorite shows that interaction of periodic images of the hydrogen defects is insignificant ($\Delta H_{def} \leq 0.03$ eV) (Fig. 25). The defect-defect interactions in aluminous majorite are more significant with the supercell calculations (0.4 wt% Al_2O_3) resulting in hydrous defect formation enthalpies that are up to 0.39 eV greater than the calculations using a single unit-cell (3.2 wt% Al_2O_3).

4.3.6. Wave speeds in hydrous majorite

To examine quantities that could provide geophysical evidence of hydrogen incorporation in garnet in the upper mantle and transition zone, the Voigt-Reuss-Hill averages of the bulk and shear moduli were calculated from the elastic constants (Anderson 1963) derived from the force field calculations (Table 8) along with the compressional and shear acoustic velocities, v_p and v_s. There is a negligible effect of water on both v_p and v_s for majorite with 700–1400 ppm wt H_2O at 25 GPa (Fig. 28). At these concentrations, body wave speeds are reduced by only ~0.2%, unlikely to be detectable by seismological measurements within the limits of radial seismic profile

uncertainties (Matas et al. 2007). When normalized to the same water concentration (1400 ppm wt H_2O) over the pressure range of this study, the shear modulus of majorite with the $[\square_{Si2}+4OH_{O6}]^X$ defect is 0.3% greater than with the $[\square_{Mg3}+2OH_{O5}]^X$ defect. There is even less of a difference between the bulk moduli (<0.2%) and no difference between the densities as a function of defect mechanism. Significant effects on body-wave speeds can only be seen at concentrations of >0.5 wt% water with reductions in v_p and v_s of 1–2% at transition zone pressures. However, such concentrations of water in majoritic garnets are unlikely in Earth's mantle (Beran and Libowitzky 2006).

4.4. Discussion

Bolfan-Casanova et al. (2000) synthesized tetragonal $MgSiO_3$ majorite at 17.5 GPa and ~1800 K with ~680 ppm wt H_2O. They argue against the hydrogarnet substitution based on the IR spectra citing the volume expansion of the Si-O tetrahedra (Lager et al. 1989) and energetic feasibility of the hydrogarnet defect formation only at large water contents (Rossman and Aines 1991). The OH-absorption band in synthetic majorite (Bolfan-Casanova et al. 2000) is centered 80 cm^{-1} lower and is 65 cm^{-1} broader compared to the hydrogarnet OH-absorption band in pyrope synthesized at high pressure (Withers et al. 1998). The volume expansion of the tetrahedra in andradite garnets (Lager et al. 1989) has been used to explain the apparent abrupt dewatering of pyrope at high pressure (Withers et al. 1998). However, a more recent study (Mookherjee and Karato 2010) shows that pyrope does not dewater abruptly at P = ~7 GPa. Natural grossular garnets with low-OH contents have complex IR spectra and are thus proposed to have substitution of H at the dodecahedral and octahedral site but no evidence for these substitutions was presented (Rossman and Aines 1991). Our results show that even at

low-water contents, the hydrogarnet defect is likely to form in majorite. Synthesis of majorite in the MORB+H_2O system results in a sharp peak centered at 3580 cm^{-1} (Katayama et al. 2003), which is only 20 cm^{-1} lower than the hydrogarnet substitution in synthetic pyrope (Ackermann et al. 1983). For the hydrogarnet defect in majorite (P = 0 GPa), our calculated bond lengths using force field methods, d(O-O) = 2.83 and 3.24 Å for the shared and unshared edges, are shorter than those in grossular [d(O-O) = 3.08 and 3.29 Å] also calculated using interatomic potentials (Wright et al. 1994). Thus, the incorporation of hydrogen through the hydrogarnet defect causes a greater tetrahedral volume expansion in grossular than in majorite due to a greater lengthening of the 2 shared tetrahedral edges. This greater lengthening of the shared edges in grossular is energetically favorable due to Ca, with its larger ionic radius, occupying the dodecahedral sites. Additionally, our DFT optimizations of the hydrogarnet defect result in d(H···O) = 2.26–2.34 Å, which is shorter than d(H···O) = 2.49–2.62 Å and d(H···O) = ~2.23–2.54 Å for katoite and hydropyrope calculated in a previous first-principles study (Nobes et al. 2000). The shorter d(H···O) in majorite relative to hydropyrope is related to the O-H···O angle. The longer calculated distances in hydroyrope are associated with O-H···O = 113–120° compared to 146–147° in our majorite calculations. Based on shorter O···O and H···O distances, we expect the OH-stretching vibrational frequency to be lower in majorite when compared to other garnets (Libowitzky 1999). Thus it appears that the variation in the vibrational peak positions for the hydrogarnet defect in garnet can be attributed to differences in major and trace element chemistry and possibly the presence of an additional substitution mechanism.

Our calculated defect binding energies show that isolated hydroxyl groups are unlikely in the majorite structure and hydrogen is associated with cation vacancies. The defect binding energies for protonation of the ^{VI}Mg site and the formation of the hydrogarnet defect are calculated according to the reactions

$$\square_{Mg3}'' + OH_{O5}^{\cdot} + OH_{O5}^{\cdot} \rightarrow [\square_{Mg3} + 2OH_{O5}]^{X} \quad (4.11)$$

and

$$\square_{Si}'''' + OH_{O5}^{\cdot} + OH_{O5}^{\cdot} + OH_{O5}^{\cdot} + OH_{O5}^{\cdot} \rightarrow [\square_{Si} + 4OH_{O}]^{X} \quad (4.12)$$

The energetics for formation of the hydrogarnet and $[\square_{Mg3}+2OH_{O5}]^{X}$ defects are thus −2.19 and −1.09 eV/H at zero-pressure. The binding energies become more exothermic with increasing pressure to −2.87 and −1.64 eV/H at 25 GPa confirming that isolated defects become less favorable at high pressure. The preferential formation of the hydrogarnet defect is consistent with atomistic simulations of hydrogen defect formation in ringwoodite (Blanchard et al. 2005). However, Blanchard et al. (2005) show a significantly greater driving force for hydrogen to be bound to cation vacancies in ringwoodite with defect binding energies of −15.80 and −10.36 eV/H. This is consistent with the greater H_2O storage capacity of ringwoodite (e.g., Bolfan-Casanova 2005).

We also compare the relative defect energies of the two defect mechanisms through the reaction of majorite with water as

$$H_2O + Mg_{Mg}^{X} + 2O_{O}^{X} = [\square_{Mg3} + 2OH_{O5}]^{X} + MgO \quad (4.13)$$

$$H_2O + Si_{Si}^{X} + 4O_{O}^{X} = [\square_{Si2} + 4OH_{O6}]^{X} + SiO_2 \quad (4.14)$$

The reaction energies are thus calculated according to

$$E_{12} = E_{\text{Mg-OH}} + E_{PT} + U_{MgO} \quad (4.15)$$

$$E_{13} = E_{\text{Hydrogarnet}} + 2E_{PT} + U_{SiO2} \quad (4.16)$$

where E_{PT} is the proton transfer energy and assumed to be −9.74 eV at zero-pressure. The derivation of E_{PT} and the full Born-Haber thermochemical cycle for hydrolysis reactions can be found elsewhere (Catlow 1977; Wright et al. 1994). Our zero-pressure calculations show that the hydrogarnet defect is more favorable by 1.44 eV with large negative energies of −6.51 and −7.95 eV/H for reactions 4.12 and 4.13. Thus, it is possible that both types of defects occur in majorite with the hydrogarnet defect likely to be dominant. This is consistent with IR spectra that show a deviation from a strict hydrogarnet substitution (Bolfan-Casanova et al. 2000). Atomistic simulations of defect mechanisms in the olivine polymorphs also show that one defect mechanism tends to be favored over the other. In the case of ringwoodite, both mechanisms are energetically favorable with reaction energies of −3.08 and −6.49 eV/H (Blanchard et al. 2005) and as with majorite, the hydrogarnet is more likely to be dominant. The hydrogarnet defect is also likely to occur in olivine with a reaction energy of 0.4 eV/H compared to 1.5 eV/H for the $[\square_{Mg}+2OH_O]^X$ defect (Walker et al. 2006). Conversely, the $[\square_{Mg}+2OH_O]^X$ is 5 eV more favorable than the hydrogarnet defect in wadsleyite (Walker et al. 2006).

Comparison of our DFT-GGA results at 20 GPa (Table 11) with the work of Panero (2010) confirms that the hydrogarnet defect is more likely to occur in majorite than in ringwoodite. The $[\square_{Mg}+2OH_O]^X$ defect is 0.54 eV/H more favorable in ringwoodite than in majorite, while the hydrogarnet defect formation enthalpy in majorite is 0.12 eV/H less than in ringwoodite. Reaction 4.3 shows that the hydrogarnet defect is more stable in ringwoodite by 0.17 eV/H (Panero 2010) compared to 0.82 eV/H in majorite.

The stability of the hydrous defects relative to the anhydrous phase in the presence of free H_2O at high pressure can be accomplished through static calculations using Ice VIII (Panero 2006). The following reactions at 20 GPa are considered

$$Mg_{31}Si_{32}O_{96}H_2 + MgO \rightarrow H_2O \text{ (Ice VIII)} + Mg_{32}Si_{32}O_{96} \quad (4.17)$$

and

$$Mg_{32}Si_{31}O_{96}H_4 + SiO_2 \text{ (stishovite)} \rightarrow 2\ H_2O \text{ (Ice VIII)} + Mg_{32}Si_{32}O_{96} \quad (4.18)$$

resulting in calculated static reaction enthalpies of −1.88 and −0.47 eV, respectively. Considering the heat of fusion of H_2O at ambient conditions (0.06 eV) and assuming the Dulong-Petit limit, the relative enthalpy of reaction 4.17 increases to 0.09 eV at 20 GPa and 2000 K. However, this represents an upper bound because the entropic effects of supercritical water are not considered here. Thus it appears more likely that the hydrogarnet defect will be stable at transition zone conditions and the $[\square_{Mg}+2OH_O]^X$ defect may not occur at high-*P*-*T* in the presence of water. This supports the interpretation that it is solely the hydrogarnet defect found in the IR spectra of Katayama et al. (2003).

It is possible that there are other H-defect mechanisms in majorite besides those considered here. Zhang and Wright (2010) show that coupled substitutions of Al and H into forsterite favors hydrogen substitution at the Si site by 1–2 eV/H. Our calculations show that the presence of Al stabilizes the hydrogarnet defect by 2.2–2.4 eV/H (Fig. 26). However, Mookherjee and Karato (2010) propose that water is incorporated into pyrope at high-water contents through the $[(Al+H)_{Si}]^X$ defect.

Majoritic garnet found in diamond inclusions originating from transition zone depths have been found to contain ~1 wt% Na_2O coupled with ~15–20 wt%

Al_2O_3 (Stachl 2001). However, these garnet inclusions are most likely anhydrous with the weight percent of major and minor element oxides summing to >100%. Zhang and Wright (2012) show that the presence of $Al^{3+}$and the monovalent Li ion may increase the potential of olivine to incorporate water, with the hydrogarnet defect being particularly favorable. Therefore it may be possible that coupled substitution of Na^{+} and Al^{3+} promotes hydrogen uptake in garnet as well.

The presence of iron in majorite may also affect the type of defect mechanism present in majorite. Atomistic simulations show that in reducing environments, it is favorable for water to be incorporated at vacant oxygen sites formed through reduction of ferric iron to ferrous iron (Wright and Catlow 1994). Indeed, incorporation of water in olivine through Fe redox exchange has been observed experimentally (Demouchy and Mackwell 2006). However, IR-spectra of Fe-bearing ringwoodite collected at high pressure (>20 GPa) and low temperature (5 K) show that water is incorporated at both the octahedral site and through the hydrogarnet defect with multiple defect mechanisms leading to the broad OH-absorption band observed in ringwoodite at higher temperatures (Panero et al. 2013). Therefore, we predict that the hydrogarnet defect is the most stable and dominant defect mechanism in majorite, with the presence of multiple defect mechanisms likely.

4.5. Implications

The partitioning of water between mineral phases of the transition zone depends upon the type of defect mechanism present in each phase (Keppler and Bolfan-Casanova 2006). If both ringwoodite and majorite incorporate water mainly through the hydrogarnet substitution, partitioning between the two phases is independent of water

fugacity. Considering that ~1.4 wt% H_2O has been observed in a natural ringwoodite inclusion in a diamond from the transition zone (Pearson et al. 2014), this suggests that majorite in the transition zone may contain 700 ppm water, at least locally in the CH_4-rich environments that are conducive to diamond formation. Majorite with water concentrations this large have been shown to be stable in synthesis experiments at lower transition zone pressure-temperature conditions (Bolfan-Casanova et al. 2000; Katayama et al. 2003).

Lateral heterogeneities in seismic wave speeds in the Earth's upper mantle can be caused by both variations in composition and temperature. The $R(H_2O)$ ratio of $d\ln(v_s)/d(H_2O)$ and $d\ln(v_p)/d(H_2O)$ and the $R(T)$ ratio of $d\ln(v_s)/dT$ and $d\ln(v_p)/dT$ are useful to elucidate the underlying cause of mantle heterogeneities (Li et al. 2011). We calculate $R(H_2O)$ for Al-free majorite as

$$R(\mathrm{H_2O}) = \frac{\ln V_s(1400 \text{ ppm wt } \mathrm{H_2O}) - \ln V_s(\text{anhydrous})}{\ln V_p(1400 \text{ ppm wt } \mathrm{H_2O}) - \ln V_p(\text{anhydrous})} \quad (4.19)$$

The $R(T)$ value for majorite was calculated at 16 GPa such that

$$R(\mathrm{T}) = \frac{\ln V_s(1473 \text{ K}) - \ln V_s(300 \text{ K})}{\ln V_p(1473 \text{ K}) - \ln V_p(300 \text{ K})} \quad (4.20)$$

based on the ultrasonic measurements of Irifune et al. (2008). $R(H_2O)$ for ringwoodite was taken from Panero (2010) and Li et al. (2011). The Li et al. (2011) seismic ratios for olivine, wadslyeite, and ringwoodite were determined using experimental and calculated densities, and bulk and shear moduli (Inoue et al. 1998; Wang et al. 2003; Mao et al. 2008, 2010; Li et al. 2009; Liu et al. 2009; Tsuchiya and Tsuchiya 2009). Although water at the ~1000 ppm level has only a minor effect on the absolute body wave speeds (Fig. 28), our calculated $R(H_2O)$ values show that the presence of hydrated majorite is

observable (Fig. 29) within the typical seismic model uncertainty of ±0.15 (Karato and Karki 2001). The presence of Al has a significant effect on $R(H_2O)$, with our calculations showing that R decreases by ~0.2–0.4 in the presence of 3 wt% Al_2O_3 with the Al substituted into the octahedral sites. Additionally, seismic wave speeds are dependent upon the density, bulk modulus, and shear modulus thus the pressure dependence of R is particularly sensitive to the pressure derivatives of these parameters. In addition to pressure and temperature, compositional variations, such as variations in Fe content can strongly influence seismic ratios. However, even when considering the presence of Al, $R(H_2O)$ for majorite appears to be significantly different than the same ratio for ringwoodite at high pressures with a difference of 0.5–1.2 at 20 GPa. At the base of the transition zone, $R(H_2O)$ for majorite is indistinguishable from $R(T)$ of ringwoodite calculated by Li et al. (2011) using DFT. $R(T)$ for majorite is ~0.5–1.0 greater than our calculated $R(H_2O)$ for majorite. Our calculated $R(H_2O)$ for Al-free majorite is indistinguishable from that of olivine and wadsleyite up to 15 and 20 GPa but becomes significantly different in the presence of aluminum. Therefore, it appears that the effect of hydrated, aluminous majorite should be visible in the upper mantle and neglecting it may result in an overestimate of temperature anomalies

References

Ackermann, L., Cemic, L., and Langer, K. (1983) Hydrogarnet substitution in pyrope – a possible location for “water” in the mantle. Earth and Planetary Science Letters, 62, 208–214.

Akaogi, M., Oohata, M., Kojitani, H., and Kawaji, H. (2011) Thermodynamic properties of stishovite by low-temperature heat capacity measurements and the coesite-stishovite transition boundary. American Mineralogist, 96, 1325–1330.

Allegre, C., Poirier, J.-P., Humler, E., and Hofmann, A.W. (1995) The chemical composition of the Earth. Earth and Planetary Science Letters, 134, 515-526.

Amthauer, G., and Rossman, G.R. (1998) The hydrous component in andradite garnet. American Mineralogist, 83, 835–840.

Anderson, O.L. (1963) A simplified method for calculating Debye temperature from elastic constants. Journal of Physics and Chemistry of Solids, 24, 909–917.

Andrault, D., and Fiquet, G. (2001) Synchrotron radiation and laser heating in a diamond anvil cell. Review of Scientific Instruments, 72, 1283-1288.

Andrault, D., Angel, R.J., Mosenfelder, J.L., and Le Bihan, T. (2003) Equation of state of stishovite to lower mantle pressures, American Mineralogist, 88, 301–307.

Angel, R.J. (2000), Equations of state. In R.M. Hazen and R.T. Downs, Eds., High-Temperature and High-Pressure Crystal Chemistry, 41, p. 35–59, Reviews in Mineralogy and Geochemistry, Mineralogical Society of America, Chantilly, Virginia.

Angel, R.J., Finger, L.W., Hazen, R.M., Kanzaki, M., Weidner, D.J., Liebermann, R.C., and Veblen, D.R. (1989) Structure and twinning of single-crystal $MgSiO_3$ garnet synthesized at 17 GPa and 1800 °C. American Mineralogist, 74, 509–512.

Angel. R.J., Allan, D.R., Miletich, R., and Finger, L.W. (1997) The use of quartz as an internal pressure standard in high-pressure crystallography. Journal of Applied Crystallography, 30, 461–466.

Angel, R.J., Mosenfelder, J.L., and Shaw, C.S.J. (2001) Anomalous compression and equation of state of coesite. Physics of the Earth and Planetary Interiors, 124, 71–79.

Balan, E., Blanchard, M., Lazzeri, M., and Ingrin, J. (2014) Contribution of interstitial OH groups to the incorporation of water in forsterite. Physics and Chemistry of Minerals, 41, 105–114.

Bass, J.D., Liebermann, R.C., Weidner, D.J., and Finch, S.J. (1981) Elastic properties from acoustic and volume compression experiments. Physics of the Earth and Planetary Interiors, 25, 140–158.

Bell, D.R., and Rossman, G.R. (1992a) Water in Earth's mantle - the role of nominally anhydrous minerals. Science, 251, 1391–1397.

Bell, D.R., and Rossman, G.R. (1992b) The distribution of hydroxyl in garnets from the subcontinental mantle of southern Africa. Contributions to Mineralogy and Petrology, 111, 161–178.

Beran, A., and Libowitzky, E. (2006) Water in natural mantle minerals II: Olivine, garnet and accessory minerals. In H. Keppler and J.R. Smyth, Eds., Water in Nominally Anhydrous Minerals, 62, p. 169–191, Reviews in Mineralogy and Geochemistry, Mineralogical Society of America, Chantilly, Virginia.

Bina, C.R., and Navrotsky, A. (2001) Possible presence of high-pressure ice in cold subducting slabs. Nature, 408, 844–847.

Birch, F. (1952) Elasticity and constitution of the Earth's interior. Journal of Geophysical Research, 57, 227–286.

Bish, D.L. (1993) Rietveld refinement of the kaolinite structure at 1.5 K. Clays and Clay Minerals, 41, 738–744.

Blanchard, M., Wright, K., and Gale, J.D. (2005) A computer simulation study of OH defects in Mg_2SiO_4 and Mg_2GeO_4 spinels. Physics and Chemistry of Minerals, 32, 585–593.

Boehler, R. (1993) Temperatures in the Earth's core from melting-point measurements of iron at high static pressures. Nature, 363, 534-536.

Bolfan-Casanova, N. (2005) Water in the Earth's mantle. Mineralogical Magazine, 69, 229–257.

Bolfan-Casanova, N., Keppler, H., and Rubie, D.C. (2000) Water partitioning between nominally anhydrous minerals in the MgO-SiO_2-H_2O system up to 24 GPa: implications

for the distribution of water in the Earth's mantle. Earth and Planetary Science Letters, 182, 209–221.

Campbell, A.J., Danielson, L., Righter, K., Seagle, C.T., Wang, Y., and Prakapenka V.B. (2009) High pressure effects on the iron–iron oxide and nickel–nickel oxide oxygen fugacity buffers. Earth and Planetary Science Letters, 286, 556–564.

Catlow, C.R.A. (1977) Oxygen incorporation in alkaline-Earth fluorides. Journal of Physics and Chemistry of Solids, 38, 1131–1136.

Catlow, C.R.A., Faux, I.D., and Norgett, M.J. (1976) Shell and breathing shell model calculations for defect formation energies and volumes in magnesium oxide. Journal of Physics C-Solid State Physics, 9, 419–429.

Catti, M., Ferris, G., Hull, S., and Pavese, A. (1995) Static compression and H disorder in brucite, $Mg(OH)_2$, to 11 GPa: a powder neutron diffraction study. Physics and Chemistry of Minerals, 22, 200–206.

Chopin, C. (2003) Ultrahigh-pressure metamorphism: tracing continental crust into the mantle. Earth and Planetary Science Letters, 212, 1–14.

Côté, A.S., Vočadlo, L., and Brodholt, J.P. (2012) Ab initio simulations of iron–nickel alloys at Earth's core conditions. Earth and Planetary Science Letters, 345–348, 126–130.

Decker, D.L. (1971) High pressure equation of state for NaCl, KCl, and CsCl. Journal of Applied Physics, 42, 3239–3244.

Demouchy, S., and Mackwell, S. (2006) Mechanisms of hydrogen incorporation and diffusion in iron-bearing olivine. Physics and Chemistry of Minerals, 294, 347–355.

Dewaele, A., Loubeyre, P., Occelli, F., Mezouar, M., Dorogokupets, P.I., and Torrent, M. (2006) Quasihydrostatic equation of state of iron above 2 Mbar. Physical Review Letters, 97, 215504.

Dewaele, A., Torrent, M., Loubeyre, P., and Mezouar, M. (2008) Compression curves of transition metals in the Mbar range: Experiments and projector augmented-wave calculations. Physical Review B, 78, 104102.

Dick, B.G. Jr., and Overhauser, A.W. (1958) Theory of the dielectric constants of alkali halide crystals. Physical Review, 112, 90–103.

Dziewonski, A., and Anderson, D. (1981) Preliminary Reference Earth Model. Physics of the Earth and Planetary Interiors, 25, 297–356.

Endo, S., Akai, T., Akahama, Y., Wakatsuki, M., Nakamura, T., Tomii, Y., Koto, K., Ito, Y., and Tokonami, M. (1986) High temperature x-ray study of single crystal stishovite synthesized with Li_2WO_4 as flux. Physics and Chemistry of Minerals, 13, 146–151.

Fei, Y., Li, J., Hirose, K., Minarik, W., Van Orman, J., Sanloup, C., van Westrenen, W., Komabayashi, T., and Funakoshi, K.-i. (2004) A critical evaluation of pressure scales at high temperatures by in situ X-ray diffraction measurements. Physics of the Earth and Planetary Interiors, 143-144, 515-526.

Fei, Y., Ricolleau, A., Frank, M., Mibe, K., Shen, G., and Prakapenka, V. (2007) Toward an internally consistent pressure scale. Proceedings of the National Academy of Sciences USA, 104, 9182–9186.

Finger, L.W., and Hazen, R.M. (1978) Crystal structure and compression of ruby to 46 kbar. Journal of Applied Physics, 49, 5823.

Fleming, S., and Rohl, A. (2005) GDIS: a visualization program for molecular and periodic systems. Zeitschrift für Kristallographie, 220, 580–584.

Frost, D.J. (2008) The upper mantle and transition zone. Elements, 4, 171–176.

Fukao, Y., Obayashi, M., Nakakuki, T., and the Deep Slab Project Group (2009) Stagnant slab: A review. Annual Review of Earth and Planetary Sciences, 37, 19–46.

Gale, J.D., and Rohl, A.L. (2003) The general utility lattice program (GULP). Molecular Simulation, 29, 291–341.

Gerstl, S.S.A., Morrone, A., and Kvitek, R. (2006) Three-dimensional nanoscale characterization of Pt deposition from an organometallic precursor induced by a focused ion beam. Microscopy and Microanalysis, 12, 1252-1253.

Gwamnesia, G.D., Chen, G., and Liebermann, R.C. (1998) Sound velocities in $MgSiO_3$-garnet to 8 GPa. Geophysical Research Letters, 25, 4553–4556.

Han, Y., Gao, C., Ma, Y., Liu, H., Pan, Y., Luo, J., Li, M., He, C., Huang, X., Zou, G., Li, Y., Li, X., and Liu, J. (2005) Integrated microcircuit on a diamond anvil for high-pressure electrical resistivity measurement. Applied Physics Letters, 86, 064104.

Hazen, R.M. (1976) Effects of temperature and pressure on cell dimension and x-ray temperature factors of periclase. American Mineralogist, 61, 266–271.

Hirose, K., Fei, Y., Ma, Y., and Mao, H.-K. (1999), The fate of subducted basaltic crust in the Earth's lower mantle. Nature, 397, 53–56.

Hirose, K., Takafuji, N., Sata, N., and Ohishi Y. (2005) Phase transition and density of subducted MORB crust in the lower mantle. Earth and Planetary Sciences Letters, 237, 239–251.

Hirose, K., Labrosse, S., and Hernlund, J. (2013) Composition and state of the core. Annual Review of Earth and Planetary Sciences, 41, 657–691.

Hirschmann, M.M. (2006) Water, melting, and the deep Earth H_2O cycle. Annual Review of Earth and Planetary Sciences, 34, 629–653.

Holmes, N.C., Moriarty, J.A., Gathers, G.R., and Nellis, W.J. (1989) The equation of state of platinum to 660 GPa (6.6 Mbar). Journal of Applied Physics, 66, 2962-2967.

Inoue, T., Weidner, D.J., Northrup, P.A., and Parise, J.B. (1998) Elastic properties of hydrous ringwoodite (gamma-phase) in Mg_2SiO_4. Earth and Planetary Science Letters, 160, 107–113.

Irifune, T., and Ringwood, A. (1993) Phase-Transformations in subducted oceanic-crust and buoyancy relationships at depths of 600-800 km in the mantle. Earth and Planetary Science Letters, 117, 101–110.

Irifune, T., Isshiki, M., and Sakamoto, S. (2005) Transmission electron microscope observation of the high-pressure form of magnesite retrieved from laser heated diamond anvil cell. Earth and Planetary Science Letters, 239, 98-105.

Irifune, T., Higo, Y., Inoue, T., Kono, Y., Ohfuji, H., and Funakoshi, K. (2008) Sound velocities of majorite garnet and the composition of the mantle transition region. Nature, 451, 814–817.

Jackson, I., and Rigden, S.M. (1996) Analysis of *P-V-T* data: constraints on the thermoelastic properties of high-pressure minerals. Physics of the Earth and Planetary Interiors, 96, 85–112.

Jacobsen, S.D., Reichmann, H.-J., Spetzler, H.A., Mackwell, S.J., Smyth, J.R., Angel, R.J., and McCammon, C.A. (2002) Structure and elasticity of single-crystal (Mg,Fe)O and a new method of generating shear waves for gigahertz ultrasonic interferometry. Journal of Geophysical Research, 107, 2037.

Jiang, F., Speziale, S., and Duffy, T.S. (2006) Single-crystal elasticity of brucite, $Mg(OH)_2$, to 15 GPa by Brillouin scattering. American Mineralogist, 91, 1893–1900.

Jorgenson, G.V., and Wehner, G.K. (1965) Sputtering studies of insulators by means of Langmuir probes. Journal of Applied Physics, 36, 2672 – 2674.

Karato, S. (2006) Remote sensing of hydrogen in Earth's mantle. In H. Keppler and J.R. Smyth, Eds., Water in Nominally Anhydrous Minerals, 62, p. 343–375, Reviews in Mineralogy and Geochemistry, Mineralogical Society of America, Chantilly, Virginia.

Karato, S., and Karki, B.B. (2001) Origin of lateral variation of seismic wave velocities and density in the deep mantle. Journal of Geophysical Research, 106, 21771–21783.

Katayama, I., Hirose, K., Yurimoto, H., and Nakashima, S. (2003) Water solubility in majoritic garnet in subducting oceanic crust. Geophysical Research Letters, 30, 2155.

Kavner, A., and Jeanloz, R. (1998) High-pressure melting curve of platinum. Journal of Applied Physics, 83, 7553-7559.

Kavner, A., and Panero, W.R. (2004) Temperature gradients and evaluation of thermoelastic properties in the synchrotron-based laser-heated diamond cell. Physics of the Earth and Planetary Interiors, 143-144, 527-539.

Keppler, H., and Bolfan-Casanova, N. (2006) Thermodynamics of water solubility and partitioning. In H. Keppler and J.R. Smyth, Eds., Water in Nominally Anhydrous Minerals, 62, p. 193–230, Reviews in Mineralogy and Geochemistry, Mineralogical Society of America, Chantilly, Virginia.

Kiefer, B., and Duffy, T.S. (2005) Finite element simulations of the laser-heated diamond-anvil cell. Journal of Applied Physics, 97, 114902.

Kirby, S.H., Stein, S., Okal, E.A., and Rubie, D.C. (1996) Metastable mantle phase transformations and deep earthquakes in subducting oceanic lithosphere. Reviews of Geophysics, 34, 261–306.

Knacke, O., Kubaschewski, O., and Hesselman, K. (1991) Thermochemical properties of inorganic substances, 2412 p. Springer-Verlag, Berlin.

Kohlstedt, D.L., Keppler, H., and Rubie, D.C. (1996) Solubility of water in the alpha, beta and gamma phases of $(Mg,Fe)_2SiO_4$. Contributions to Mineralogy and Petrology, 123, 345–357.

Kollie, T.G. (1977) Measurement of the thermal-expansion coefficient of nickel from 300 to 1000 K and determination of the power-law constants near the Curie temperature. Physical Review B, 16, 4872–4881.

Kresse, G., and Furthmüller, J. (1996a) Efficiency of ab-initio total energy calculations for metals and semiconductors using a plane-wave basis set. Computational Materials Science, 6, 15–50.

Kresse, G., and Furthmüller, J. (1996b) Efficient iterative schemes for ab initio total-energy calculations using a plane-wave basis set. Physical Review B, 54, 11169–11186.

Lager, G.A., Armbruster, T., Rotella, F.J., and Rossman, G.R. (1989) OH substitution in garnets: x-ray and neutron-diffraction, infrared, and geometric-modeling studies. American Mineralogist, 74, 840–851.

Levien, L., and Prewitt, C.T. (1981) High-pressure crystal structure and compressibility of coesite. American Mineralogist, 66, 324–333.

Levien, L., Prewitt, C.T., and Weidner, D.J. (1980) Structure and elastic properties of quartz at pressure. American Mineralogist, 65, 920–930.

Libowitzky, E. (1999) Correlation of O-H stretching frequencies and O-H…O hydrogen bond lengths in minerals. Monatshefte für Chemie, 130, 1047–1059.

Li, B., Rigden, S.M., and Liebermann, R.C. (1996) Elasticity of stishovite at high pressure. Physics of the Earth and Planetary Interiors, 96, 113–127.

Li, L., Brodholt, J., and Alfe, D. (2009) Structure and elasticity of hydrous ringwoodite: A first principle investigation. Physics of the Earth and Planetary Interiors, 177, 103–115.

Li, L., Weidner, D.J., Brodholt, J.P., and Alfe, D. (2011) Prospecting for water in the transition zone: dln(Vs)/dln(Vp). Physics of the Earth and Planetary Interiors, 189, 117–120.

Litasov, K.D., Ohtani, E., Ghosh, S., Nishihara, Y., Suzuki, A., and Funakoshi, K. (2007) Thermal equation of state of superhydrous phase B to 27 GPa and 1373 K. Physics of the Earth and Planetary Interiors, 164, 142–160.

Liu, J., Chen, G., Gwamnesia, G.D., and Lieberman, R.C. (2000) Elastic wave velocities of pyrope-majorite garnets ($Py_{62}Mj_{38}$ and $Py_{50}Mj_{50}$) to 9 GPa. Physics of the Earth and Planetary Interiors, 120, 153–163.

Liu, L., Du, J., Zhao, J., Liu, H., Gao, H., and Chen, Y. (2009) Elastic properties of hydrous forsterites under high pressure: first-principle calculations. Physics of the Earth and Planetary Interiors, 176, 89–97.

Luo, S.-N., Çağin, T., Strachan, A., Goddard III, W.A., and Ahrens, T.J. (2002) Molecular dynamics modeling of stishovite. Earth and Planetary Science Letters, 202, 147–157.

Mao, Z., Jacobsen, S.D., Jiang, F., Smyth, J.R., Holl, C.M., and Duffy, T.S. (2008) Elasticity of hydrous wadsleyite to 12 GPa: implications for Earth's transition zone. Geophysical Research Letters, 35, L21305.

Mao, Z., Jacobsen, S.D., Jiang, F., Smyth, J.R., Holl, C.M., Frost, D.J., and Duffy, T.S. (2010) Velocity crossover between hydrous and anhydrous forsterite at high pressures. Earth and Planetary Science Letters, 293, 250–258.

Marquardt, H., and Miyagi, L. (2015) Slab stagnation in the shallow lower mantle linked to an increase in mantle viscosity. Nature Geoscience, 8, 311 – 314.

Matas, J., Bass, J., Ricard, Y., Mattern, E., and Bukowinski, M.S.T. (2007) On the bulk composition of the lower mantle: predictions and limitations from generalized inversion of radial seismic profiles. Geophysical Journal International, 170, 764–780.

McDonough, W.F., and Sun, S.-s. (1995) The composition of the Earth. Chemical Geology, 120, 223–253.

Mei, J., Davenport, J.W., and Fernando, G.W. (1991) Analytic embedded-atom potentials for fcc metals: application to liquid and solid copper. Physical Review B, 43, 4653–4658.

Mellini, M., and Zanazzi, P.F. (1989) Effects of pressure on the structure of lizardite-1T. European Journal of Mineralogy, 1, 13–19.

Mookherjee, M., and Karato, S. (2010) Solubility of water in pyrope-rich garnet at high pressures and temperature. Geophysical Research Letters, 37, L03310.

Murphy, C.A., Jackson, J.M., Sturhahn, W., and Chen, B. (2011) Melting and thermal pressure of hcp-Fe from the phonon density of states. Physics of the Earth and Planetary Interiors, 188, 114–120.

Nakatsuka, A., Yoshiasa, A., Yamanaka, T., Ohtaka, O., Katsura, T., and Ito, E. (1999) Symmetry change of majorite solid-solution in the system $Mg_3Al_2Si_3O_{12}$-$MgSiO_3$. American Mineralogist, 84, 1135–1143.

Nguyen, J.H., and Holmes, N.C. (2004) Melting of iron at the physical conditions of the Earth's core, Nature, 427, 339–342.

Niu, F., Kwakatsu, H., Fukao, Y. (2003) Seismic evidence for a chemical heterogeneity in the midmantle: A slightly dipping and strong seismic reflector at mid-depth beneath the Mariana subduction zone. Journal of Geophysical Researsh,108, 2419.

Nobes, R.H., Akhmatskaya, E.V., Milman, V., White, J.A., Winkler, B., and Pickard, C.J. (2000) An ab initio study of hydrogarnets. American Mineralogist, 85, 1706–1715.

Nomura, R., Hirose, K., Sata, N., and Ohishi, Y. (2010) Precise determination of post-stishovite phase transition boundary and implications for seismic heterogeneities in the mid-lower mantle. Physics of the Earth and Planetary Interiors, 183, 104–109.

Ono, S., Kikegawa, T., and Ohishi, Y. (2005) A high-pressure and high-temperature synthesis of platinum carbide. Solid State Communications, 133, 55-59.

Orloff, J., Narayana, C., and Ruoff, A.L. (2000) Use of focused ion beams for making tiny sample holes in gaskets for diamond anvil cells. Review of Scientific Instruments, 71, 216-219.

Pacalo, R.E.G., and Weidner, D.J. (1996) Elasticity of superhydrous B. Physics and Chemistry of Minerals, 23, 520–525.

Pacalo, R.E.G., and Weidner, D.J. (1997) Elasticity of majorite, $MgSiO_3$ tetragonal garnet. Physics of the Earth and Planetary Interiors, 99, 145–154.

Panero, W.R. (2006) Aluminum incorporation in stishovite. Geophysical Research Letters, 33, L20317.

Panero, W.R. (2010) First principles determination of the structure and elasticity of hydrous ringwoodite. Journal of Geophysical Research, 115, B03203.

Panero, W.R., and Jeanloz, R. (2001a) The effect of sample thickness and insulation layers on the temperature distribution in the laser-heated diamond cell. Review of Scientific Instruments, 72, 1306-1308.

Panero, W.R., and Jeanloz, R. (2001b) Temperature gradients in the laser-heated diamond anvil cell. Journal of Geophysical Research, 106, 6493-6498.

Panero, W.R., Benedetti, L.R., and Jeanloz, R. (2003) Equation of state of stishovite and interpretation of SiO_2 shock-compression data. Journal of Geophysical Research, 108, doi:10.1029/2001JB001663.

Panero, W.R., Smyth, J.R., Pigott, J.S., Liu, Z., and Frost, D.J. (2013) Hydrous ringwoodite to 5 K and 35 GPa: multiple hydrogen bonding sites resolved with FTIR spectroscopy. American Mineralogist, 98, 637–642.

Pauling, L. (1980) The nature of silicon-oxygen bonds. American Mineralogist, 65, 321–323.

Pearson, D.G., Brenker, F.E., Nestola, F., McNeill, J., Nasdala, L., Hutchison, M.T., Matveev, S., Mather, K., Silversmit, G., Schmitz, S., Vekemans, B., and Vincze, L. (2014) Hydrous mantle transition zone indicated by ringwoodite included within diamond. Nature, 507, 221–229.

Perdew, J.P. (1991) Unified theory of exchange and correlation beyond the local density approximation, In P. Ziesche and H. Eschrig, Eds., Electronic Structure of Solids ’91, p. 11–20, Akademie Verlag, Berlin.

Perrillat, J.-P., Ricolleau, A., Daniel, I., Fiquet, G., Mezouar, M., Guignot, N., and Cardon, H. (2006) Phase transformations of subducted basaltic crust in the upmost lower mantle. Physics of the Earth and Planetary Interiors, 157, 139–149.

Pigott, J.S., Reaman, D.M., and Panero, W.R. (2011) Microfabrication of controlled-geometry samples for the laser-heated diamond-anvil cell using focused ion beam technology. Review of Scientific Instruments, 82, 115106.

Pigott, J.S., Wright, K., Gale, J.D., and Panero, W.R. (2015) Calculation of the energetics of water incorporation in majorite garnet. American Mineralogist, 100, 1065-1075.

Poli, S., and Schmidt, M.W. (2002) Petrology of subducted slabs. Annual Review of Earth and Planetary Sciences, 30, 207 – 235.

Purton, J., Jones, R., Heggie, M., Öberg, S., and Catlow, C.R.A. (1992) LDF pseudopotential calculations of the alpha-quartz structure and hydrogarnet defect. Physics and Chemistry of Minerals, 18, 389–392.

Rainey, E.S.G., Hernlund, J.W., and Kavner, A. (2013) Temperature distributions in the laser-heated diamond anvil cell from 3-D numerical modeling. Journal of Applied Physics, 114, 204905.

Reaman, D.M., Colijn, H.O., Yang, F., Hauser, A.J., and Panero, W.R. (2012) Interdiffusion of Earth's core materials to 65 GPa and 2200 K. Earth and Planetary Science Letters, 349–350, 8–14.

Ross, N.L., Shu, J.-F., Hazen, R.M., and Gasparik, T. (1990) High-pressure crystal chemistry of stishovite. American Mineralogist, 75, 739–747.

Rossman, G.R., and Aines, R.D. (1991) The hydrous components in garnets: grossular-hydrogrossular. American Mineralogist, 76, 1153–1164.

Runge, C.E., Kubo, A., Kiefer, B., Meng, Y., Prakapenka, V.B., Shen, G., Cava, R.J., and Duffy, T.S. (2006) Equation of state of $MgGeO_3$ perovskite to 65 GPa: comparison with the post-perovskite phase. Physics and Chemistry of Minerals, 33, 699–709.

Sakai, T., Takahasi, S., Nishitani, N., Mashino, I., Ohtani, E., and Hirao, N. (2014) Equation of state of pure iron and $Fe_{0.9}Ni_{0.1}$ alloy up to 3 Mbar. Physics of the Earth and Planetary Interiors, 228, 114–126.

Saul, P., Catlow, C.R.A., and Kendrick, J. (1985) Theoretical studies of protons in sodium hydroxide. Philosophical Magazine B, 51, 107–117.

Schröder, K.-P., Sauer, J., Leslie, M., Catlow, C.R.A., and Thomas, J.M. (1992) Bridging hydroxyl-groups in zeolitic catalysts: a computer simulation of their structure, vibrational

properties and acidity in protonated faujasites (H-Y zeolites). Chemical Physics Letters, 88, 320–325.

Shen, G., Mao, H.-k., Hemley, R.J., Duffy, T.S., and Rivers, M.L. (1998) Melting and crystal structure of iron at high pressures and temperatures. Geophysical Research Letters, 25, 373-376.

Sinogeikin, S.V., Bass, J.D., O'Neill, B., and Gasparik, T. (1997a) Elasticity of tetragonal end-member majorite and solid solutions in the system $Mg_4Si_4O_{12}$-$Mg_3Al_2Si_3O_{12}$. Physics and Chemistry of Minerals, 24, 115–121.

Sinogeikin, S.V., Bass, J.D., Kavner, A., and Jeanloz, R. (1997b) Elasticity of natural majorite and ringwoodite from the Catherwood meteorite. Geophysical Research Letters, 24, 3265–3268.

Sinogeikin, S.V., and Bass, J.D. (2000) Single-crystal elasticity of pyrope and MgO to 20 GPa by Brillouin scattering in the diamond cell. Physics of the Earth and Planetary Interiors, 120, 43–62.

Sinogeikin, S.V., and Bass, J.D. (2002) Elasticity of majorite and a majorite-pyrope solid solution to high pressure: implications for the transition zone. Geophysical Research Letters, 29, 1017.

Smyth, J.R., and Jacobsen, S.D. (2006) Nominally Anhydrous Minerals and Earth's Deep Water Cycle. In S.D. Jacobsen and S. van der Lee, Eds., Earth's Deep Water Cycle, 168, p. 1–11, Geophysical Monograph Series, American Geophysical Union, Washingtion, D.C.

Smyth, J.R., Holl, C.M., Frost, D.J., and Jacobsen, S.D. (2004) High pressure crystal chemistry of hydrous ringwoodite and water in the Earth's interior. Physics of the Earth and Planetary Interiors, 143–144, 271-278.

Speziale, S., Zha, C.-S., Duffy, T.S., Hemley, R.J., and Mao, H.-k. (2001) Quasi-hydrostatic compression of magnesium oxide to 52 GPa: Implications for the pressure-volume-temperature equation of state. Journal of Geophysical Research, 106, 515–528.

Stacey, F.D., and Davis, P.M. (2008) Physics of the Earth, 532 p. Cambridge University Press, Cambridge.

Stachl, T. (2001) Diamonds from the asthensosphere and the transition zone. European Journal of Mineralogy, 13, 883–892.

Stixrude, L., and Lithgow-Bertelloni, C. (2007) Influence of phase transformations on lateral heterogeneity and dynamics in Earth's mantle. Earth and Planetary Science Letters, 263, 45–55.

Syracuse, E.M., van Keken, P.E., and Abers, G.A. (2010) The global range of subduction zone thermal models. Physics of the Earth and Planetary Interiors, 183, 73–90.

Tang, X., and Dong, J. (2010) Lattice thermal conductivity of MgO at conditions of Earth's interior. Proceedings of the National Academy of Sciences USA, 107, 4539–4543.

Tateno, S., Hirose, K., Ohishi, Y., and Tatsumi, Y. (2010) The structure of iron in Earth's inner core. Science, 330, 359–361.

Terada, Y., Ohkubo, K., and Mohri, T. (2005) Thermal conductivities of platinum alloys at high temperatures. Platinum Metals Review, 49, 21–26.

Thomas, S.-M., Bina, C.R., Jacobsen, S.D., and Goncharov, A.F. (2012) Radiative heat transfer in a hydrous mantle transition zone. Earth and Planetary Science Letters, 357-358, 130–136.

Tsuchiya, T. (2003) First-principles prediction of the *P-V-T* equation of state of gold and the 660-km discontinuity in Earth's mantle. Journal Geophysical Research, 108, 2462.

Tsuchiya, T., and Kawamura, K. (2002) First-principles electronic thermal pressure of metal Au and Pt. Physical Review B, 66, 094115.

Tsuchiya, J., and Tsuchiya, T. (2009) First principles investigation of the structural and elastic properties of hydrous wadsleyite under pressure. Journal of Geophysical Research, 114, B02206.

Tsujino, N., Nishihara, Y., Nakajima, Y., Takahashi, E., Funakoshi, K.-i., and Higo, Y. (2013) Equation of state of γ-Fe: Reference density for planetary cores. Earth and Planetary Science Letters, 375, 244–253.

Uchida, T., Wang, Y., Rivers, M.L., and Sutton, S.R. (2001) Stability field and thermal equation of state of ε-iron determined by synchrotron x-ray diffraction in a multianvil apparatus. Journal Geophysical Research, 106, 21799–21810.

Vinograd, V.L., Winkler, B., Putnis, A., Kroll, H., Milman, V., Gale, J.D., and Fabrichnaya, O.B. (2006) Thermodynamics of pyrope-majorite, $Mg_3Al_2Si_3O_{12}$-$Mg_4Si_4O_{12}$, solid solution from atomistic model calculations. Molecular Simulation, 32, 85–99.

Walker, A.M., Demouchy, S., and Wright, K. (2006) Computer modelling of the energies and vibrational properties of hydroxyl groups in alpha- and beta-Mg_2SiO_4. European Journal of Mineralogy, 18, 529–543.

Wang, F., Tange, Y., Irifune, T., and Funakoshi, K.-i. (2012) *P-V-T* equation of state of stishovite up to mid-lower mantle conditions. Journal of Geophysical Research, 117, B06209.

Wang, J., Sinogeikin, S.V., Inoue, T., and Bass, J.D. (2003) Elastic properties of hydrous ringwoodite. American Mineralogist, 88, 1608–1611.

Wang, Z., Wang, H., and Cates, M.E. (2001) Effective elastic properties of solid clays. Geophysics, 66, 428–440.

Weidner, D.J., and Carleton, H.R. (1977) Elasticity of coesite. Journal of Geophysical Research, 82, 1334–1346.

Williams, Q., and Hemley, R.J. (2001) Hydrogen in the deep earth. Annual Review of Earth and Planetary Sciences, 29, 365–418.

Wirth, R. (2004) Focused Ion Beam (FIB): A novel technology for advanced application of micro- and nanoanalysis in geosciences and applied mineralogy. European Journal of Mineralogy, 16, 863-876.

Withers, A.C., Wood, B.J., and Carroll, M.R. (1998) The OH content of pyrope at high pressure. Chemical Geology, 147, 161–171.

Wright, K. (2006) Atomistic models of OH defects in nominally anhydrous minerals. Water in Nominally Anhydrous Minerals, In H. Keppler and J.R. Smyth, Eds., Water in Nominally Anhydrous Minerals, 62, p. 67–83, Reviews in Mineralogy and Geochemistry, Mineralogical Society of America, Chantilly, Virginia.

Wright, K., and Catlow, C.R.A. (1994) A computer simulation study of (OH) defects in olivine. Physics and Chemistry of Minerals, 20, 515–518.

Wright, K., Freer, R., and Catlow, C.R.A. (1994) The energetics and structure of the hydrogarnet defect in grossular: a computer simulation study. Physics and Chemistry of Minerals, 20, 500–503.

Xia, X., Weidner, D.J., and Zhao, H. (1998) Equation of state of brucite: single-crystal Brillouin spectroscopy study and polycrystalline pressure-volume-temperature measurement. American Mineralogist, 83, 68–74.

Xu, L., Mei, S., Dixon, N., Jin, Z., Suzuki, A.M., and Kohlstedt, D.L. (2013) Effect of water on rheological properties of garnet at high temperatures and pressures. Earth and Planetary Science Letters, 379, 158–165.

Yagi, T., Uchiyama, Y., Akaogi, M., and Ito., E. (1992) Isothermal compression curve of $MgSiO_3$ tetragonal garnet. Physics of the Earth and Planetary Interiors, 74, 1–7.

Yamakazi, D., Ito, E., Yoshino, T., Yoneda, A., Guo, X., Zhang, B., Sun, W., Shimojuki, A., Tsujino, N., Kunimoto, T., Higo, Y., and Funakoshi, K-i. (2012) *P-V-T* equation of state for ε-iron up to 80 GPa and 1900 K using the Kawai-type high pressure apparatus equipped with sintered diamond anvils. Geophysical Research Letters, 39, L20308.

Yamakazi, D., Ito, E., Yoshino, T., Tsujino, N., Yoneda, A., Guo, X., Xu, F., Higo, Y., and Funakoshi, K. (2014) Over 1 Mbar generation in the Kawai-type multianvil apparatus and its application to compression of $(Mg_{0.92}Fe_{0.08})SiO_3$ perovskite and stishovite. Physics of the Earth and Planetary Interiors, 228, 262-267.

Zeng, Z.-Y., Hui, C.-E, Cai, L.-C., and Jing, F.-Q. (2012) *Ab initio* study of lattice dynamics and thermal equation of state of Ni. Physica B, 407, 330–334.

Zhang, F., and Wright, K. (2010) Coupled (H^+, M^{3+}) substitutions in forsterite. Geochimica et Cosmochimica Acta, 74, 5958–5965.

Zhang, F., and Wright, K. (2012) Coupled (Li^+, Al^{3+}) substitutions in hydrous forsterite. American Mineralogist, 97, 425–429.

Zou, Y., Irifune, T., Gréaux, S., Whitaker, M.L., Shinmei, T., Ohfuji, H., Negishi, R., and Higo, Y. (2012) Elasticity and sound velocities of polycrystalline $Mg_3Al_2(SiO_4)_3$ garnet up to 20 GPa and 1700 K. Journal of Applied Physics, 112, 0149.

Appendix A: Tables

Table 1. High-pressure Pt and PtC volume data from this study. The uncertainties are in parentheses. The diffraction peaks used to calculate the volumes are listed. The volumes reported are the average from the peaks listed with the uncertainty being the standard deviation. The pressures are from the Pt equation of state (Fei et al. 2004). When there was not a measured zero-pressure volume, the average of all of the measured values was used and denoted by *a* with the standard deviation as the uncertainty.

Pt V_0 (Å^3)	Pt V (Å^3)	P (GPa)	Pt Peaks	PtC V_0 (Å^3)	PtC V (Å^3)	PtC Peaks
59.9(4)	58.0(2)	10(2)	(111) (200) (220) (222)	109.3(6)[a]	104.3(1)	(111)
60.2(4)	54.7(1)	33(3)	(111) (200) (220)	109.6(4)	102.90(6)	(200) (220)
58.34(0)	51.24(0)	48(3)	(111)	108.57(4)	93.87(2)	(111)
59.7(8)[a]	57.6(9)	15(5)	(111) (200)	109.3(6)[a]	107.57(4)	(111)
59.7(8)[a]	57(1)	13(5)	(111) (200) (220) (222)	109.3(6)[a]	105.8(6)	(111) (311)
59.7(8)[a]	57.1(1)	13(5)	(111) (200)	109.3(6)[a]	104.76(4)	(111)

Table 2. PtC equation of state parameters. K_0 is the zero-pressure, 300 K bulk modulus, and K_0' is its pressure derivative. "Combined" refers to the results of fitting the data from this study and the study of Ono et al. (2005) to the 3rd-order Birch-Murnaghan equation of state. The results from using 2 different Pt equations of state are shown. Uncertainties are in parentheses.

	K_0 (GPa)	K_0'
Holmes et al. (1989) Pt EOS		
Ono et al. (2005)	298(3)	5.55(9)
Combined	222(3)	5.9(1)
Fei et al. (2004) Pt EOS		
Ono et al. (2005)	310(20)	4.4(8)
Combined	280(20)	5.3(7)

Table 3. MGD and HTBM thermal equation of state parameters for nickel and stishovite.

Nickel					
	This Study				*Campbell et al.* [2009]
P standard	MgO[a]		SiO_2[b]		NaCl[c,d]
P max, GPa	109(5)		49(1)		66(3)
T max, K	2900(500)		2440(80)		2460(70)
V_0, cm^3/mol	**6.579(1)**		6.579(1)		6.587[e]
K_0, GPa	**201(6)**		200(2)		179(3)
K_0'	**4.4(3)**		4.4[f]		4.3(2)
θ_0, K	**415**[g]		415[g]		415[g]
γ_0	**1.98(8)**	1.90(3)	2.04(4)		2.50(6)
q	**1.3(2)**	1[f]	1[f]		1[f]
$(\partial K_{0,T}/\partial T)_P$, GPa/K	–0.026(2)		–0.063(2)		–
α_0, 10^{-5} K^{-1}	2.7(2)		0.9(4)		–
α_1, 10^{-8} K^{-2}	0.9(2)		6.6(7)		–

Stishovite						
	This Study					*Wang et al.* [2012]
P standard	MgO[a]		Ni[h]			Au[i]
P max, GPa	47(1)		52(1)			54.5(3)
T max, K	2440(80)		2440(80)			1700
a_0	*4.172(2)*		–			–
c_0	2.667(1)		–			–
V_0, cm^3/mol	**13.97**[j]		13.97[j]			14.02
K_0, GPa	**312.9**[j]		312.9[j]			294(2)
K_0'	**4.8**[j]		4.8[j]			4.85(12)
K_{0a} GPa	*284(5)*		–			–
K_{0a}'	*4*[f]		–			–
K_{0c} GPa	450(20)		–			–
K_{0c}'	4[f]		–			–
θ_0, K	***1109***[k]		1109[k]			1130(100)
γ_0	1.36(2)	***1.55*(1)**	1.66(7)	1.44(2)	1.65(3)	1.66(7)
q	1[f]	***2.9***[b]	2.9(4)	1[f]	2.9[b]	2.9(4)
$(\partial K_{0,T}/\partial T)_P$, GPa/K	–0.058(1)		–0.044(5)			–
$(\partial K_{0a,T}/\partial T)_P$, GPa/K	–0.050(3)		–			–
$(\partial K_{0c,T}/\partial T)_P$, GPa/K	–0.091(7)		–			–
α_0, 10^{-5} K^{-1}	1.94(8)		1.5(2)			–
α_{0a}, 10^{-5} K^{-1}	0.69(6)		–			–
α_{0c}, 10^{-5} K^{-1}	0.3(1)		–			–
α_1, 10^{-8} K^{-2}	1.2(1)		1.2(3)			–
α_{1a}, 10^{-8} K^{-2}	0.45(8)		–			–
α_{1c}, 10^{-8} K^{-2}	0.6(1)		–			–

Bold values were used to calculate the isotherms in Fig. 13 and the densities in Fig. 18.
Italic values were used to calculate the isotherms in Fig. 15.
[a]Speziale et al. (2001); [b]Wang et al. (2012); [c]Decker (1971); [d]Fei et al. (2007); [e]JCPDS card files; [f]Assumed; [g]Knacke et al. (1991); [h]Campbell et al. (2009); [i]Tsuchiya (2003), [j]Panero et al. (2003); [k]Akaogi et al. (2011)

Table 4. Grid showing the cation-oxygen bonding in the majorite structure.

Atom	Mg1 (VIII)	Mg2 (VIII)	Mg3 (VII)	Si1 (IV)	Si2 (IV)	Si3 (IV)	Si4 (VI)
O1	**X**	**XX**	**XX**			**X**	
O2	**X**	**XX**				**X**	**XX**
O3	**X X**					**X**	**XX**
O4	**X X**		**XX**			**X**	
O5	**X**	**XX**	**XX**	**XXXX**			
O6	**X**	**XX**			**XXXX**		**XX**

Table 5. Interatomic potential parameters and ionic charges.

Species	q (e)
Mg(core)	1.7
Si(core)	3.4
Al(core)	2.55
O(core)	0.746527
O(shell)	–2.446527
O_H(core)[a]	–1.2
H(core)	0.35

Interaction			
Buckingham	A (eV)	ρ (Å)	C (eV · Å^6)
Mg(core) – O (shell)	1432.8544	0.277265	0.0
Si(core) – O (shell)	1073.4668	0.298398	0.0
Al(core) – O (shell)	1262.2081	0.28637	0.0
Mg(core) – O_H(core)	1015.8587	0.277265	0.0
Si(core) – O_H(core)	761.06168	0.298398	0.0
Al(core) – O_H(core)	894.87465	0.28637	0.0
O(shell) – O(shell)	598.8996	0.314947	26.89746
O(shell) – O_H(core)	598.8996	0.314947	26.89746
O_H (core) – O_H(core)	598.8996	0.314947	26.89746
H(core) – O(shell)	191.6667	0.25	0.0
H(core) – O_H(core)	191.6667	0.25	0.0

Morse	D_e (eV)	a (Å^{-1})	r_0 (Å)
H(core) – O_H(core)	7.0525	2.1986	0.94285

Spring	k_2 (eV/Å^2)	k_4 (eV/Å^4)
O(core) – O(shell)	56.5598	10000.0

Three-body	k_θ (eV/rad^2)	θ (degrees)
O – ^{IV}Si – O	0.77664	109.47
O – ^{VI}Si – O	2.2955	90.0
O – ^{IV}Al – O	1.2883	109.47
O – ^{VI}Al – O	1.8807	90.0

[a]Hydroxyl oxygen.

Table 6. Optimized atomic coordinates for tetragonal $MgSiO_3$ majorite at 0 GPa compared to published experimental and computational data. The static lattice energy calculation (SLEC) results were both obtained using essentially the same potential models, except for changes to the truncation of the Buckingham potentials and the inclusion of a fourth-order spring constant in the shell model. The density functional theory (DFT) calculations were performed within the generalized gradient approximation (GGA) using VASP (this study) and CASTEP (Vinograd et al. 2006). Atoms at special positions (Mg3, Si1, S2, and Si4) are omitted from the comparison. The crystallographic origin has been shifted by 0.5, 0.0, 0.0 relative to the standard origin for space group no. 88 ($I4_1/a$). The x-ray diffraction (XRD) data were collected at ambient conditions and the uncertainties are in parentheses.

Atomic coordinates			*XRD*[a]	*SLEC* This Study	*SLEC*[b]	*DFT-GGA* This Study	*DFT-GGA*[b]
Atom	*Site*						
Mg1	D1	x	0.1253(4)	0.1261	0.1256	0.1288	0.1287
		y	0.0112(4)	0.0129	0.0120	0.0134	0.0135
		z	0.2857(3)	0.2645	0.2623	0.2663	0.2665
Mg2	D2	x	0.0000	0.0000	0.0000	0.0000	0.0000
		y	0.2500	0.2500	0.2500	0.2500	0.2500
		z	0.6258(6)	0.6229	0.6227	0.6234	0.6235
Si3	T3	x	0.1249(3)	0.1260	0.1261	0.1256	0.1254
		y	0.0065(3)	0.0115	0.0116	0.0107	0.0116
		z	0.7544(3)	0.7564	0.7560	0.7568	0.7568
O1	O(1)	x	0.0282(6)	0.0267	0.0257	0.0260	0.0268
		y	0.0550(6)	0.0591	0.0603	0.0580	0.0588
		z	0.6633(6)	0.6693	0.6685	0.6691	0.6691
O2	O(2)	x	0.0380(6)	0.0433	0.0429	0.0451	0.0447
		y	0.9529(6)	0.9559	0.9540	0.9550	0.9565
		z	0.8562(6)	0.8612	0.8610	0.8616	0.8611
O3	O(3)	x	0.2195(7)	0.2243	0.2248	0.2244	0.2234
		y	0.1023(6)	0.1075	0.1079	0.1060	0.1069
		z	0.8021(6)	0.8050	0.8070	0.8061	0.8053
O4	O(4)	x	0.2150(6)	0.2133	0.2145	0.2128	0.2117
		y	0.9106(6)	0.9166	0.9161	0.9154	0.9165
		z	0.7000(6)	0.7024	0.7013	0.7026	0.7028
O5	O(5)	x	0.9412(6)	0.9358	0.9353	0.9363	0.9372
		y	0.1617(6)	0.1639	0.1629	0.1641	0.1638
		z	0.4680(6)	0.4682	0.4690	0.4688	0.4678
O6	O(6)	x	0.8960(6)	0.8978	0.8980	0.8974	0.8977
		y	0.2080(6)	0.2128	0.2102	0.2149	0.2153
		z	0.7851(6)	0.7829	0.7821	0.7830	0.7833

[a]Angel et al. (1989); [b]Vinograd et al. (2006)

Table 7. Calculated structural parameters for tetragonal $MgSiO_3$ majorite compared to published experimental and computational data.

Cell parameters	*XRD*[a]	*SLEC* This Study	% difference	*SLEC*[b]	*DFT-GGA* This Study	*DFT-GGA*[b]
			P = 0 GPa			
a (Å)	11.501(1)	11.506	0.04	11.494	11.638	11.670
c (Å)	11.480(2)	11.416	–0.56	11.392	11.528	11.561
c/*a*	0.9982(2)	0.9922	–0.60	0.9912	0.9905	0.9907
V(Å^3)	1518.6(4)	1511.27	–0.48	1505.04	1561.34	1574.47
			P = 10 GPa			
a (Å)	11.315	11.307	–0.07	–	–	–
c (Å)	11.214	11.211	–0.03	–	–	–
c/*a*	0.9911	0.9915	0.04	–	–	–
V(Å^3)	1435.7	1433.33	–0.17	–	–	–
			P = 20 GPa			
a (Å)	–	11.144	–	–	11.251	–
c (Å)	–	11.048	–	–	11.115	–
c/*a*	–	0.9913	–	–	0.9879	–
V(Å^3)	–	1372.05	–	–	1407.06	–

[a]Ambient condition (Angel et al. 1989) and *P* = 9.72 GPa experiments (Yagi et al. 1992) and ; [b]CASTEP (Vinograd et al. 2006)

Table 8. Elastic constants, bulk (K_S) and shear (μ) moduli of tetragonal majorite garnet ($MgSiO_3$).

Elastic constants	*Experimental* (GPa)	*SLEC* This study (GPa)	*SLEC*[b] (GPa)
	P = 0 GPa		
C_{11}	[a]286.4(13)	296.52	295.10
C_{33}	[a]280.1(18)	296.14	–
C_{44}	[a]85.0(7)	86.05	85.23
C_{66}	[a]93.2(11)	94.14	93.66
C_{12}	[a]83.0(29)	112.5	112.7
C_{23}	[a]104.9(24)	102.42	–
C_{16}	[a]1.4(13)	14.30	14.72
	P = 10 GPa		
C_{11}	–	347.04	–
C_{33}	–	350.51	–
C_{44}	–	92.99	–
C_{66}	–	103.66	–
C_{12}	–	141.27	–
C_{23}	–	132.47	–
C_{16}	–	21.55	–
	P = 20 GPa		
C_{11}	–	392.16	–
C_{33}	–	398.69	–
C_{44}	–	97.96	–
C_{66}	–	109.86	–
C_{12}	–	170.97	–
C_{23}	–	164.06	–
C_{16}	–	26.36	–
Isotropic properties			
	P = 0 GPa		
K_S	[a]159.8(44), [c]167.3(33) [d]164.4(5), [e]170(5), [f]166(3) [g]166(5), [h]164(4)	169.3	170.14
μ	[a]89.7(6), [c]88.3(18), [d]94.9(2) [e]89(1), [f]85(2), [g]88(2), [h]87(2)	90.8	–
	P = 10 GPa		
K_S	[b]210(4)	206.3	–
μ	[b]103(2)	99.4	–
	P = 20 GPa		
K_S	–	242.4	–
μ	–	105.3	–

[a]Ambient condition experiments, Mj_{100} (Pacalo and Weidner 1997); [b]Vinograd et al. (2006); [c]Mj_{100} (Gwamnesia et al. 1998); [d]pyrolite minus olivine composition (Irifune et al. 2008); [e]$Mj_{50}Py_{50}$ (Liu et al. 2000); [f]Mj_{100} (Sinogeikin and Bass 2002); [g]Mj_{100} (Sinogeikin et al. 1997a); [h]natural Catherwood meteorite sample (Sinogeikin et al. 1997b)

Table 9. Structure and bulk modulus of mineral phases in the Mg-Si-Al-O-H system using force fields compared to experimental results. The experimental structural results are from ambient conditions with the exception of the kaolinite data that were acquired at *T* = 1.5 K. The reported experimental uncertainties are in parentheses. The experimental lattice parameters of superhydrous B are based on the average of the measurements reported by Litasov et al. (2007), weighted according to the uncertainties. The experimental bulk moduli values are either Hill-averages of ambient condition elasticity measurements or are from Birch-Murnaghan equation of state measurements where $K_0' = 4$.

Phase		*a* (Å)	*b* (Å)	*c* (Å)	*V* (Å^3)	*α* (°)	*β* (°)	*γ* (°)	K_0 (GPa)
Pyrope	Calc.	11.462	-	-	1505.69	90.0	-	-	174.1
	Exp.[a,b]	11.4482(2)	-	-	1500.43(8)	90.0	-	-	171.2(20)
MgO	Calc.	4.205	-	-	74.33	90.0	-	-	192.9
	Exp.[c,b]	4.215(1)	-	-	74.698(3)	90.0	-	-	163.2(10)
Brucite	Calc.	3.129	-	4.823	40.88	90.0	-	120.0	35.1
	Exp.[d]	3.14(1)	-	4.76(1)	40.8(1)	90.0	-	120.0	46(1)
Quartz	Calc.	4.994	-	5.498	118.77	90.0	-	120.0	45.5
	Exp.[e,f]	4.91300(11)	-	5.40482(17)	112.981(2)	90.0	-	120.0	40.4(33)
Coesite	Calc.	7.138	12.389	7.194	547.45	90.0	120.62	90.0	115.5
	Exp.[g,h]	7.1366(2)	12.3723(4)	7.1749(3)	546.80(3)	90.0	120.33	90.0	113.7(-)
Stishovite	Calc.	4.135	-	2.722	46.54	90.0	-	-	337.5
	Exp.[i,j]	4.17755(16)	-	2.66518(34)	46.5126(61)	90.0	-	-	305(5)
Lizardite	Calc.	5.326	-	7.191	176.67	90.0	-	120.0	56.8
	Exp.[k]	5.335(5)	-	7.243(5)	178.4(5)	90.0	-	120.0	57.0(-)
Superhydrous B	Calc.	5.090	13.966	8.695	618.16	90.0	-	-	157.7
	Exp.[l,m]	5.105	14.006	8.718	623.38(39)	90.0	-	-	154.0(42)
Kaolinite	Calc.	5.194	9.076	7.401	337.95	90.04	104.35	88.99	53.2
	Exp.[n,o]	5.1535(3)	8.9419(5)	7.3906(4)	328.70(5)	91.93	104.86	89.80	47.9(8)
Corundum	Calc.	4.786	-	13.056	259.03	90.0	-	120.0	277.7
	Exp[p]	4.7617(9)	-	12.9947(17)	255.05(7)	90.0	-	120.0	257(6)

[a]Zou et al. (2012); [b]Sinogeiken and Bass (2000); [c]Jacobsen et al. (2002); [d]Xia et al. (1998); [e]Angel et al. (1997); [f]Bass et al. (1981); [g]Angel et al. (2001); [h]Weidner and Carleton (1977); [i]Andrault et al. (2003); [j]Li et al. (1996); [k]Mellini and Zanazzi. (1989); [l]Litasov et al. (2007); [m]Pacalo and Weidner (1996); [n]Bish (1993); [o]Wang et al. (2001); [p]Finger and Hazen (1978)

Table 10. Calculated vacancy formation energy and crystalline lattice energies from force fields.

Defect	*Formation Enthalpy (eV)*	
Unbound vacancies	0 GPa	25 GPa
$\square_{Mg1}^{''}$	18.89	19.50
$\square_{Mg2}^{''}$	18.77	19.38
$\square_{Mg3}^{''}$	19.43	20.26
$\square_{Si1}^{''''}$	76.61	78.89
$\square_{Si2}^{''''}$	70.07	71.95
$\square_{Si3}^{''''}$	73.39	75.84
$\square_{Si4}^{''''}$	72.56	74.36
$\square_{O1}^{\cdot\cdot}$	17.06	16.78
$\square_{O2}^{\cdot\cdot}$	16.69	16.92
$\square_{O3}^{\cdot\cdot}$	15.93	15.56
$\square_{O4}^{\cdot\cdot}$	15.96	15.54
$\square_{O5}^{\cdot\cdot}$	15.95	15.56
$\square_{O6}^{\cdot\cdot}$	17.08	17.31
Bound vacancies		
$[\square_{Mg1} + \square_{O1}]^{x}$	35.86	36.34
$[\square_{Mg1} + \square_{O2}]^{x}$	35.44	36.32
$[\square_{Mg1} + \square_{O3}]^{x}$	34.97	34.99
$[\square_{Mg1} + \square_{O4}]^{x}$	35.87	35.03
$[\square_{Mg1} + \square_{O5}]^{x}$	34.90	35.01
$[\square_{Mg1} + \square_{O6}]^{x}$	36.15	37.07
$[\square_{Mg2} + \square_{O1}]^{x}$	35.20	35.24
$[\square_{Mg2} + \square_{O2}]^{x}$	35.04	35.24
$[\square_{Mg2} + \square_{O5}]^{x}$	34.66	34.68
$[\square_{Mg2} + \square_{O6}]^{x}$	35.47	36.59
$[\square_{Mg3} + \square_{O1}]^{x}$	35.69	35.88
$[\square_{Mg3} + \square_{O4}]^{x}$	36.40	34.81
$[\square_{Mg3} + \square_{O5}]^{x}$	34.67	35.04
Phase		
MgO	–30.18	–27.44
α-Quartz	–95.35	–
Stishovite	–	–91.06

Table 11. Enthalpies of the hydrogarnet defect calculated from first principles at the DFT-GGA level of theory.

	0 GPa	20 GPa
Enthalpy (eV)		
MgO[a]	–12.01	–9.71
SiO_2, α-quartz[a]	-23.98	–
SiO_2, stishovite[a]	–	-20.55
Majorite[b]	–1147.67	–963.27
Defect Formation Enthalpy (eV/H)		
$\square_{Mg3}^{''} + 2(OH_{O5}^{\cdot})$	–0.51	–0.62
$\square_{Si2}^{''''} + 4(OH_{O6}^{\cdot})$	–1.37	–1.16
Reaction enthalpy (eV/H)		
Reaction 6	–0.85	–0.82

[a]1 formula unit; [b]Full unit cell (8 formula units)

Appendix B: Figures

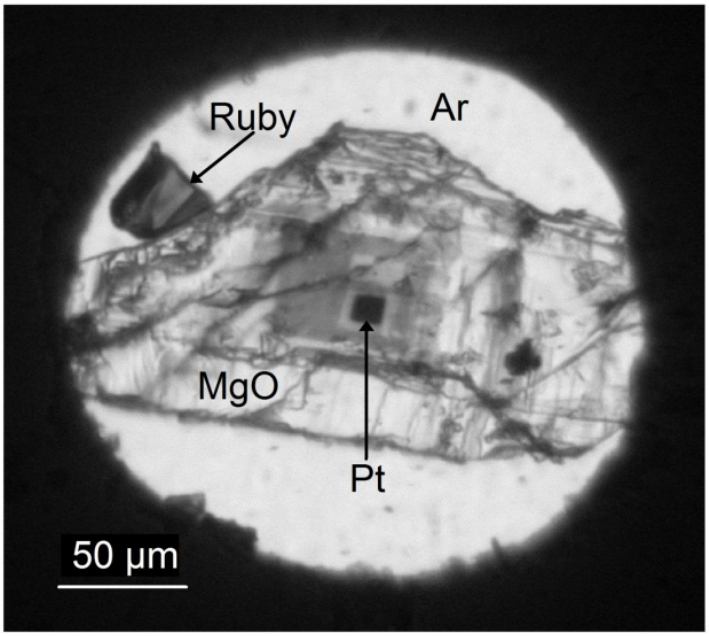

Figure 1. Controlled geometry Pt sample embedded in a MgO single crystal and compressed in a DAC. The sample is compressed to 5.2 GPa before laser heating.

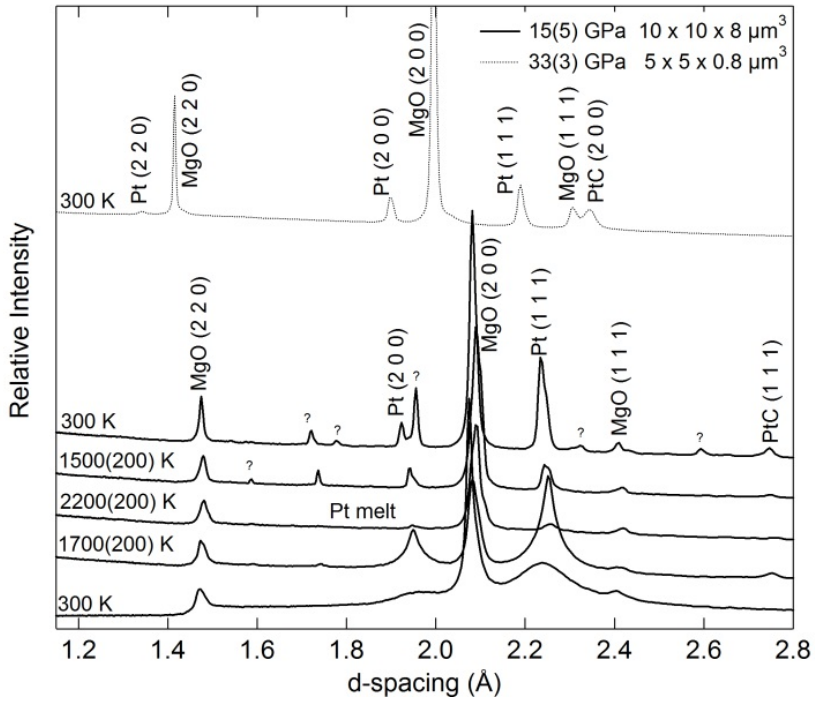

Figure 2. X-ray diffraction spectra from an 8-μm- and 0.8-μm-thick Pt layer embedded in a 33-μm- and 21-μm-thick MgO single crystal, respectively. Ruby served as a pressure standard and powdered MgO (15 GPa) or Ar (33 GPa) was used as an insulation medium. PtC formed as a secondary phase resulting from the Pt deposition. Unidentified peaks are labeled with question marks.

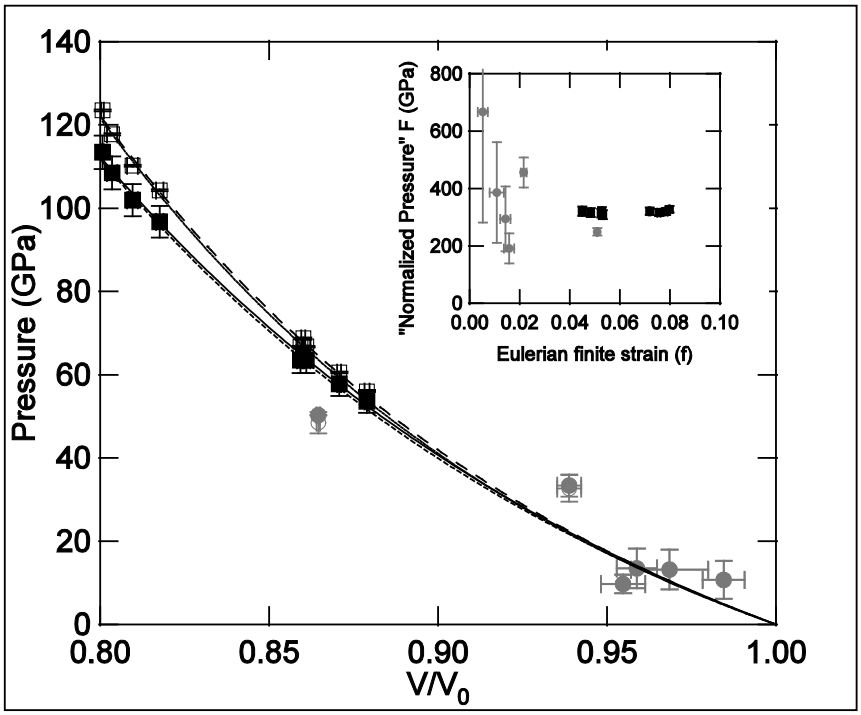

Figure 3. PtC compression. Black squares are from Ono et al. (2005) and gray circles are from this study. Pt served as the internal pressure standard. Open symbols are based on pressures calculated from the Holmes et al. (1989) equation of state with an electronic thermal pressure correction (Tsuchiya and Kawamura 2002)) and filled symbols are based on pressures calculated from the Fei et al. (2004) equation of state. The curves are from curve-fitting to the 3rd-order Birch-Murnaghan equation of state. The error bars represent the uncertainties after full error propagation.

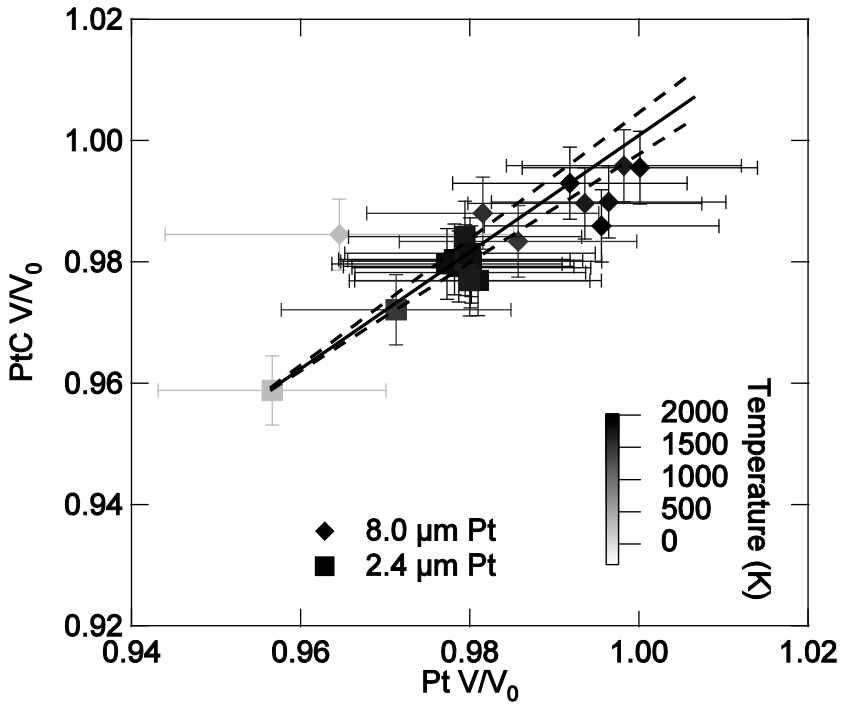

Figure 4. Normalized unit-cell volumes of PtC and Pt from two samples. The solid line is the predicted volume change based on the relative thermal expansions from equation 2.3. The dashed lines represent the uncertainty in the relative thermal expansions. The error bars represent the uncertainty after full error propagation.

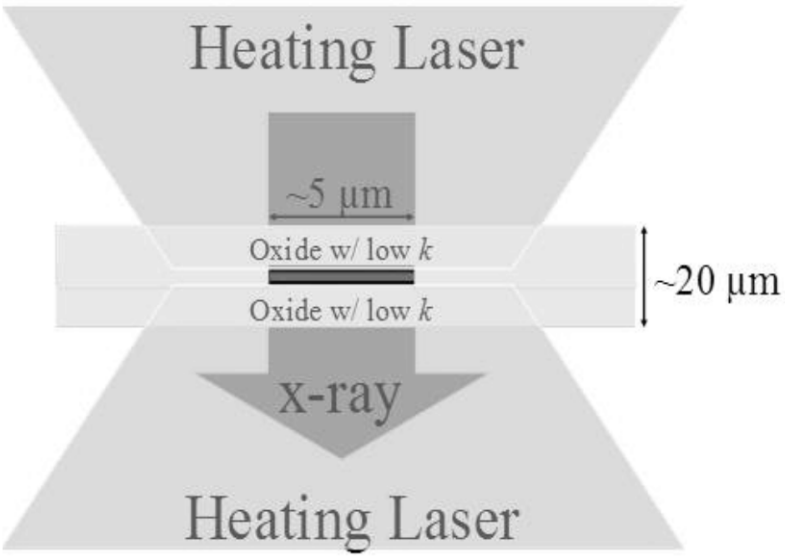

Figure 5. Schematic of controlled geometry sample showing its relative size compared to the x-ray beam and heating lasers. The dark gray sample of interest is between the black metal laser absorbers. Note that the entire sample will be heated and completely sampled by the x-ray beam.

Figure 6. (a) Schematic DAC cross section showing the sample, heating lasers (yellow) and x-ray (orange). (b) Scanning electron microscope (SEM) image of an array of the samples. (c) Backscattered electron image of a recovered sample before loading in the diamond-anvil cell. (d) A sample, compressed to P = 66(1) GPa, and viewed through the cylinder diamond after heating to T = 2360(100) K. The insulation and pressure medium is MgO and the gasketing material is rhenium.

(a)

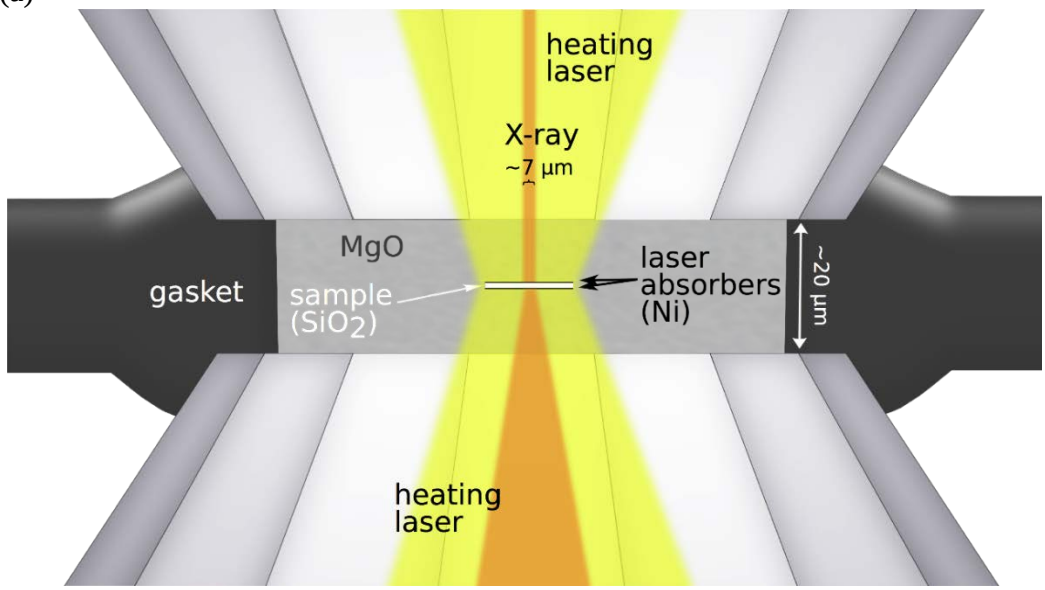

(b)

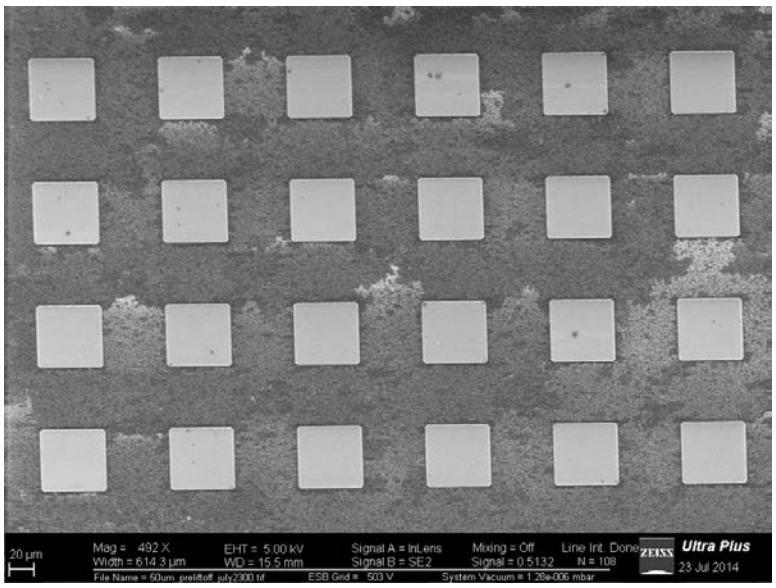

(continued)

(Figure 6 continued)

(c)

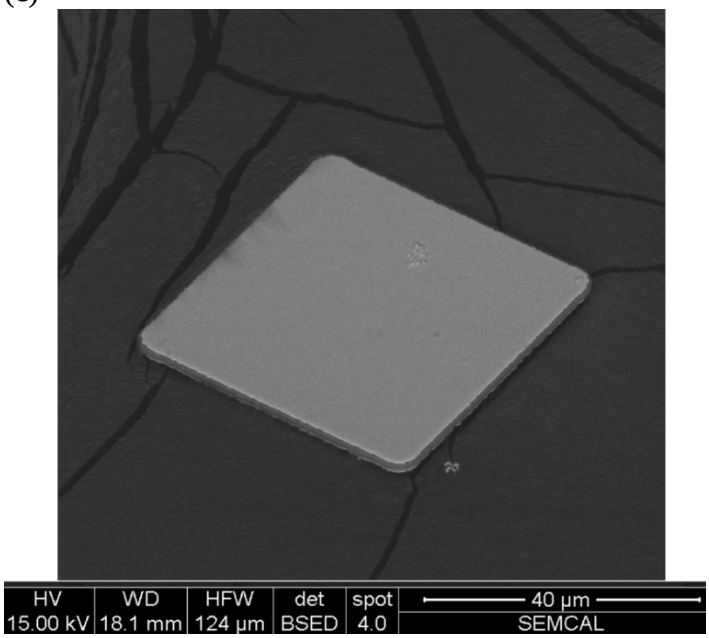

(d)

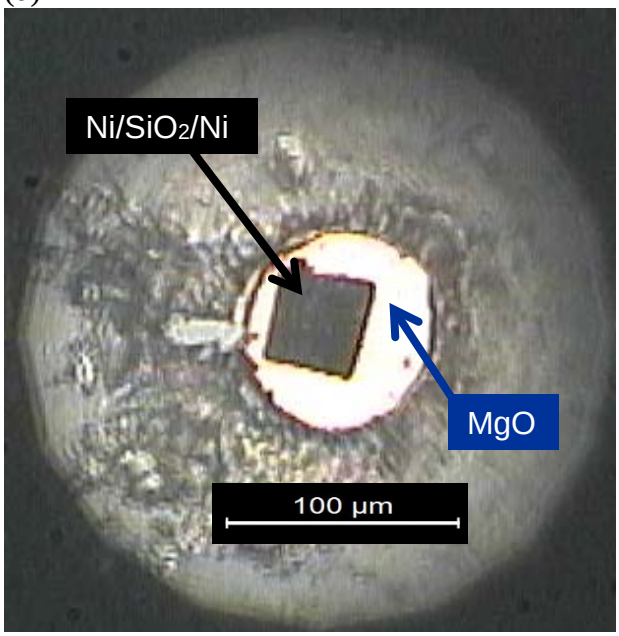

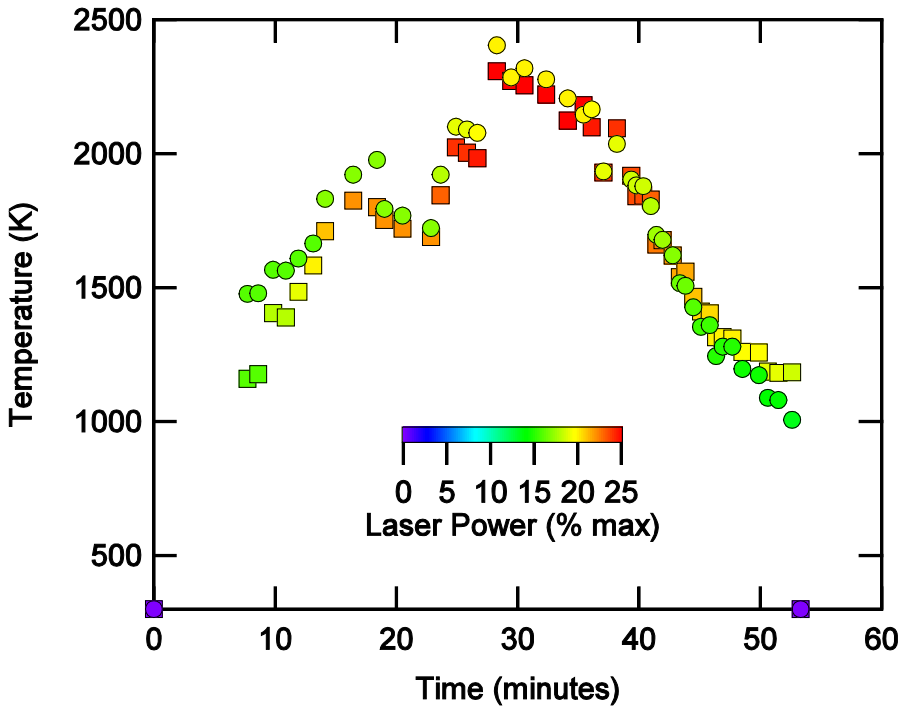

Figure 7. Temperature as a function of time and laser power for a laser-heating cycle at ~65 GPa. Temperature measured from both the downstream (squares) and upstream (circles) sides are shown.

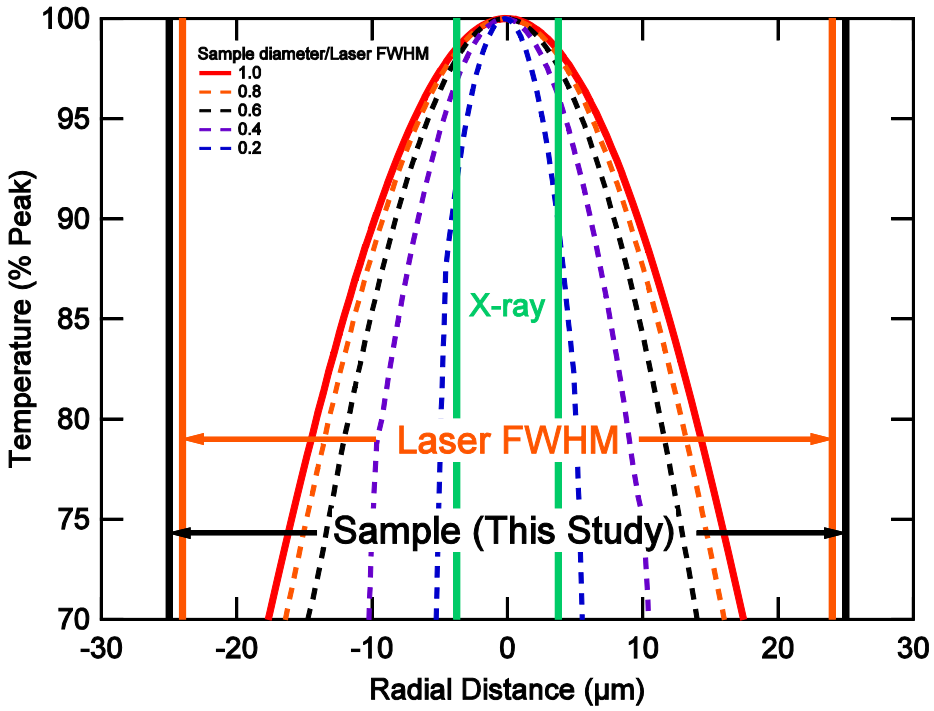

Figure 8. Radial temperature distributions for different ratios of laser absorbing sample diameter to FWHM of a Gaussian laser calculated using TempDAC (Rainey et al. 2013). The absolute peak temperature is 2600 – 2700 K. X-ray spot size is 16% of the laser FWHM; and a sample chamber diameter 1.9 times laser FWHM. The sample consists of a perfectly absorbing Pt layer that is 4.0 μm thick and surrounded by MgO. The radial temperature gradients within the volume probed by the x-ray are reduced when the sample width to laser FWHM ratio is >0.7. The temperature range in the x-ray probed region is 98.4 – 100% of the measured peak temperature for a sample to laser ratio that is >1.0, as in the present study. This temperature range does not include the portion of the sample probed by the x-ray beam tails which were insignificant during our experiments.

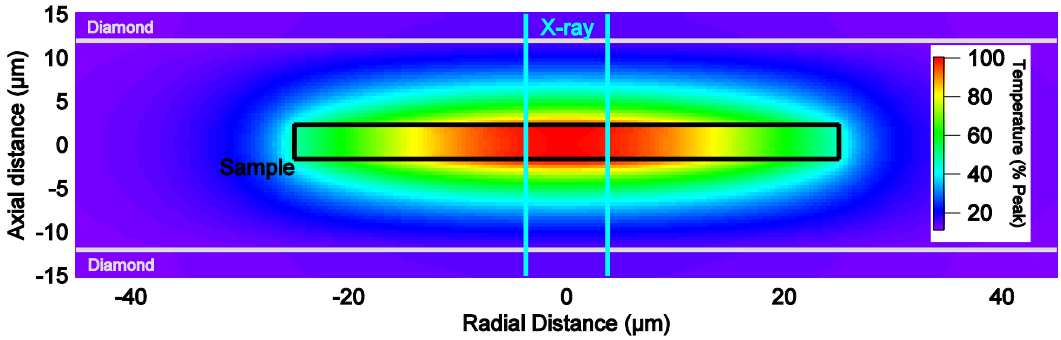

Figure 9. Modeled axial and radial temperature distribution in the LHDAC. The temperatures were calculated using the 3-D numerical modeling code TempDAC (Rainey et al. 2013). The spatial parameters of the calculation are: absolute peak temperature = 2600 K, x-ray spot size = 7.5 µm wide, double-sided heating is via a Gaussian laser (TEM_{00}) with FWHM = 48 µm. The sample chamber is 24 µm thick with a diameter of 90 µm. The sample consists of a perfectly absorbing 4.0 µm thick Pt layer (k_0 = 77.8 W/m K) (Terada et al. 2005) with a diameter of 50 µm surrounded by MgO (k_0 = 62.5 W/m K) (Tang and Dong 2010). The temperature within the 4.0 µm thick Pt layer varies between 99.3–100% of the peak temperature at r = 0 and between 97.8–100% of the peak temperature within the Pt probed by the x-ray.

(a)

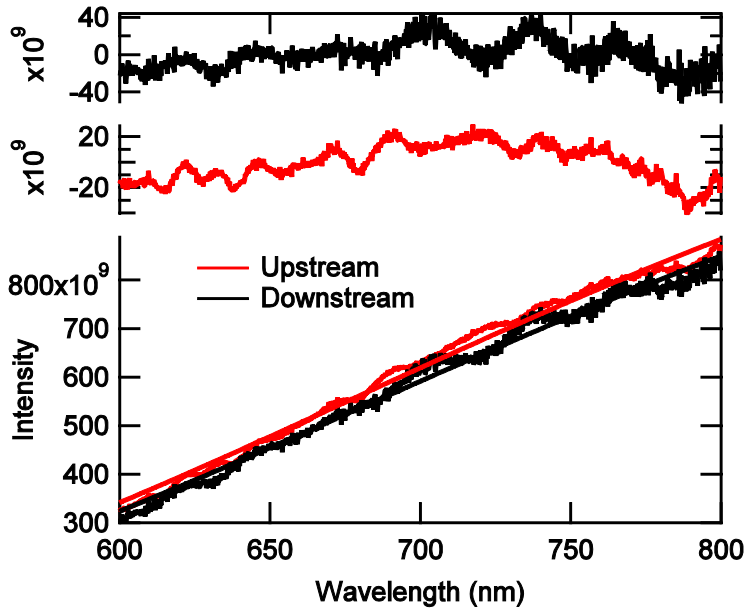

(b)

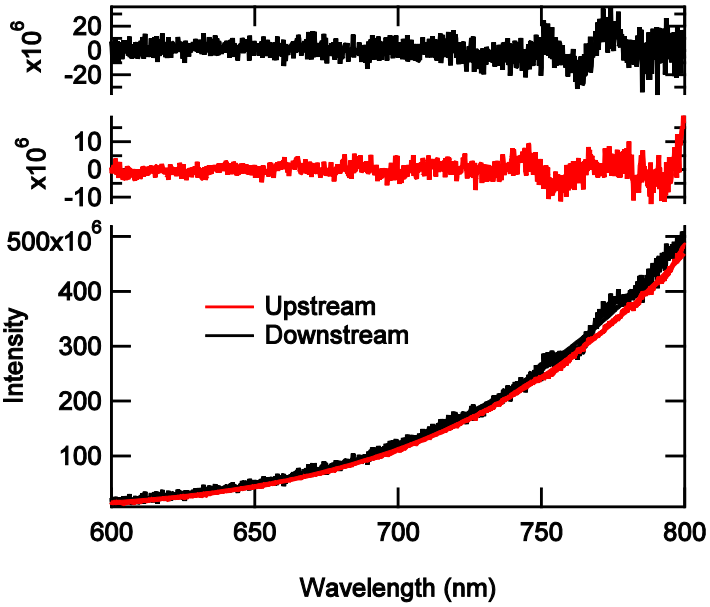

Figure 10. Representative temperature measurements from our Ni/SiO_2/Ni samples showing the accuracy of the Planck's law fits assuming constant emissivity. The temperatures from the fits are (a) upstream T = 2511(3) K, downstream T = 2497(4) K and (b) upstream T = 1223(1) K, downstream T = 1228(2) K. The fit residuals are shown above the spectral intensity.

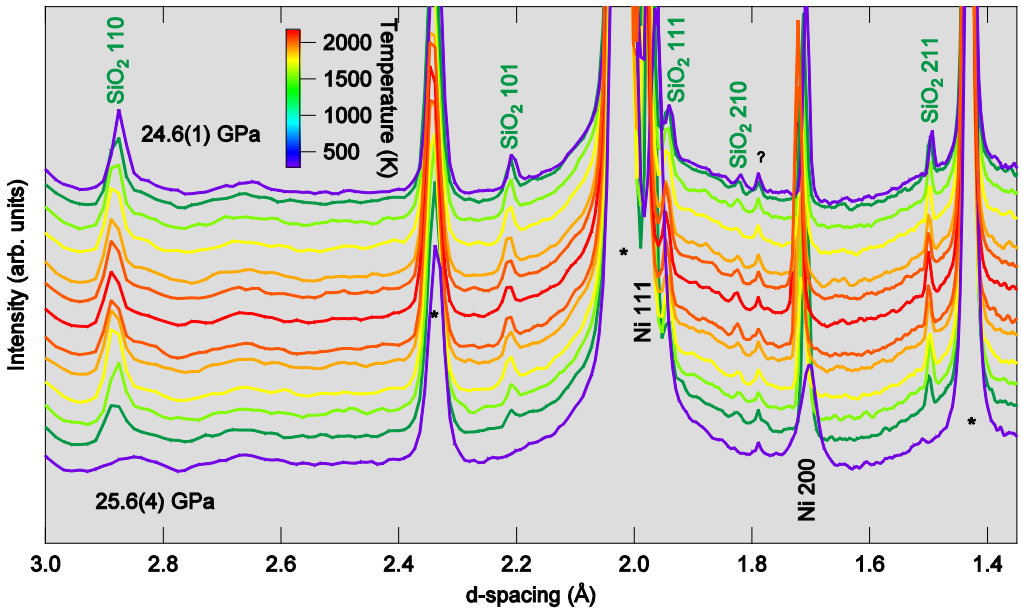

Figure 11. Representative x-ray diffraction patterns of a nanofabricated Ni/SiO_2/Ni sample at high *P*-*T* conditions. The patterns are from a single heating cycle starting at 25.6(4) GPa and are offset vertically for clarity in order from bottom to top. The '*' denotes diffraction from the MgO insulation and pressure-transmitting medium. There is one unidentified spurious peak labeled with a question mark. This peak does not appear during other heating cycles and does not shift systematically with temperature therefore we conclude that it does not come from our sample.

Figure 12. (a) High-angle annular dark-field (HAADF) image of sample recovered from P = 24.6(1) GPa after laser heating to T_{max} = 2170(100) K. (b) Mg (c) Ni (d) O (e) Si EDS maps from the highlighted box in the HAADF image. The images and analyses were acquired using an FEI Tecnai F20 scanning transmission electron microscope. An FEI Helios 600 dual-beam focused-ion beam (FIB) with a Ga^+ liquid-metal ion source was used to extract and thin the vertical slice of the recovered run-product.

(a)

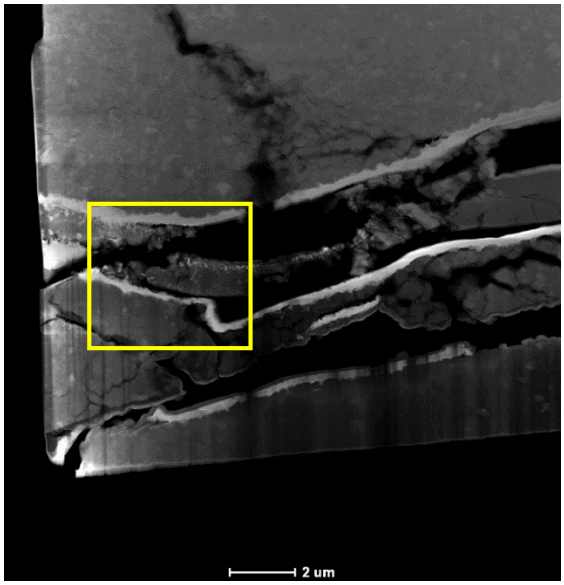

(b)

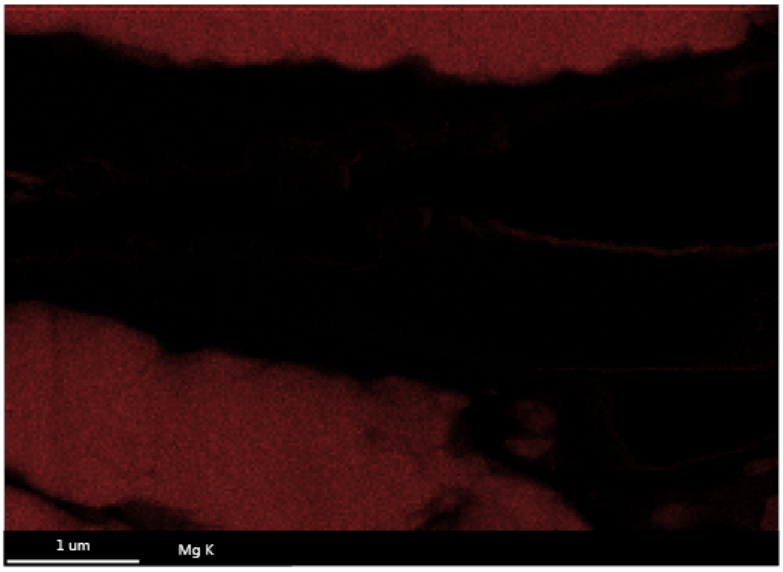

(continued)

(Figure 12 continued)

(c)

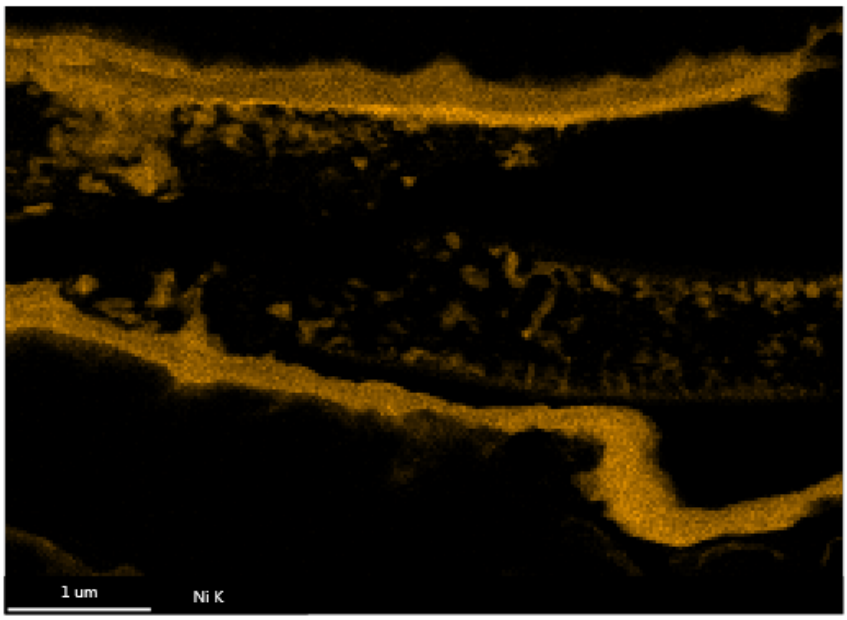

(d)

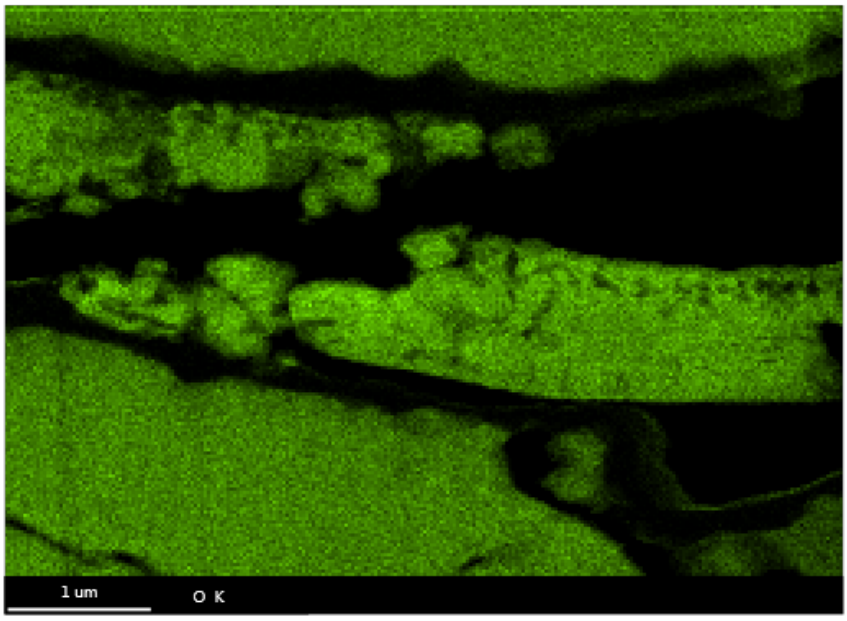

(continued)

(Figure 12 continued)

(e)

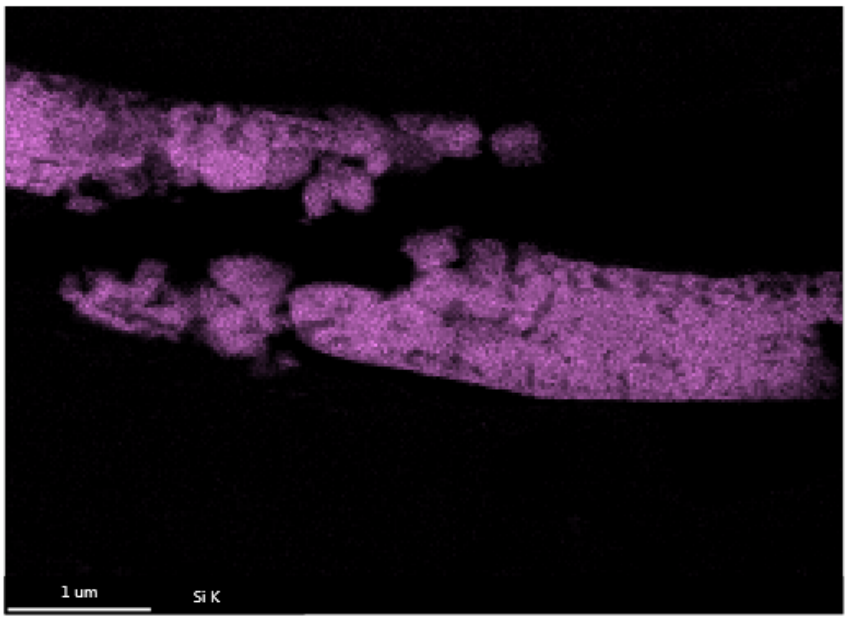

(a.)

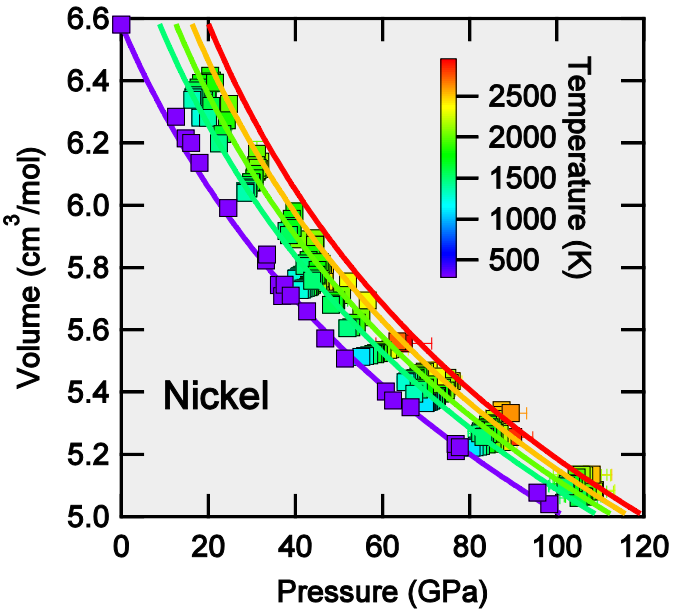

(b.)

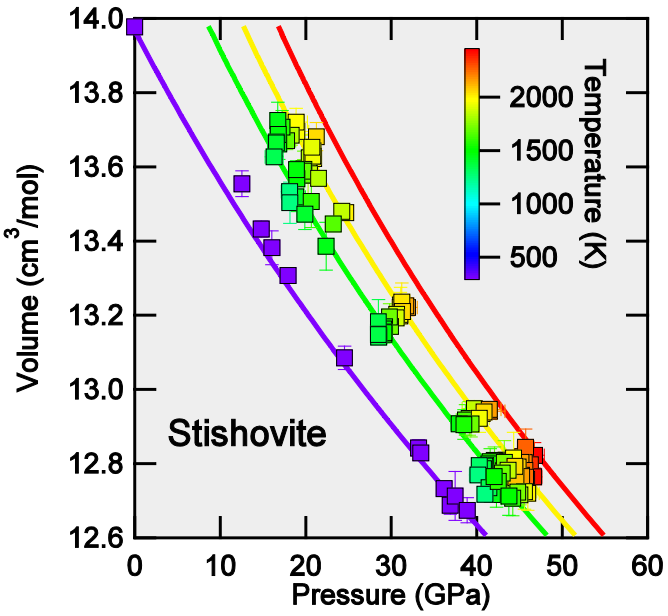

Figure 13. Experimental *P-V-T* data for (a.) nickel and (b.) stishovite with calculated isotherms based on parameters (Table 3) obtained from the fit to data. The MgO insulation was used as the pressure standard according to the thermal equation of state of Speziale et al. (2001). The temperature of the MgO was assumed to be the average temperature of the x-rayed volume (Campbell et al. 2009). Uncertainties in the pressure and volume are shown and are smaller than the size of the symbol when not visible.

(a)

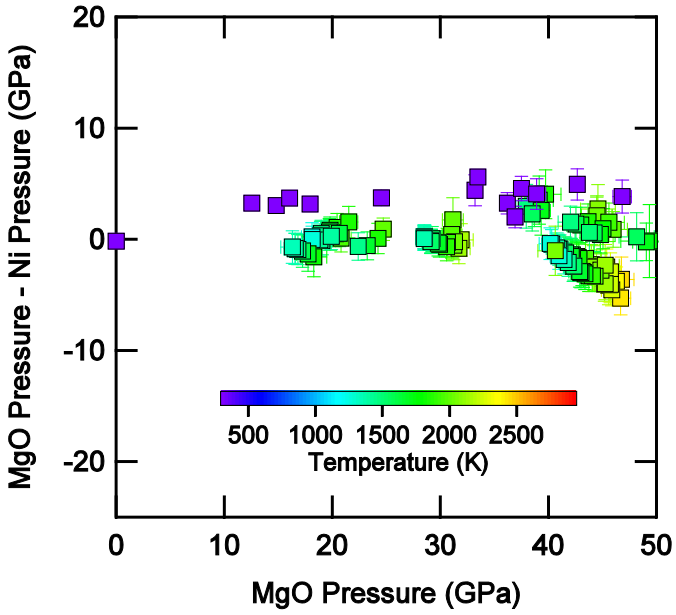

(b)

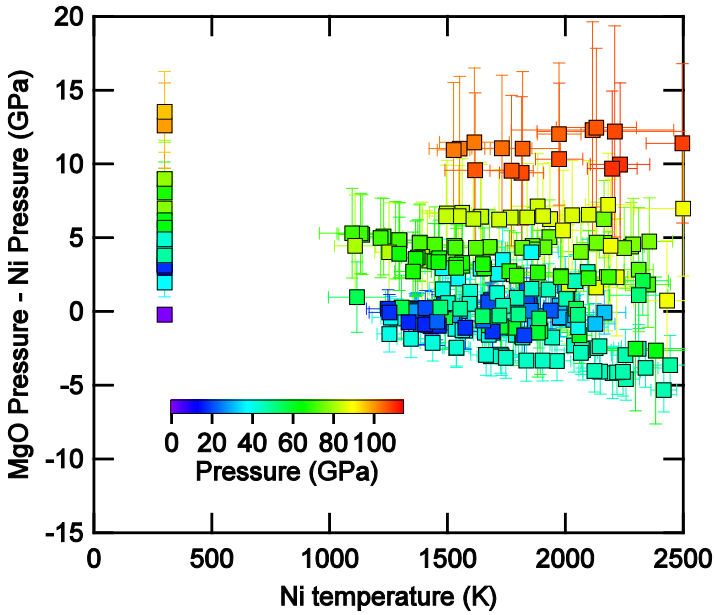

Figure 14. Difference in calculated pressure between the MgO pressure standard (Speziale et al. 2001) and the Ni pressure standard (Campbell et al. 2009) for our measured volumes as a function of pressure and temperature.

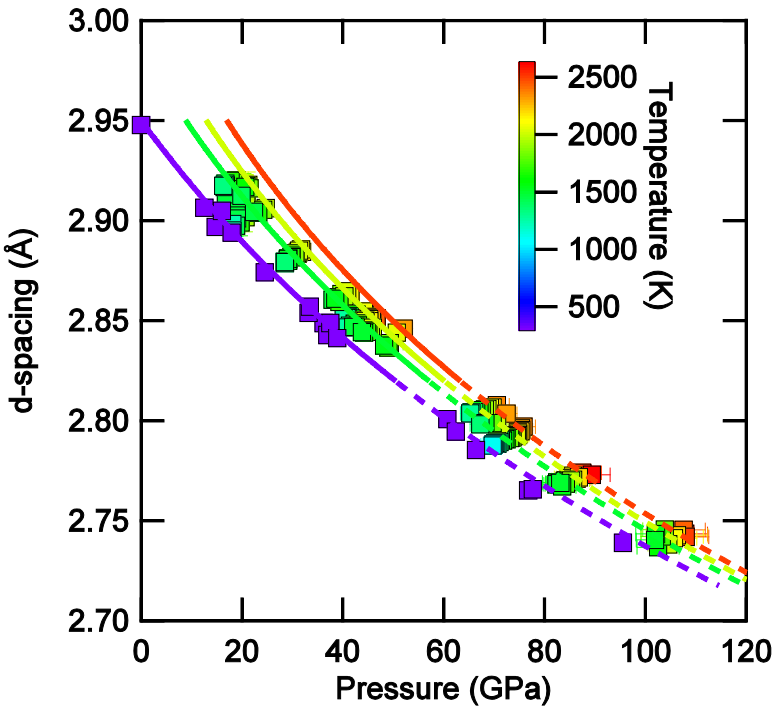

Figure 15. Pressure and temperature dependence of the d-spacing for the SiO_2 (110) diffraction peak. The solid curves represent the predicted d-spacing for stishovite calculated from the equation of state parameters in Table 3. The dashed curves are an extrapolation of the stishovite equation of state.

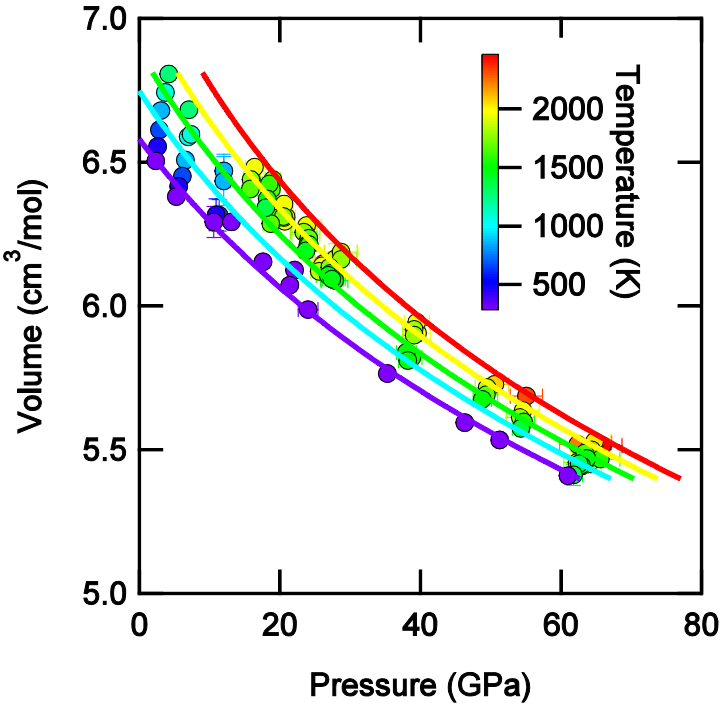

Figure 16. Refitting of *P*-*V*-*T* data for Ni from Campbell et al. (2009). The data from 293–313 K were fit to the BM-EOS and the high-*T* data were fit to the MGD equation of state with the 300 K parameters fixed. The isotherms were calculated based on the fit results, K_0 = 205(4) GPa and γ_0 = 1.86(5). V_0 = 6.579 cm^3/mol, K_0' = 4.4, and q = 1.3 were fixed based on our experimental results using the MgO pressure standard. The Debye temperature is fixed at 415 K (Knacke et al. 1991).

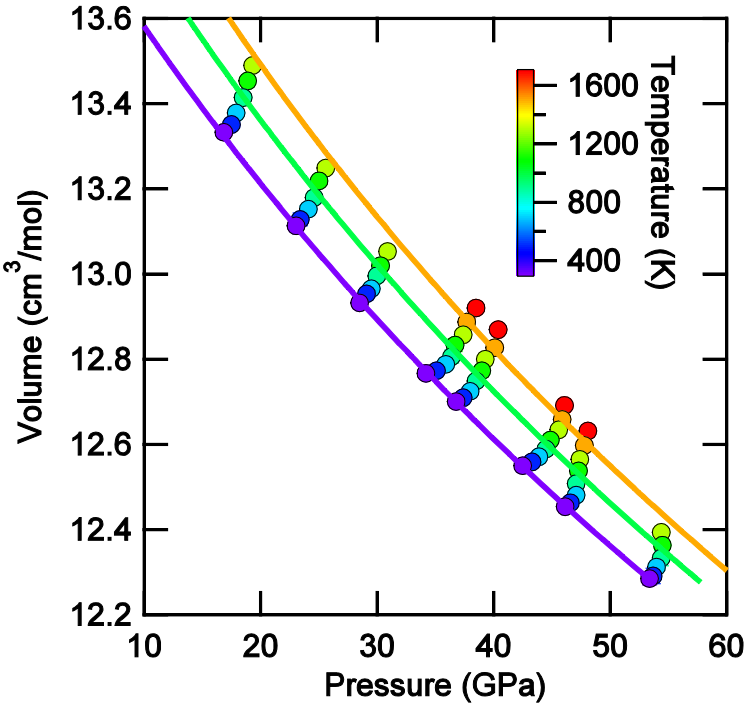

Figure 17. Refitting of *P*-*V*-*T* data for stishovite from Wang et al. (2012). The 300 K data were fit to the BM-EOS and the high-*T* data were fit to the MGD equation of state with the 300 K parameters fixed. The isotherms were calculated based on the fit results, K_0 = 293(3) GPa, K_0' = 4.9(2) and γ_0 = 1.37(1) with V_0 = 14.017 cm^3/mol and q = 1 (assumed). The Debye temperature is fixed at 1109 K (Akaogi et al. 2011).

(a)

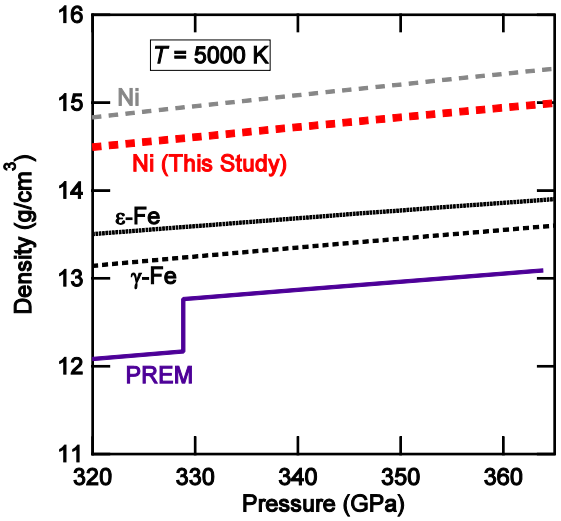

(b)

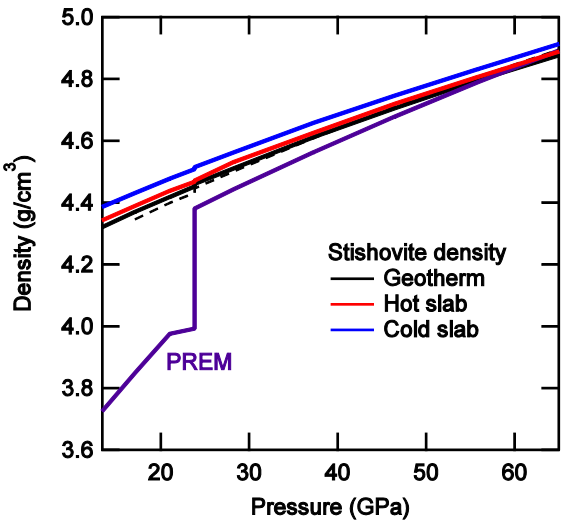

Figure 18. (a) Density of nickel over the pressure range of Earth's inner core (330–365 GPa) extrapolated from the thermal equations of state (Table 3) determined in this study (red) and Campbell et al. (2009) (black). The extrapolated densities of ε-iron (*hcp*) and γ-iron (*fcc*) based on published thermal equations of state (Uchida et al. 2001; Tsujino et al. 2013) are shown for comparison. The Ni and Fe densities were calculated at 5000 K. (b) Density of stishovite throughout the transition zone (~13–24 GPa) and into the mid-lower mantle. The density was calculated from our thermal equation of state (Table 3) along a typical mantle geotherm (black) (Stacy and Davis 2008) and along slab geotherms. The small density jump in the calculated profiles at ~24 GPa is due to the 70 K temperature drop at 670 km depth (Stacy and Davis 2008) due to the latent heat from the breakdown of ringwoodite. The hot (red) and cold (blue) slab geotherms are assumed to be 200 K and 600 K less than the mantle geotherm (e.g. Syracuse et al. 2010). The dashed line corresponds to the density along the mantle geotherm based on the Wang et al. (2012) equation of state. The density according to the seismic Preliminary Reference Earth Model (PREM) (Dziewonski and Anderson 1981) is also shown in (a) and (b).

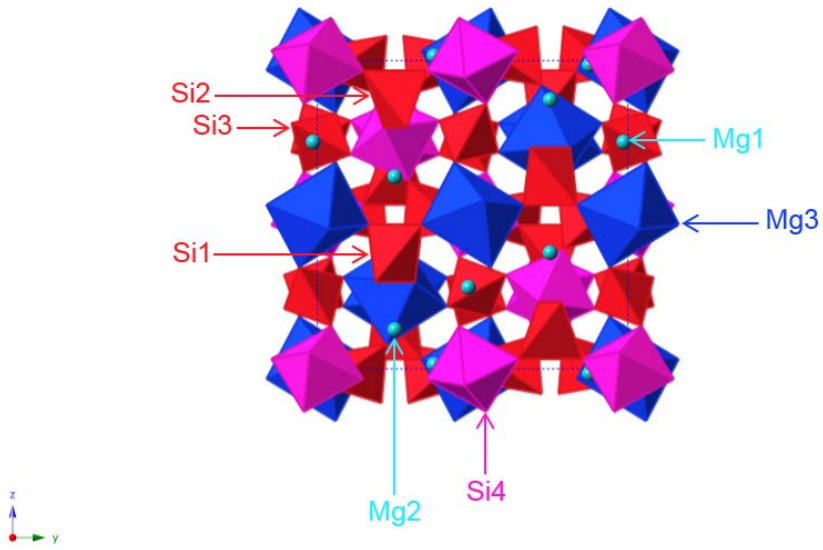

Figure 19. Crystal structure of defect-free $MgSiO_3$ tetragonal garnet optimized using force fields. The two octahedral sites are occupied by Si (pink) and Mg (blue). Mg atoms (light blue) occupy two unique interstitial sites. Three unique tetrahedral sites are occupied by Si.

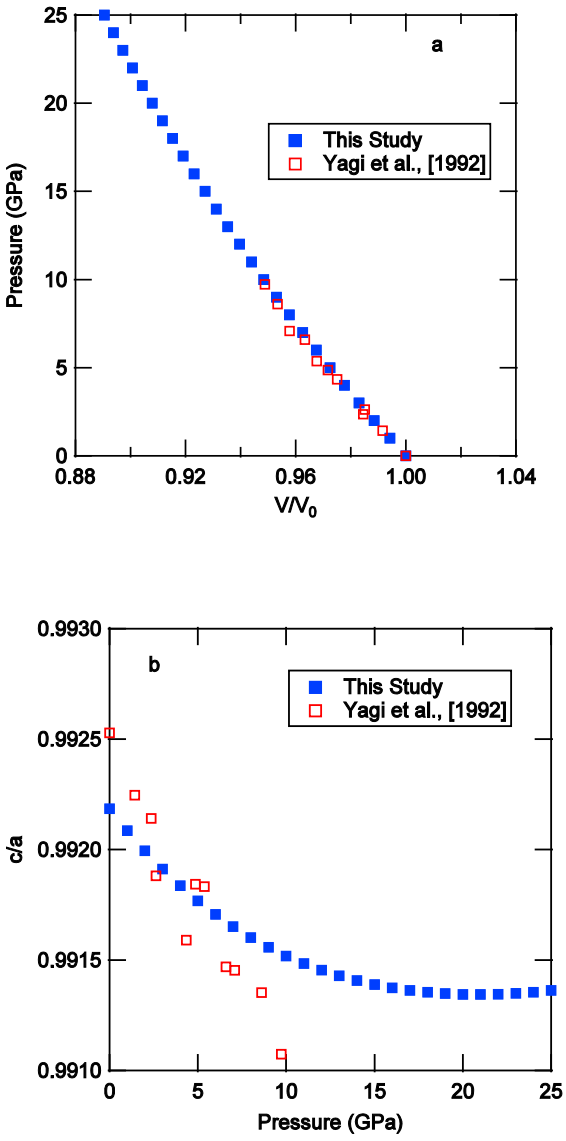

Figure 20. (a) Calculated pressure-volume curve for majorite using interatomic potentials from Table 5 compared to experimental values. The volume is normalized to the zero-pressure value (V_0). Based on fitting our calculated *P*-*V* data to the 2rd-order Birch-Murnaghan equation of state (BM-EOS), the isothermal bulk modulus (K_0) is 170.48(7) GPa. Our bulk modulus is 6% greater than that determined by the high-*P* XRD study of Yagi et al. (1992) (*P* = 0 – 10 GPa), K_0 = 161(4). A 3rd-order fit of our calculated *P*-*V* data to the BM-EOS with K_0 fixed to 169.3 (Table 8) results in the pressure derivative *K*' = 4.15. A 3rd-order BM-EOS fit with no fixed parameters results in K_0 =169.06(2) and *K*' = 4.18. (b) Pressure dependence of the calculated axial ratio (c/a) of majorite using the potentials from Table 5 compared to experimental values. Assuming a linear relationship from *P* = 0 to *P* = 10 GPa, these results have a smaller d(*c*/*a*)/d*P* = 8x10^{-5} GPa^{-1} than experimental d(*c*/*a*)/d*P* = 1.4x10^{-4} GPa^{-1} (Yagi et al. 1992).

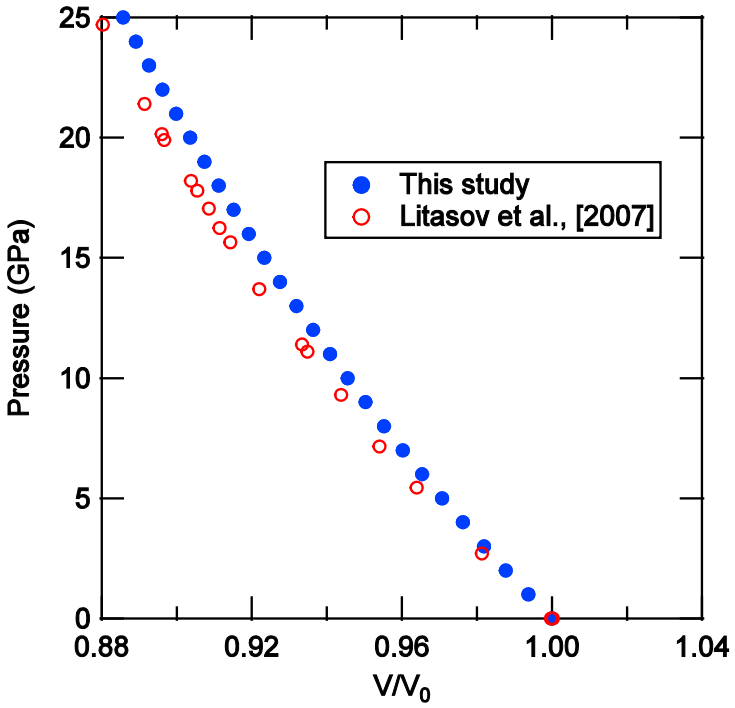

Figure 21. Calculated pressure-volume curve for superhydrous B using the interatomic potentials in Table 5 compared to experimental multi-anvil cell (MAC) values. The bulk modulus determined by our zero-pressure calculations (K_0 = 157.7 GPa) is consistent with the value obtained through fitting our calculated *P*-*V* data with the 3rd-order BM-EOS (K_0 = 160.8(1) GPa and K_0' = 4 (fixed)). If we fix K_0 = 157.7 GPa, the result is K_0' = 4.39. Fitting for both the bulk modulus and its pressure derivative results in K_0 = 158.07(3) and K_0' = 4.35. Our bulk modulus is ~10% greater than the MAC experiments ((K_0 = 146.7(5) GPa and K_0' = 4 (fixed)).

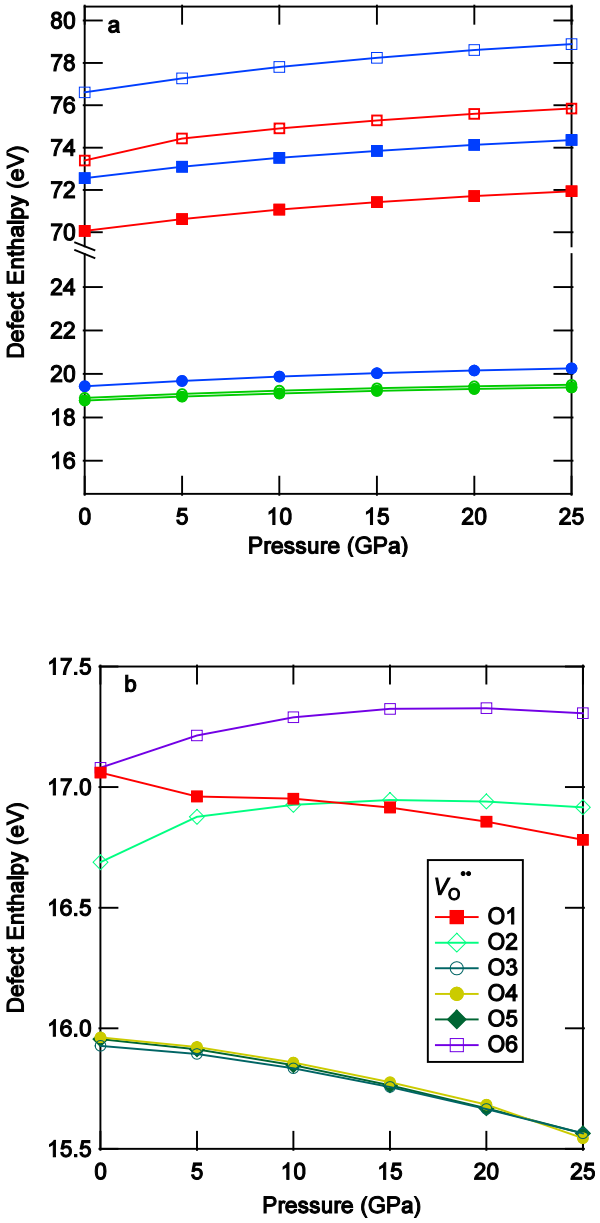

Figure 22. Calculated majorite vacancy formation enthalpies using the force fields. (a) Enthalpy associated with forming charged defects by creating Mg (circles) and Si (squares) vacancies at the ^{IV}Si1 (open blue), ^{IV}Si2 (filled red), ^{IV}Si3 (open red), ^{VI}Si4 (filled blue), ^{VIII}Mg1 (open green), ^{VIII}Mg2 (filled green), and ^{VI}Mg3 (filled blue) sites. (b) Enthalpy associated with generating an oxygen vacancy.

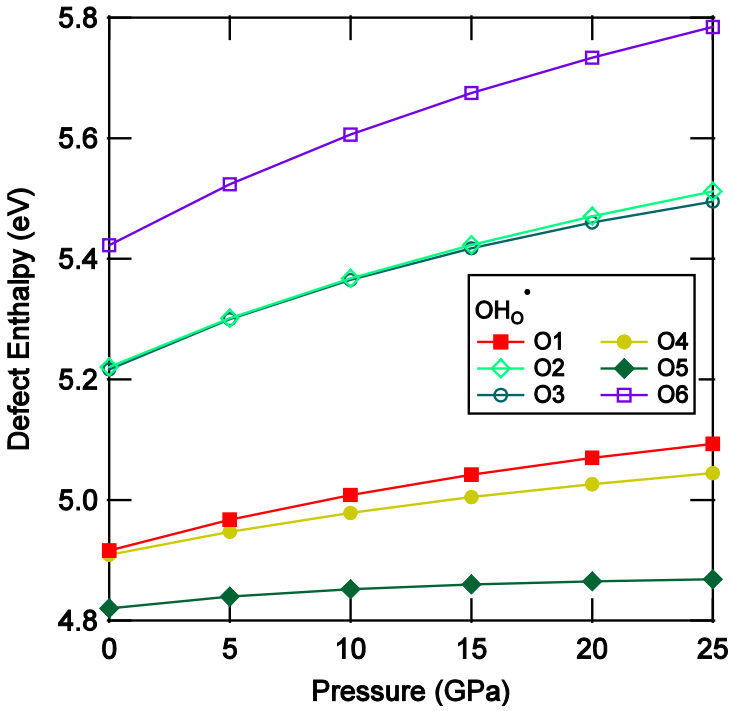

Figure 23. Enthalpy associated with protonating each oxygen site calculated using the force field approach.

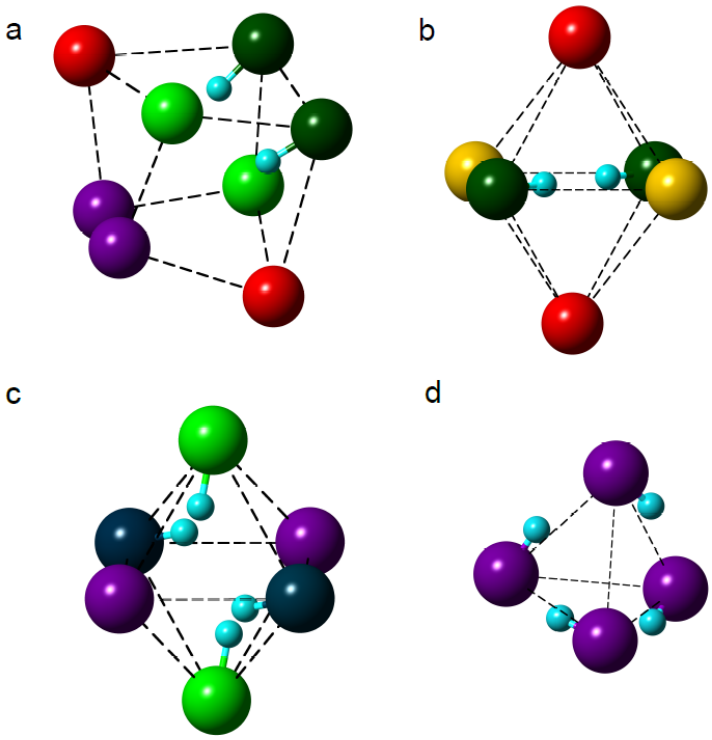

Figure 24. OH-defect structures in $MgSiO_3$ majorite optimized using force fields. Hydrogen atoms are light blue and the oxygen atoms are color-coded according to atomic site where O1 = red, O2 = light green, O3 = dark blue, O4 = yellow, O5 = dark green, O6 = purple. (a) $[\square_{Mg2}+2OH_{O5}]^{X}$; (b) $[\square_{Mg3}+2OH_{O5}]^{X}$; (c) $[\square_{Si4}+2OH_{O2}+2OH_{O3}]^{X}$; (d) "Hydrogarnet"-type $[\square_{Si2}+4OH_{O6}]^{X}$.

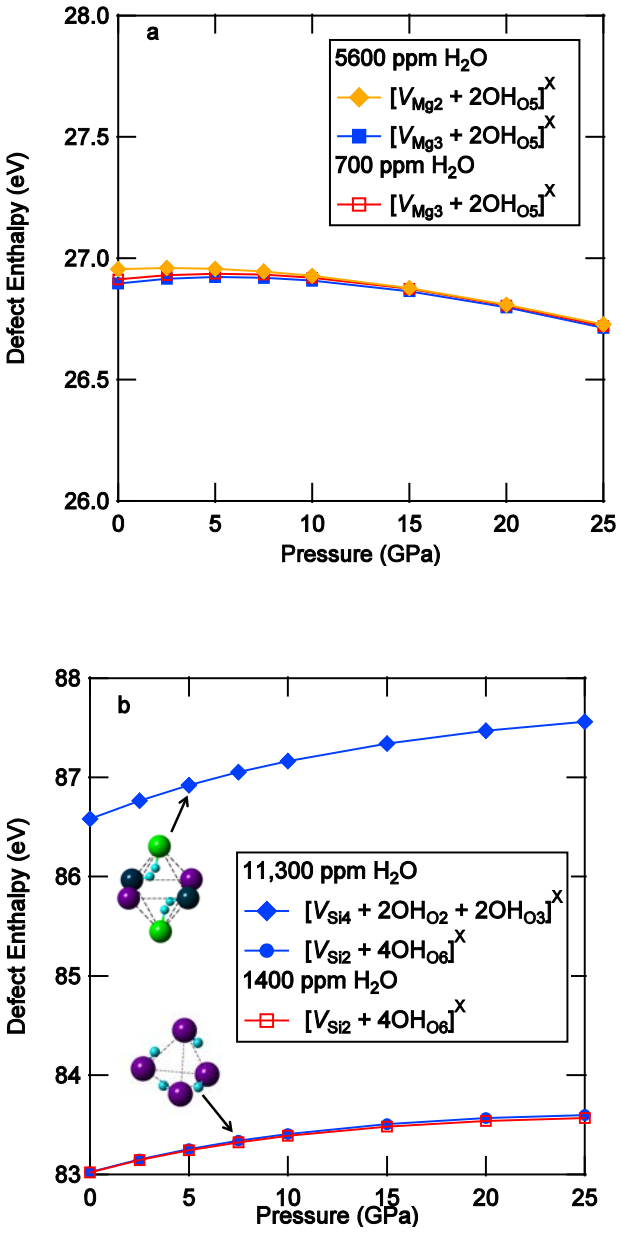

Figure 25. Calculated defect-formation enthalpies using force fields for OH-defect complexes shown in Figure 24. Open symbols represent calculations using a 2 x 2 x 2 supercell, and the filled symbols represent calculations using the 160-atom unit cell. (a) Hydrogen incorporation via Mg vacancies. (b) Hydrogen incorporation via Si vacancies.

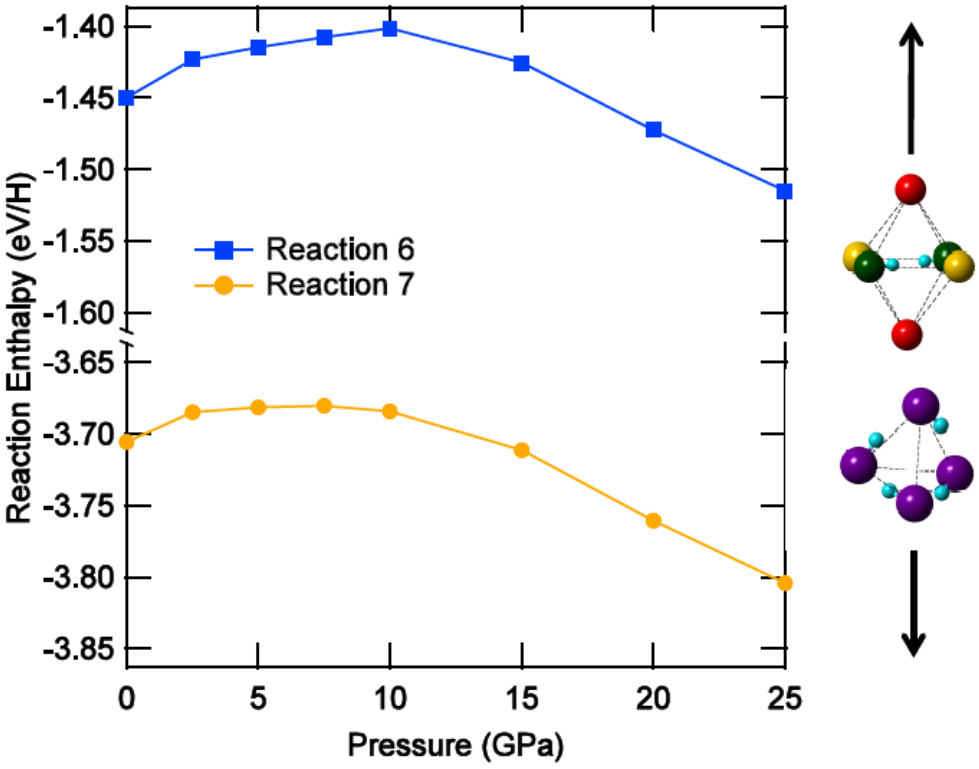

Figure 26. Enthalpies of reactions 4.6 (Al-free) and 4.7 (Al_2O_3 = 0.4 wt%) calculated as a function of pressure using the force field approach. Negative values of the enthalpy correspond to the hydrogarnet defect being favored.

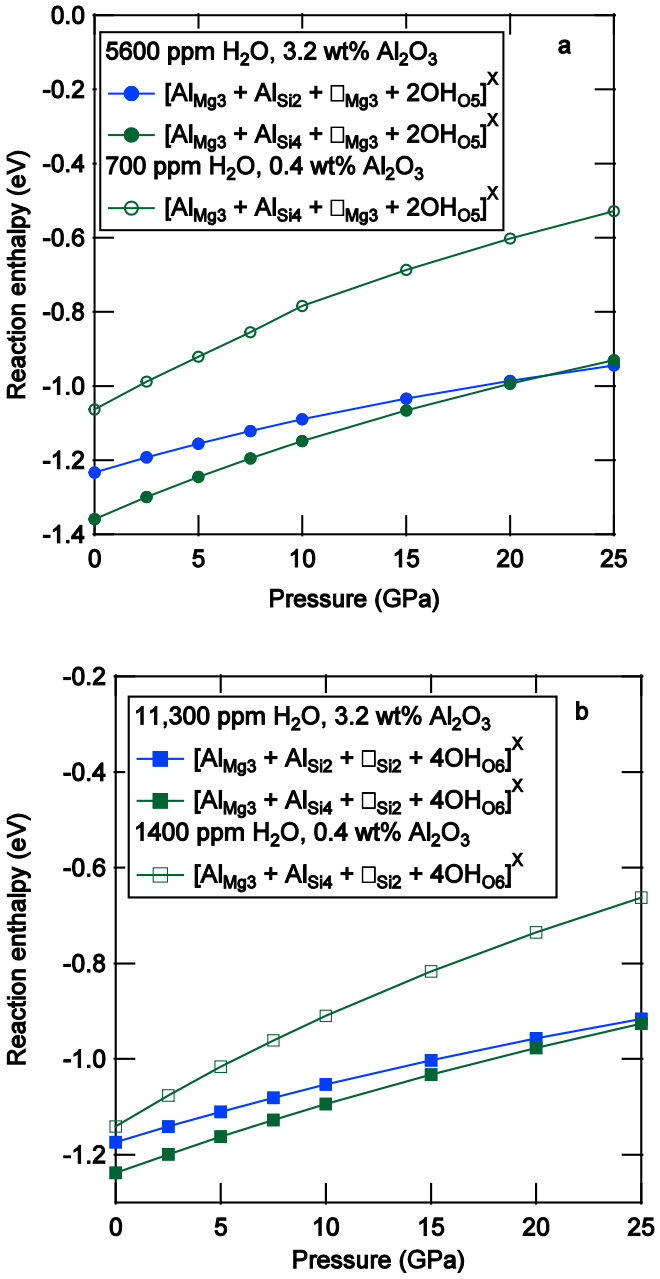

Figure 27. Calculated enthalpies (reactions 4.8 and 4.9) using force fields for hydrogen incorporation via (a) Mg and (b) Si vacancies in the presence of a coupled-substitution of Al for ^{IV}Si or ^{VI}Si and ^{VI}Mg as a function of pressure. Open symbols represent calculations using a 2 × 2 × 2 supercell, and the filled symbols represent calculations using the conventional tetragonal unit cell.

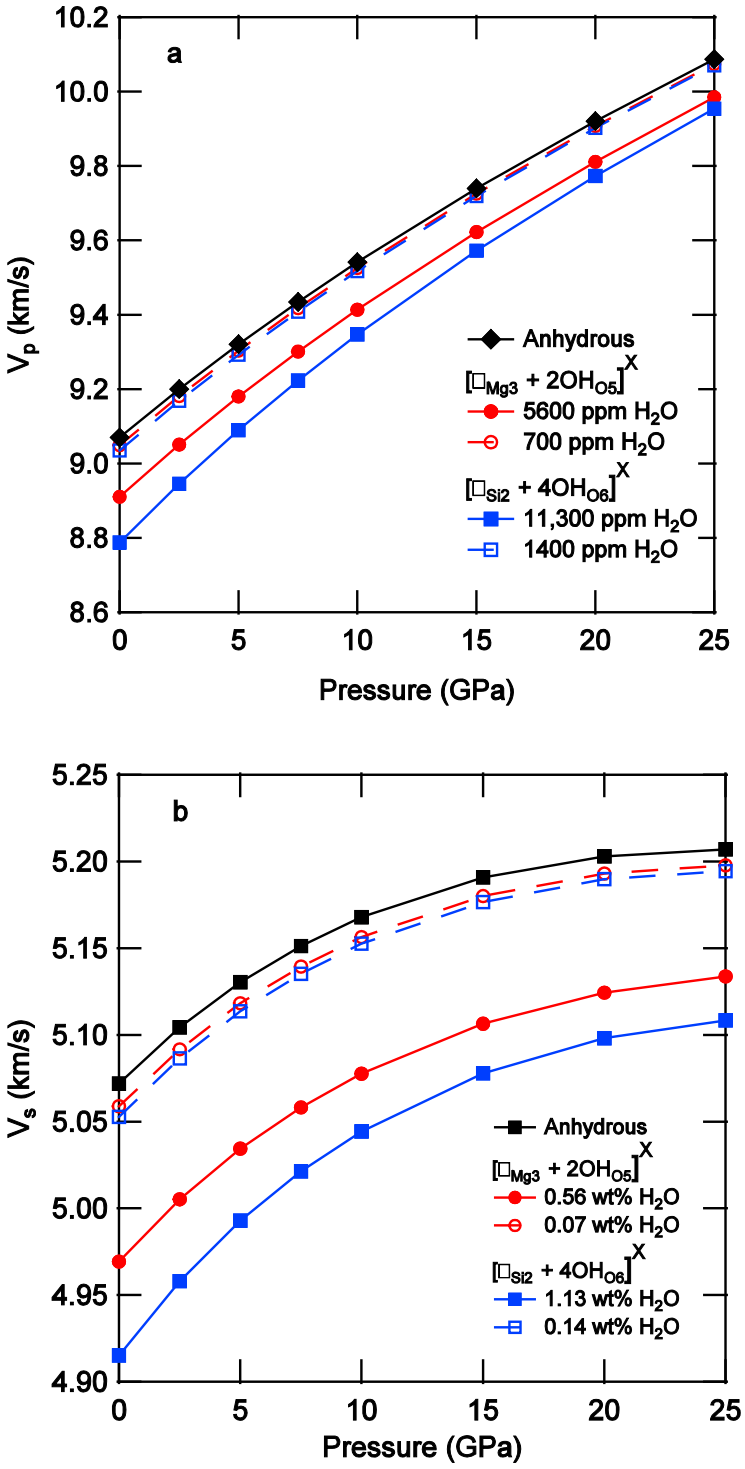

Figure 28. a) v_p and (b) v_s for Al-free anhydrous and hydrous majorite calculated as a function of pressure using force fields.

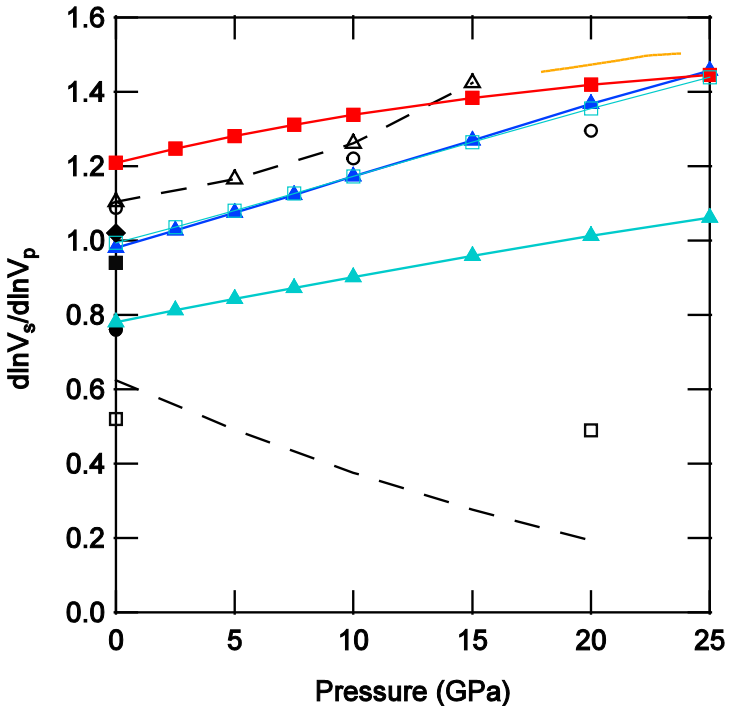

Figure 29. The force field calculated majorite $d\ln v_s/d\ln v_p$ due to compositional changes resulting from OH incorporation compared to experimental and computational results for the olivine polymorphs (Li et al. 2011). The results from this study are shown by red squares ($[\square_{Mg3}+2OH_{O5}]^X$, C_{water} = 1400 ppm), blue triangles ($[\square_{Si2}+4OH_{O6}]^X$, C_{water} = 1400 ppm), light-blue open squares $[\square_{Si2}+4OH_{O6}]^X$, C_{water}= 1.13 wt%) and light-blue triangles $[\square_{Si2}+4OH_{O6}]^X$, C_{water} = 1.13 wt%, C_{Al2O3} = 3.2 wt%). Experimental results (filled black symbols) for forsterite (square) (Mao et al. 2010), wadsleyite (triangle) (Mao et al. 2008), and ringwoodite (circle) (Inoue et al. 1998; Wang et al. 2003) are shown. Additional computational results (black open symbols and dashed lines) are also shown for forsterite (triangles) (Tsuchiya and Tsuchiya 2009), wadsleyite (circles) (Liu et al. 2009), and ringwoodite (squares and dashed line without symbols) (Li et al. 2009; Panero 2010), respectively. For comparison, the thermal $d\ln v_s/d\ln v_p$ for ringwoodite (Li et al. 2011) is shown by the orange line.

Appendix C: Nickel *P-V-T* data

All volumes in cm^3/mol. *T* in K. *P* in GPa. Pressures calculated according to Speziale et al. (2001).

Exp. #	V (Ni)			V (MgO)			T (sample)			T (MgO)			P (total)		
8292	5.813	±	0.0048	9.594	±	0.0097	2311	±	86	1808	±	171	45.4	±	1.21
8293	5.795	±	0.0065	9.591	±	0.0089	2037	±	102	1603	±	204	43.98	±	1.36
8294	5.798	±	0.0044	9.591	±	0.009	1944	±	111	1533	±	221	43.45	±	1.44
8295	5.799	±	0.0049	9.592	±	0.0095	2129	±	77	1671	±	153	44.46	±	1.1
8296	5.791	±	0.0045	9.59	±	0.0098	2075	±	119	1631	±	238	44.21	±	1.56
8297	5.793	±	0.0034	9.592	±	0.0095	2070	±	59	1627	±	117	44.14	±	0.92
8298	5.79	±	0.0014	9.591	±	0.0091	1790	±	67	1418	±	134	42.62	±	0.97
8299	5.79	±	0.0014	9.591	±	0.0098	1816	±	66	1437	±	131	42.76	±	0.96
8300	5.788	±	0.0011	9.589	±	0.0092	1819	±	62	1439	±	123	42.84	±	0.92
8301	5.783	±	0.0008	9.587	±	0.0097	1694	±	72	1346	±	144	42.22	±	1.01
8302	5.779	±	0.0006	9.585	±	0.0096	1659	±	82	1319	±	163	42.09	±	1.1
8303	5.779	±	0.0004	9.587	±	0.0089	1676	±	65	1332	±	129	42.13	±	0.93
8304	5.776	±	0.0013	9.587	±	0.0093	1575	±	62	1256	±	124	41.59	±	0.9
8305	5.774	±	0.0016	9.584	±	0.0091	1534	±	72	1226	±	144	41.44	±	0.98
8306	5.775	±	0.0025	9.584	±	0.0091	1563	±	77	1247	±	154	41.6	±	1.04
8307	5.772	±	0.0032	9.582	±	0.0087	1451	±	63	1163	±	126	41.06	±	0.89
8308	5.77	±	0.0031	9.582	±	0.0088	1419	±	67	1139	±	133	40.89	±	0.92
8309	5.767	±	0.0025	9.581	±	0.0097	1428	±	71	1146	±	142	40.99	±	0.97
8310	5.768	±	0.0034	9.58	±	0.0084	1420	±	62	1140	±	123	40.96	±	0.87
8311	5.767	±	0.0029	9.58	±	0.0088	1387	±	74	1115	±	148	40.79	±	0.98
8312	5.765	±	0.0041	9.578	±	0.0089	1287	±	69	1040	±	138	40.31	±	0.92
8313	5.764	±	0.0045	9.578	±	0.0089	1259	±	79	1019	±	158	40.17	±	1.01
8335	6.139	±	0.0016	10.04	±	0.0062	2166	±	91	1699	±	181	31.93	±	1.12
8336	6.116	±	0.0056	10.04	±	0.0061	2128	±	83	1671	±	165	31.72	±	1.03
8337	6.165	±	0.04	10.04	±	0.006	2000	±	79	1575	±	157	31.17	±	0.97
8338	6.128	±	0.0195	10.04	±	0.0058	1986	±	74	1564	±	147	31.1	±	0.92
8339	6.128	±	0.0134	10.04	±	0.006	1976	±	68	1557	±	136	31.04	±	0.86
8340	6.107	±	0.0045	10.04	±	0.006	1981	±	75	1560	±	149	31.07	±	0.93
8341	6.108	±	0.0056	10.04	±	0.0062	1977	±	79	1557	±	157	31.04	±	0.97

8342	6.113	±	0.0072	10.04	±	0.0062	2035	±	76	1601	±	151	31.25	±	0.94
8343	6.12	±	0.0087	10.04	±	0.0059	2042	±	77	1606	±	153	31.33	±	0.95
8344	6.1	±	0.0073	10.04	±	0.0061	1891	±	77	1493	±	153	30.66	±	0.94
8345	6.086	±	0.0022	10.03	±	0.0061	1870	±	76	1477	±	151	30.59	±	0.93
8346	6.072	±	0.0003	10.03	±	0.0057	1713	±	69	1359	±	137	29.94	±	0.84
8347	6.074	±	0.0009	10.03	±	0.0058	1697	±	70	1347	±	139	29.81	±	0.85
8348	6.065	±	0.0044	10.02	±	0.0055	1553	±	69	1239	±	137	29.23	±	0.82
8349	6.057	±	0.002	10.02	±	0.0056	1531	±	65	1223	±	129	29.15	±	0.78
8350	6.054	±	0.0023	10.02	±	0.0055	1522	±	66	1216	±	131	29.12	±	0.79
8351	6.054	±	0.0028	10.02	±	0.0054	1520	±	66	1215	±	132	29.15	±	0.79
8352	6.053	±	0.0013	10.02	±	0.0057	1520	±	65	1215	±	130	29.15	±	0.78
8353	6.046	±	0.0069	10.02	±	0.0056	1372	±	66	1104	±	131	28.5	±	0.77
8354	6.044	±	0.0072	10.02	±	0.0056	1378	±	67	1108	±	133	28.54	±	0.78
8355	6.043	±	0.0066	10.01	±	0.0054	1362	±	61	1096	±	121	28.5	±	0.72
8356	6.043	±	0.0072	10.01	±	0.0052	1368	±	64	1101	±	128	28.54	±	0.75
8357	6.041	±	0.007	10.01	±	0.0056	1366	±	65	1100	±	130	28.52	±	0.76
8358	6.041	±	0.0065	10.01	±	0.0056	1369	±	64	1101	±	127	28.54	±	0.75
8359	6.039	±	0.0059	10.01	±	0.0059	1363	±	63	1097	±	125	28.51	±	0.74
8246	5.789	±	0.0239	9.573	±	0.0116	2445	±	77	1908	±	153	46.77	±	1.15
8247	5.776	±	0.0008	9.57	±	0.0111	2341	±	53	1830	±	105	46.31	±	0.91
8248	5.788	±	0.0205	9.573	±	0.012	2255	±	59	1766	±	118	45.74	±	0.97
8249	5.754	±	0.011	9.571	±	0.0119	2418	±	55	1888	±	109	46.69	±	0.94
8250	5.758	±	0.0053	9.568	±	0.0112	2201	±	90	1726	±	180	45.59	±	1.27
8251	5.758	±	0.0022	9.571	±	0.0119	2148	±	75	1686	±	150	45.2	±	1.12
8252	5.755	±	0.0078	9.569	±	0.0115	2257	±	57	1768	±	114	45.88	±	0.95
8253	5.761	±	0.0011	9.57	±	0.0115	2219	±	71	1739	±	142	45.64	±	1.08
8254	5.764	±	0.0112	9.571	±	0.0118	2245	±	75	1758	±	149	45.74	±	1.12
8255	5.753	±	0.0016	9.565	±	0.0114	2124	±	66	1668	±	131	45.26	±	1.02
8256	5.773	±	0.0012	9.568	±	0.0117	2066	±	71	1625	±	142	44.87	±	1.07
8257	5.788	±	0.0142	9.569	±	0.0119	2145	±	93	1684	±	186	45.27	±	1.3
8258	5.755	±	0.0012	9.567	±	0.0119	1964	±	59	1548	±	118	44.33	±	0.95
8259	5.744	±	0.0027	9.563	±	0.0118	1835	±	66	1451	±	131	43.76	±	0.99
8260	5.75	±	0.0028	9.565	±	0.012	1904	±	64	1503	±	127	44.07	±	0.98
8261	5.744	±	0.0027	9.564	±	0.0126	1726	±	51	1370	±	102	43.12	±	0.87
8262	5.74	±	0.0038	9.561	±	0.0121	1730	±	57	1373	±	114	43.25	±	0.91
8263	5.739	±	0.003	9.559	±	0.0118	1748	±	66	1386	±	131	43.38	±	0.99
8264	5.736	±	0.0028	9.56	±	0.0125	1685	±	59	1338	±	117	43.01	±	0.92
8265	5.737	±	0.0032	9.56	±	0.0125	1664	±	65	1323	±	130	42.9	±	0.98
8266	5.734	±	0.002	9.557	±	0.0118	1538	±	60	1228	±	119	42.32	±	0.91
8267	5.734	±	0.002	9.555	±	0.0114	1538	±	53	1229	±	106	42.37	±	0.85

8268	5.732	±	0.0008	9.555	±	0.012	1437	±	53	1153	±	106	41.84	±	0.85
8269	5.728	±	0.0002	9.551	±	0.0119	1346	±	60	1084	±	119	41.46	±	0.89
8270	5.727	±	0.0015	9.551	±	0.012	1254	±	52	1015	±	103	40.99	±	0.81
8117	5.556	±	0.0001	9.141	±	0.0237	2941	±	466	2281	±	932	64.89	±	6.4
8118	5.537	±	0.0071	9.136	±	0.0234	2384	±	297	1863	±	593	61.8	±	4.07
8119	5.534	±	0.0104	9.137	±	0.0221	2298	±	244	1798	±	487	61.28	±	3.39
8120	5.562	±	0.008	9.144	±	0.0247	2714	±	200	2111	±	400	63.42	±	2.97
8121	5.534	±	0.0005	9.134	±	0.0241	2060	±	52	1620	±	104	60.01	±	1.44
8123	5.527	±	0.0034	9.131	±	0.0231	1894	±	158	1495	±	315	59.18	±	2.33
8124	5.524	±	0.0045	9.13	±	0.0238	1883	±	162	1487	±	324	59.15	±	2.38
8125	5.524	±	0.0045	9.131	±	0.0255	1780	±	123	1410	±	245	58.5	±	2
8126	5.522	±	0.0048	9.129	±	0.0232	1730	±	127	1372	±	253	58.28	±	1.98
8127	5.52	±	0.0038	9.129	±	0.0226	1726	±	113	1370	±	226	58.28	±	1.85
8128	5.521	±	0.0039	9.132	±	0.0249	1676	±	97	1332	±	194	57.87	±	1.74
8129	5.517	±	0.0053	9.128	±	0.0257	1491	±	87	1193	±	174	56.95	±	1.65
8130	5.515	±	0.0069	9.126	±	0.024	1306	±	93	1054	±	185	56	±	1.62
8131	5.512	±	0.008	9.121	±	0.0213	1116	±	121	912	±	242	55.12	±	1.75
8028	5.434	±	0.0098	8.799	±	0.0268	2357	±	99	1842	±	197	75.85	±	2.34
8029	5.426	±	0.0206	8.799	±	0.0286	2279	±	57	1784	±	113	75.38	±	2.11
8030	5.429	±	0.0196	8.8	±	0.0298	2288	±	82	1791	±	163	75.39	±	2.28
8031	5.422	±	0.0046	8.797	±	0.0276	2250	±	79	1762	±	157	75.3	±	2.2
8032	5.423	±	0.0122	8.798	±	0.0293	2166	±	92	1699	±	183	74.73	±	2.32
8033	5.445	±	0.0022	8.796	±	0.0277	2164	±	68	1698	±	136	74.84	±	2.13
8034	5.419	±	0.0021	8.793	±	0.0255	2133	±	84	1674	±	167	74.78	±	2.18
8035	5.413	±	0.0052	8.791	±	0.025	1932	±	52	1524	±	104	73.65	±	1.97
8036	5.405	±	0.0027	8.789	±	0.0245	2066	±	79	1625	±	158	74.54	±	2.12
8037	5.401	±	5e-6	8.787	±	0.024	1911	±	57	1508	±	114	73.68	±	1.97
8038	5.399	±	0.0012	8.786	±	0.0241	1862	±	71	1471	±	141	73.44	±	2.04
8039	5.396	±	0.0007	8.787	±	0.0253	1862	±	68	1471	±	135	73.4	±	2.05
8040	5.394	±	0.003	8.785	±	0.0248	1817	±	62	1438	±	124	73.21	±	2
8041	5.387	±	0.0025	8.783	±	0.0237	1679	±	68	1334	±	136	72.48	±	1.99
8042	5.387	±	0.0025	8.782	±	0.0244	1679	±	51	1334	±	101	72.51	±	1.92
8043	5.382	±	0.0022	8.78	±	0.0233	1621	±	51	1290	±	101	72.26	±	1.89
8044	5.379	±	0.0024	8.779	±	0.024	1529	±	62	1221	±	123	71.75	±	1.94
8045	5.377	±	0.0023	8.778	±	0.0229	1534	±	77	1225	±	153	71.82	±	1.99
8046	5.375	±	0.0026	8.777	±	0.0229	1447	±	70	1160	±	139	71.36	±	1.94
8047	5.373	±	0.0033	8.775	±	0.0237	1383	±	79	1112	±	157	71.08	±	1.99
8048	5.372	±	0.0037	8.775	±	0.0237	1382	±	72	1112	±	144	71.08	±	1.96
8049	5.369	±	0.003	8.773	±	0.0226	1280	±	85	1035	±	170	70.57	±	1.98
8050	5.37	±	0.0039	8.774	±	0.0243	1298	±	68	1048	±	135	70.62	±	1.93

8051	5.369	±	0.0039	8.772	±	0.0239	1295	±	65	1046	±	130	70.68	±	1.91
8052	5.368	±	0.0042	8.77	±	0.0222	1229	±	82	996	±	163	70.41	±	1.94
8053	5.367	±	0.0042	8.772	±	0.0245	1216	±	92	987	±	184	70.26	±	2.05
8054	5.365	±	0.004	8.769	±	0.0235	1138	±	99	929	±	198	69.9	±	2.04
8055	5.365	±	0.0044	8.768	±	0.023	1132	±	101	924	±	201	69.94	±	2.04
8056	5.364	±	0.0048	8.768	±	0.0253	1096	±	139	897	±	277	69.72	±	2.35
8088	5.255	±	0.0109	8.568	±	0.0273	2827	±	258	2195	±	516	89.97	±	4.5
8089	5.249	±	0.0067	8.566	±	0.028	2218	±	140	1739	±	280	86.26	±	3.2
8090	5.248	±	0.0079	8.565	±	0.0286	2177	±	95	1707	±	189	86.04	±	2.88
8091	5.239	±	0.0056	8.566	±	0.0285	2432	±	143	1899	±	285	87.57	±	3.27
8092	5.236	±	0.0016	8.563	±	0.0276	2131	±	194	1673	±	387	85.86	±	3.65
8093	5.233	±	0.0018	8.561	±	0.0283	2014	±	151	1586	±	302	85.24	±	3.26
8094	5.231	±	0.0046	8.558	±	0.029	1781	±	101	1411	±	202	83.9	±	2.86
8095	5.228	±	0.0065	8.555	±	0.0275	1393	±	129	1119	±	257	81.71	±	2.88
8096	5.226	±	0.0047	8.555	±	0.0281	1538	±	88	1229	±	176	82.58	±	2.7
8097	5.224	±	0.0071	8.553	±	0.0283	1415	±	65	1136	±	130	81.96	±	2.57
8098	5.222	±	0.0082	8.549	±	0.0285	1253	±	61	1014	±	121	81.17	±	2.51
8099	5.22	±	0.0098	8.546	±	0.0287	1108	±	87	906	±	174	80.44	±	2.57
8372	6.4	±	0.0055	10.48	±	0.0142	1938	±	77	1529	±	154	20.81	±	0.93
8376	6.369	±	0.0166	10.47	±	0.0131	1705	±	79	1353	±	157	19.81	±	0.92
8377	6.391	±	0.0018	10.47	±	0.0129	1815	±	73	1436	±	145	20.3	±	0.87
8378	6.415	±	0.0206	10.47	±	0.0135	1849	±	68	1462	±	136	20.44	±	0.83
8379	6.397	±	0.0006	10.47	±	0.0129	1837	±	57	1453	±	114	20.42	±	0.72
8383	6.379	±	0.0151	10.47	±	0.0124	1685	±	72	1338	±	143	19.79	±	0.84
8384	6.375	±	0.0129	10.47	±	0.013	1690	±	71	1342	±	141	19.78	±	0.84
8385	6.372	±	0.0118	10.46	±	0.0128	1673	±	76	1330	±	152	19.74	±	0.89
8386	6.336	±	0.0189	10.46	±	0.0125	1484	±	68	1188	±	135	18.99	±	0.78
8387	6.329	±	0.0203	10.46	±	0.0129	1472	±	74	1179	±	148	18.93	±	0.85
8388	6.308	±	0.0041	10.45	±	0.0087	1457	±	89	1168	±	178	19.04	±	0.98
8389	6.309	±	0.0025	10.45	±	0.0115	1435	±	102	1151	±	203	18.87	±	1.11
8390	6.287	±	0.0031	10.44	±	0.0117	1247	±	91	1010	±	182	18.12	±	0.98
8391	6.281	±	0.0013	10.44	±	0.0117	1254	±	86	1015	±	171	18.15	±	0.93
8410	6.392	±	0.0291	10.57	±	0.0168	1826	±	102	1445	±	204	18.3	±	1.18
8411	6.378	±	0.0223	10.57	±	0.0163	1692	±	93	1344	±	185	17.76	±	1.07
8412	6.368	±	0.0177	10.56	±	0.0166	1576	±	91	1257	±	181	17.24	±	1.03
8415	6.352	±	0.0162	10.56	±	0.0161	1463	±	84	1172	±	168	16.81	±	0.95
8416	6.346	±	0.0134	10.56	±	0.0159	1406	±	93	1129	±	185	16.57	±	1.03
8417	6.346	±	0.0152	10.56	±	0.0163	1406	±	89	1129	±	177	16.58	±	0.99
8418	6.338	±	0.0147	10.55	±	0.0159	1336	±	98	1077	±	195	16.31	±	1.07
10057	5.341	±	0.015	8.58	±	0.0297	2509	±	56	1956	±	111	87.33	±	2.72

10058	5.325	±	0.0056	8.576	±	0.0262	2500	±	207	1950	±	414	87.48	±	3.83
10059	5.313	±	0.0121	8.572	±	0.0221	2182	±	96	1711	±	191	85.7	±	2.72
10061	5.299	±	0.0115	8.569	±	0.0253	2099	±	113	1649	±	226	85.32	±	2.9
10062	5.296	±	0.013	8.57	±	0.025	2029	±	116	1597	±	232	84.87	±	2.89
10063	5.295	±	0.0106	8.565	±	0.0227	1883	±	113	1487	±	225	84.19	±	2.8
10065	5.287	±	0.0063	8.565	±	0.0253	1935	±	139	1526	±	278	84.52	±	3.06
10066	5.283	±	0.0061	8.563	±	0.0239	1838	±	128	1454	±	256	84.02	±	2.93
10067	5.278	±	0.006	8.56	±	0.0231	1769	±	96	1401	±	191	83.75	±	2.68
10068	5.273	±	0.0053	8.559	±	0.0241	1562	±	138	1247	±	276	82.53	±	2.93
10069	5.272	±	0.0057	8.558	±	0.0231	1641	±	138	1305	±	275	83.08	±	2.94
10070	5.272	±	0.0148	8.557	±	0.0229	1643	±	92	1307	±	184	83.14	±	2.63
10071	5.268	±	0.0148	8.556	±	0.0242	1610	±	108	1283	±	216	82.99	±	2.75
10072	5.267	±	0.0151	8.554	±	0.0238	1498	±	103	1198	±	205	82.4	±	2.67
10086	5.332	±	0.0235	8.554	±	0.0344	2624	±	162	2043	±	324	89.4	±	3.64
10087	5.265	±	0.0362	8.551	±	0.0296	2192	±	51	1719	±	102	86.85	±	2.74
10088	5.269	±	0.0138	8.549	±	0.031	1991	±	136	1568	±	271	85.69	±	3.23
10089	5.276	±	0.0111	8.546	±	0.0297	1905	±	74	1504	±	148	85.3	±	2.8
10090	5.264	±	0.0002	8.544	±	0.0316	1719	±	54	1364	±	108	84.27	±	2.74
10091	5.256	±	0.0021	8.538	±	0.0293	1547	±	82	1235	±	164	83.52	±	2.76
10092	5.255	±	0.0037	8.539	±	0.031	1495	±	81	1196	±	161	83.15	±	2.78
10138	5.084	±	0.0137	8.168	±	0.0076	2232	±	126	1749	±	252	108.8	±	4.57
10139	5.08	±	0.0028	8.168	±	0.0072	2199	±	106	1724	±	211	108.6	±	4.45
10140	5.08	±	0.0004	8.167	±	0.0078	1974	±	100	1556	±	200	107.1	±	4.34
10141	5.064	±	0.0077	8.164	±	0.008	1815	±	94	1436	±	187	106.3	±	4.25
10142	5.065	±	0.0049	8.165	±	0.0086	1772	±	92	1404	±	184	105.9	±	4.22
10143	5.06	±	0.0072	8.164	±	0.0073	1618	±	128	1288	±	255	105	±	4.29
10161	5.134	±	0.0139	8.211	±	0.0062	2116	±	345	1662	±	689	105.4	±	6.17
10162	5.134	±	0.0092	8.209	±	0.0074	2497	±	154	1947	±	307	108	±	4.57
10163	5.132	±	0.0078	8.206	±	0.0076	2210	±	330	1732	±	659	106.3	±	6.09
10164	5.134	±	0.0062	8.207	±	0.0064	2132	±	170	1674	±	339	105.7	±	4.56
10165	5.125	±	0.0061	8.209	±	0.008	1974	±	93	1555	±	185	104.6	±	4.04
10166	5.106	±	0.0015	8.204	±	0.0068	1819	±	161	1439	±	321	103.9	±	4.37
10167	5.105	±	0.0045	8.204	±	0.0072	1615	±	148	1286	±	295	102.5	±	4.17
10168	5.104	±	0.0028	8.205	±	0.0065	1731	±	127	1373	±	254	103.3	±	4.11
10169	5.098	±	0.0034	8.205	±	0.0076	1552	±	130	1239	±	259	102.1	±	4.02
10170	5.096	±	0.0041	8.204	±	0.0074	1526	±	69	1220	±	138	102	±	3.74
10398	6.393	±	0.0284	10.42	±	0.016	1836	±	67	1452	±	134	21.52	±	0.84
10399	6.318	±	0.0178	10.4	±	0.0131	1596	±	65	1272	±	130	20.66	±	0.78
10400	6.28	±	0.019	10.39	±	0.0131	1406	±	64	1130	±	128	19.91	±	0.75
10416	6.325	±	0.0115	10.31	±	0.0097	2009	±	54	1581	±	107	24.71	±	0.69

10417	6.272	±	0.0295	10.3	±	0.008	1854	±	50	1466	±	100	24.23	±	0.64
10418	6.228	±	0.0243	10.3	±	0.0093	1652	±	53	1314	±	106	23.24	±	0.66
10419	6.198	±	0.0227	10.29	±	0.0095	1456	±	56	1167	±	112	22.4	±	0.67
10222	5.89	±	0.0166	9.704	±	0.0108	2054	±	127	1616	±	254	40.64	±	1.61
10223	5.979	±	0.0268	9.698	±	0.009	1856	±	115	1467	±	229	39.74	±	1.44
10224	5.955	±	0.0299	9.696	±	0.009	1735	±	105	1376	±	209	39.15	±	1.31
10225	5.933	±	0.0237	9.694	±	0.0096	1641	±	83	1306	±	166	38.7	±	1.08
10226	5.917	±	0.032	9.69	±	0.0089	1479	±	74	1184	±	148	37.96	±	0.96
10235	5.926	±	0.0405	9.686	±	0.0076	1714	±	61	1361	±	122	39.34	±	0.85
10236	5.904	±	0.0232	9.683	±	0.0066	1545	±	53	1234	±	106	38.51	±	0.75
10252	5.894	±	0.0236	9.581	±	0.0332	2095	±	93	1646	±	185	44.6	±	1.6
10253	5.873	±	0.0025	9.576	±	0.03	2043	±	78	1607	±	156	44.49	±	1.41
10254	5.873	±	0.0101	9.575	±	0.0291	2042	±	82	1607	±	164	44.49	±	1.43
10255	5.843	±	0.0036	9.569	±	0.0294	1857	±	68	1468	±	136	43.68	±	1.31
10256	5.823	±	0.0043	9.565	±	0.03	1711	±	66	1358	±	131	43.01	±	1.3
10257	5.813	±	0.0048	9.56	±	0.027	1596	±	62	1272	±	124	42.55	±	1.2
10258	5.804	±	0.0033	9.555	±	0.0264	1480	±	58	1185	±	116	42.06	±	1.15
10268	5.811	±	0.0035	9.522	±	0.0328	2003	±	53	1577	±	106	45.99	±	1.33
10269	5.817	±	0.005	9.521	±	0.0332	1928	±	69	1521	±	138	45.6	±	1.44
10270	5.792	±	0.0116	9.514	±	0.031	1794	±	73	1420	±	145	45.07	±	1.4
10271	5.776	±	0.0045	9.512	±	0.032	1736	±	64	1377	±	127	44.82	±	1.36
10272	5.764	±	0.0051	9.506	±	0.0295	1593	±	67	1270	±	134	44.23	±	1.32
10273	5.757	±	0.0087	9.504	±	0.0305	1502	±	67	1201	±	133	43.8	±	1.33
10313	5.468	±	0.0056	8.917	±	0.0388	2351	±	95	1838	±	190	70.58	±	2.41
10314	5.465	±	0.0193	8.914	±	0.0379	2184	±	81	1713	±	162	69.72	±	2.29
10315	5.46	±	0.025	8.914	±	0.0383	2099	±	75	1649	±	150	69.18	±	2.25
10316	5.453	±	0.0207	8.91	±	0.0354	1981	±	75	1560	±	150	68.69	±	2.16
10317	5.45	±	0.0172	8.907	±	0.0339	1883	±	74	1487	±	148	68.21	±	2.1
10318	5.444	±	0.0153	8.906	±	0.0348	1763	±	59	1397	±	118	67.57	±	2.04
10319	5.44	±	0.0127	8.903	±	0.0342	1656	±	75	1317	±	150	67.03	±	2.09
10320	5.437	±	0.011	8.902	±	0.0334	1563	±	77	1247	±	153	66.55	±	2.07
10321	5.433	±	0.0079	8.899	±	0.0334	1445	±	69	1158	±	138	65.99	±	2.01
10322	5.433	±	0.007	8.897	±	0.0338	1374	±	68	1106	±	135	65.64	±	2.01
10323	5.437	±	0.0083	8.897	±	0.0327	1465	±	73	1174	±	146	66.17	±	2.02
10324	5.439	±	0.0098	8.9	±	0.0339	1562	±	71	1247	±	142	66.61	±	2.05
10325	5.442	±	0.0131	8.901	±	0.0329	1650	±	76	1313	±	151	67.12	±	2.06
10326	5.436	±	0.0108	8.9	±	0.0343	1537	±	75	1228	±	149	66.47	±	2.08
10327	5.434	±	0.0075	8.899	±	0.034	1462	±	68	1172	±	135	66.09	±	2.03
10328	5.431	±	0.0064	8.898	±	0.0344	1365	±	68	1099	±	135	65.57	±	2.02
10329	5.431	±	0.0051	8.895	±	0.0336	1296	±	63	1047	±	125	65.28	±	1.97

10337	5.449	±	0.0477	8.868	±	0.0306	2311	±	61	1808	±	122	72.49	±	2.06
10338	5.424	±	0.032	8.865	±	0.03	1982	±	84	1561	±	167	70.64	±	2.14
10339	5.413	±	0.0209	8.86	±	0.0276	1794	±	65	1420	±	129	69.72	±	1.95
10340	5.407	±	0.0089	8.857	±	0.0279	1537	±	85	1227	±	169	68.32	±	2.03
10341	5.394	±	0.009	8.856	±	0.0306	1354	±	78	1091	±	156	67.29	±	2.03
10360	5.694	±	0.0119	9.267	±	0.0237	2329	±	109	1821	±	217	56.57	±	1.8
10361	5.639	±	0.0009	9.262	±	0.0182	2046	±	57	1610	±	114	55.14	±	1.22
10362	5.622	±	0.0089	9.267	±	0.026	1889	±	78	1492	±	156	54.06	±	1.52
10363	5.607	±	0.0086	9.263	±	0.0275	1649	±	90	1312	±	180	52.82	±	1.62
10364	5.604	±	0.014	9.26	±	0.0265	1470	±	112	1177	±	223	51.93	±	1.75
10383	5.755	±	0.0029	9.391	±	0.0169	2311	±	124	1808	±	248	52.07	±	1.79
10384	5.711	±	0.0057	9.388	±	0.0188	2054	±	114	1615	±	227	50.71	±	1.66
10385	5.693	±	0.0044	9.387	±	0.0217	1801	±	204	1426	±	408	49.35	±	2.64
10386	5.683	±	0.0029	9.382	±	0.0149	1720	±	81	1365	±	162	49.06	±	1.25
10387	5.68	±	0.0094	9.381	±	0.0202	1554	±	117	1240	±	233	48.17	±	1.64
8314	5.743	±	0.0106	9.555	±	0.0084	300	±	0	300	±	0	36.21	±	0.26
8360	5.99	±	0.0123	9.971	±	0.0052	300	±	0	300	±	0	24.55	±	0.14
8271	5.707	±	0.0073	9.531	±	0.0128	300	±	0	300	±	0	36.92	±	0.4
8132	5.507	±	0.009	9.113	±	0.0237	300	±	0	300	±	0	51.35	±	0.9
8057	5.35	±	0.0094	8.751	±	0.0241	300	±	0	300	±	0	66.42	±	1.1
8100	5.209	±	0.0119	8.534	±	0.0271	300	±	0	300	±	0	76.81	±	1.38
8392	6.214	±	0.0095	10.39	±	0.0116	300	±	0	300	±	0	14.82	±	0.25
8419	6.284	±	0.0105	10.5	±	0.0155	300	±	0	300	±	0	12.55	±	0.31
10073	5.233	±	0.0079	8.535	±	0.0267	300	±	0	300	±	0	76.77	±	1.36
10093	5.222	±	0.0105	8.517	±	0.0276	300	±	0	300	±	0	77.7	±	1.42
10144	5.039	±	0.0044	8.15	±	0.0072	300	±	0	300	±	0	98.28	±	0.48
10171	5.076	±	0.0062	8.195	±	0.0072	300	±	0	300	±	0	95.55	±	0.47
10401	6.199	±	0.0113	10.33	±	0.0124	300	±	0	300	±	0	16.06	±	0.27
10420	6.135	±	0.0068	10.25	±	0.0116	300	±	0	300	±	0	17.95	±	0.26
10227	5.822	±	0.0241	9.654	±	0.0083	300	±	0	300	±	0	33.21	±	0.25
10237	5.84	±	0.004	9.645	±	0.0073	300	±	0	300	±	0	33.48	±	0.22
10259	5.744	±	0.0073	9.513	±	0.0231	300	±	0	300	±	0	37.5	±	0.73
10274	5.709	±	0.0133	9.469	±	0.0263	300	±	0	300	±	0	38.91	±	0.85
10330	5.401	±	0.007	8.879	±	0.0319	300	±	0	300	±	0	60.76	±	1.37
10342	5.372	±	0.0041	8.841	±	0.0289	300	±	0	300	±	0	62.4	±	1.26
10365	5.571	±	0.0103	9.235	±	0.0236	300	±	0	300	±	0	46.84	±	0.85
10388	5.658	±	0.0159	9.354	±	0.0178	300	±	0	300	±	0	42.67	±	0.61

Appendix D: Stishovite *P-V-T* data

All volumes in cm^3/mol. *T* in K. *P* in GPa. Pressures calculated according to Speziale et al. (2001).

Exp. #	V (SiO_2)			V (MgO)			T (sample)			T (MgO)			P (total)		
8292	12.819	±	0.013	9.594	±	0.0097	2311	±	86	1808	±	171	45.4	±	1.21
8293	12.808	±	0.02	9.591	±	0.0089	2037	±	102	1603	±	204	43.98	±	1.36
8294	12.809	±	0.02	9.591	±	0.009	1944	±	111	1533	±	221	43.45	±	1.44
8295	12.802	±	0.008	9.592	±	0.0095	2129	±	77	1671	±	153	44.46	±	1.1
8296	12.802	±	0.021	9.59	±	0.0098	2075	±	119	1631	±	238	44.21	±	1.56
8297	12.806	±	0.027	9.592	±	0.0095	2070	±	59	1627	±	117	44.14	±	0.92
8298	12.79	±	0.017	9.591	±	0.0091	1790	±	67	1418	±	134	42.62	±	0.97
8299	12.805	±	0.012	9.591	±	0.0098	1816	±	66	1437	±	131	42.76	±	0.96
8300	12.789	±	0.032	9.589	±	0.0092	1819	±	62	1439	±	123	42.84	±	0.92
8301	12.806	±	0.021	9.587	±	0.0097	1694	±	72	1346	±	144	42.22	±	1.01
8302	12.809	±	0.036	9.585	±	0.0096	1659	±	82	1319	±	163	42.09	±	1.1
8303	12.806	±	0.019	9.587	±	0.0089	1676	±	65	1332	±	129	42.13	±	0.93
8304	12.805	±	0.035	9.587	±	0.0093	1575	±	62	1256	±	124	41.59	±	0.9
8305	12.799	±	0.015	9.584	±	0.0091	1534	±	72	1226	±	144	41.44	±	0.98
8306	12.765	±	0.033	9.584	±	0.0091	1563	±	77	1247	±	154	41.6	±	1.04
8307	12.795	±	0.019	9.582	±	0.0087	1451	±	63	1163	±	126	41.06	±	0.89
8308	12.777	±	0.021	9.582	±	0.0088	1419	±	67	1139	±	133	40.89	±	0.92
8309	12.775	±	0.018	9.581	±	0.0097	1428	±	71	1146	±	142	40.99	±	0.97
8310	12.793	±	0.023	9.58	±	0.0084	1420	±	62	1140	±	123	40.96	±	0.87
8311	12.786	±	0.022	9.58	±	0.0088	1387	±	74	1115	±	148	40.79	±	0.98
8312	12.794	±	0.016	9.578	±	0.0089	1287	±	69	1040	±	138	40.31	±	0.92
8313	12.769	±	0.012	9.578	±	0.0089	1259	±	79	1019	±	158	40.17	±	1.01
8335	13.221	±	0.023	10.04	±	0.0062	2166	±	91	1699	±	181	31.93	±	1.12
8336	13.225	±	0.022	10.04	±	0.0061	2128	±	83	1671	±	165	31.72	±	1.03
8337	13.212	±	0.019	10.04	±	0.006	2000	±	79	1575	±	157	31.17	±	0.97
8338	13.228	±	0.047	10.04	±	0.0058	1986	±	74	1564	±	147	31.1	±	0.92
8339	13.198	±	0.012	10.04	±	0.006	1976	±	68	1557	±	136	31.04	±	0.86
8340	13.221	±	0.041	10.04	±	0.006	1981	±	75	1560	±	149	31.07	±	0.93
8341	13.202	±	0.018	10.04	±	0.0062	1977	±	79	1557	±	157	31.04	±	0.97
8342	13.235	±	0.052	10.04	±	0.0062	2035	±	76	1601	±	151	31.25	±	0.94

8343	13.21	±	0.018	10.04	±	0.0059	2042	±	77	1606	±	153	31.33	±	0.95
8344	13.202	±	0.025	10.04	±	0.0061	1891	±	77	1493	±	153	30.66	±	0.94
8345	13.193	±	0.016	10.03	±	0.0061	1870	±	76	1477	±	151	30.59	±	0.93
8346	13.17	±	0.018	10.03	±	0.0057	1713	±	69	1359	±	137	29.94	±	0.84
8347	13.195	±	0.036	10.03	±	0.0058	1697	±	70	1347	±	139	29.81	±	0.85
8348	13.169	±	0.021	10.02	±	0.0055	1553	±	69	1239	±	137	29.23	±	0.82
8349	13.149	±	0.024	10.02	±	0.0056	1531	±	65	1223	±	129	29.15	±	0.78
8350	13.163	±	0.019	10.02	±	0.0055	1522	±	66	1216	±	131	29.12	±	0.79
8351	13.155	±	0.022	10.02	±	0.0054	1520	±	66	1215	±	132	29.15	±	0.79
8352	13.153	±	0.018	10.02	±	0.0057	1520	±	65	1215	±	130	29.15	±	0.78
8353	13.153	±	0.023	10.02	±	0.0056	1372	±	66	1104	±	131	28.5	±	0.77
8354	13.146	±	0.018	10.02	±	0.0056	1378	±	67	1108	±	133	28.54	±	0.78
8355	13.182	±	0.06	10.01	±	0.0054	1362	±	61	1096	±	121	28.5	±	0.72
8356	13.144	±	0.014	10.01	±	0.0052	1368	±	64	1101	±	128	28.54	±	0.75
8357	13.149	±	0.02	10.01	±	0.0056	1366	±	65	1100	±	130	28.52	±	0.76
8358	13.141	±	0.016	10.01	±	0.0056	1369	±	64	1101	±	127	28.54	±	0.75
8359	13.148	±	0.022	10.01	±	0.0059	1363	±	63	1097	±	125	28.51	±	0.74
8246	12.822	±	0.035	9.573	±	0.0116	2445	±	77	1908	±	153	46.77	±	1.15
8247	12.797	±	0.019	9.57	±	0.0111	2341	±	53	1830	±	105	46.31	±	0.91
8248	12.844	±	0.049	9.573	±	0.012	2255	±	59	1766	±	118	45.74	±	0.97
8249	12.764	±	0.003	9.571	±	0.0119	2418	±	55	1888	±	109	46.69	±	0.94
8250	12.803	±	0.051	9.568	±	0.0112	2201	±	90	1726	±	180	45.59	±	1.27
8251	12.803	±	0.017	9.571	±	0.0119	2148	±	75	1686	±	150	45.2	±	1.12
8252	12.758	±	0.017	9.569	±	0.0115	2257	±	57	1768	±	114	45.88	±	0.95
8253	12.782	±	0.003	9.57	±	0.0115	2219	±	71	1739	±	142	45.64	±	1.08
8254	12.763	±	0.015	9.571	±	0.0118	2245	±	75	1758	±	149	45.74	±	1.12
8255	12.768	±	0.025	9.565	±	0.0114	2124	±	66	1668	±	131	45.26	±	1.02
8256	12.791	±	0.022	9.568	±	0.0117	2066	±	71	1625	±	142	44.87	±	1.07
8257	12.765	±	0.016	9.569	±	0.0119	2145	±	93	1684	±	186	45.27	±	1.3
8258	12.815	±	0.069	9.567	±	0.0119	1964	±	59	1548	±	118	44.33	±	0.95
8259	12.772	±	0.033	9.563	±	0.0118	1835	±	66	1451	±	131	43.76	±	0.99
8260	12.741	±	0.006	9.565	±	0.012	1904	±	64	1503	±	127	44.07	±	0.98
8261	12.781	±	0.038	9.564	±	0.0126	1726	±	51	1370	±	102	43.12	±	0.87
8262	12.804	±	0.059	9.561	±	0.0121	1730	±	57	1373	±	114	43.25	±	0.91
8263	12.739	±	0.017	9.559	±	0.0118	1748	±	66	1386	±	131	43.38	±	0.99
8264	12.762	±	0.041	9.56	±	0.0125	1685	±	59	1338	±	117	43.01	±	0.92
8265	12.764	±	0.026	9.56	±	0.0125	1664	±	65	1323	±	130	42.9	±	0.98
8266	12.73	±	0.048	9.557	±	0.0118	1538	±	60	1228	±	119	42.32	±	0.91
8267	12.748	±	0.032	9.555	±	0.0114	1538	±	53	1229	±	106	42.37	±	0.85
8268	12.716	±	0.005	9.555	±	0.012	1437	±	53	1153	±	106	41.84	±	0.85

8269	12.735	±	0.028	9.551	±	0.0119	1346	±	60	1084	±	119	41.46	±	0.89
8270	12.717	±	0.012	9.551	±	0.012	1254	±	52	1015	±	103	40.99	±	0.81
8371	13.681	±	0.038	10.48	±	0.0151	2051	±	72	1613	±	143	21.26	±	0.89
8372	13.629	±	0.011	10.48	±	0.0142	1938	±	77	1529	±	154	20.81	±	0.93
8373	13.623	±	0.02	10.48	±	0.0138	1966	±	71	1550	±	142	20.95	±	0.87
8374	13.643	±	0.045	10.48	±	0.0136	1962	±	66	1546	±	131	20.87	±	0.81
8375	13.628	±	0.009	10.48	±	0.0135	1971	±	60	1553	±	120	20.92	±	0.76
8376	13.594	±	0.017	10.47	±	0.0131	1705	±	79	1353	±	157	19.81	±	0.92
8377	13.578	±	0.07	10.47	±	0.0129	1815	±	73	1436	±	145	20.3	±	0.87
8378	13.598	±	0.016	10.47	±	0.0135	1849	±	68	1462	±	136	20.44	±	0.83
8379	13.624	±	0.061	10.47	±	0.0129	1837	±	57	1453	±	114	20.42	±	0.72
8380	13.637	±	0.049	10.48	±	0.0134	1927	±	66	1520	±	131	20.74	±	0.81
8381	13.629	±	0.008	10.48	±	0.0134	1949	±	69	1536	±	137	20.85	±	0.84
8382	13.653	±	0.022	10.48	±	0.0128	1917	±	76	1512	±	151	20.73	±	0.91
8383	13.593	±	0.026	10.47	±	0.0124	1685	±	72	1338	±	143	19.79	±	0.84
8384	13.578	±	0.065	10.47	±	0.013	1690	±	71	1342	±	141	19.78	±	0.84
8385	13.588	±	0.014	10.46	±	0.0128	1673	±	76	1330	±	152	19.74	±	0.89
8386	13.568	±	0.032	10.46	±	0.0125	1484	±	68	1188	±	135	18.99	±	0.78
8387	13.592	±	0.024	10.46	±	0.0129	1472	±	74	1179	±	148	18.93	±	0.85
8388	13.506	±	0.027	10.45	±	0.0087	1457	±	89	1168	±	178	19.04	±	0.98
8389	13.519	±	0.029	10.45	±	0.0115	1435	±	102	1151	±	203	18.87	±	1.11
8390	13.533	±	0.016	10.44	±	0.0117	1247	±	91	1010	±	182	18.12	±	0.98
8391	13.503	±	0.055	10.44	±	0.0117	1254	±	86	1015	±	171	18.15	±	0.93
8408	13.695	±	0.026	10.58	±	0.0169	1988	±	120	1566	±	240	18.97	±	1.39
8409	13.72	±	0.037	10.58	±	0.0176	1976	±	114	1557	±	228	18.89	±	1.33
8410	13.685	±	0.027	10.57	±	0.0168	1826	±	102	1445	±	204	18.3	±	1.18
8411	13.67	±	0.024	10.57	±	0.0163	1692	±	93	1344	±	185	17.76	±	1.07
8412	13.707	±	0.045	10.56	±	0.0166	1576	±	91	1257	±	181	17.24	±	1.03
8413	13.725	±	0.05	10.56	±	0.0167	1457	±	70	1167	±	139	16.75	±	0.82
8414	13.662	±	0.042	10.56	±	0.016	1472	±	82	1179	±	163	16.85	±	0.93
8415	13.688	±	0.04	10.56	±	0.0161	1463	±	84	1172	±	168	16.81	±	0.95
8416	13.667	±	0.037	10.56	±	0.0159	1406	±	93	1129	±	185	16.57	±	1.03
8417	13.664	±	0.036	10.56	±	0.0163	1406	±	89	1129	±	177	16.58	±	0.99
8418	13.627	±	0.014	10.55	±	0.0159	1336	±	98	1077	±	195	16.31	±	1.07
10398	13.569	±	0.012	10.42	±	0.016	1836	±	67	1452	±	134	21.52	±	0.84
10399	13.506	±	0.07	10.4	±	0.0131	1596	±	65	1272	±	130	20.66	±	0.78
10400	13.473	±	0.041	10.39	±	0.0131	1406	±	64	1130	±	128	19.91	±	0.75
10416	13.477	±	0.019	10.31	±	0.0097	2009	±	54	1581	±	107	24.71	±	0.69
10417	13.48	±	6E-04	10.3	±	0.008	1854	±	50	1466	±	100	24.23	±	0.64

10418	13.446	±	0.006	10.3	±	0.0093	1652	±	53	1314	±	106	23.24	±	0.66
10419	13.386	±	0.064	10.29	±	0.0095	1456	±	56	1167	±	112	22.4	±	0.67
10221	12.941	±	0.021	9.703	±	0.0104	2210	±	143	1732	±	285	41.52	±	1.81
10222	12.935	±	0.002	9.704	±	0.0108	2054	±	127	1616	±	254	40.64	±	1.61
10223	12.948	±	0.022	9.698	±	0.009	1856	±	115	1467	±	229	39.74	±	1.44
10224	12.922	±	0.045	9.696	±	0.009	1735	±	105	1376	±	209	39.15	±	1.31
10225	12.918	±	0.041	9.694	±	0.0096	1641	±	83	1306	±	166	38.7	±	1.08
10226	12.907	±	0.002	9.69	±	0.0089	1479	±	74	1184	±	148	37.96	±	0.96
10232	12.946	±	0.011	9.694	±	0.0095	2158	±	102	1694	±	204	41.5	±	1.34
10233	12.939	±	0.001	9.693	±	0.0085	2038	±	94	1603	±	187	40.88	±	1.23
10234	12.922	±	0.038	9.693	±	0.0081	1934	±	88	1526	±	176	40.31	±	1.16
10235	12.907	±	0.035	9.686	±	0.0076	1714	±	61	1361	±	122	39.34	±	0.85
10236	12.905	±	0.04	9.683	±	0.0066	1545	±	53	1234	±	106	38.51	±	0.75
10252	12.762	±	0.035	9.581	±	0.0332	2095	±	93	1646	±	185	44.6	±	1.6
10253	12.792	±	0.027	9.576	±	0.03	2043	±	78	1607	±	156	44.49	±	1.41
10254	12.792	±	0.024	9.575	±	0.0291	2042	±	82	1607	±	164	44.49	±	1.43
10255	12.782	±	0.032	9.569	±	0.0294	1857	±	68	1468	±	136	43.68	±	1.31
10256	12.774	±	0.045	9.565	±	0.03	1711	±	66	1358	±	131	43.01	±	1.3
10257	12.752	±	0.035	9.56	±	0.027	1596	±	62	1272	±	124	42.55	±	1.2
10258	12.765	±	0.048	9.555	±	0.0264	1480	±	58	1185	±	116	42.06	±	1.15
10268	12.72	±	0.046	9.522	±	0.0328	2003	±	53	1577	±	106	45.99	±	1.33
10269	12.724	±	0.047	9.521	±	0.0332	1928	±	69	1521	±	138	45.6	±	1.44
10270	12.716	±	0.027	9.514	±	0.031	1794	±	73	1420	±	145	45.07	±	1.4
10271	12.723	±	0.037	9.512	±	0.032	1736	±	64	1377	±	127	44.82	±	1.36
10272	12.706	±	0.047	9.506	±	0.0295	1593	±	67	1270	±	134	44.23	±	1.32
10273	12.712	±	0.052	9.504	±	0.0305	1502	±	67	1201	±	133	43.8	±	1.33
8314	12.732	±	0.018	9.555	±	0.0084	300	±	0	300	±	0	36.21	±	0.26
8360	13.085	±	0.031	9.971	±	0.0052	300	±	0	300	±	0	24.55	±	0.14
8271	12.688	±	0.024	9.531	±	0.0128	300	±	0	300	±	0	36.92	±	0.4
8392	13.433	±	0.022	10.39	±	0.0116	300	±	0	300	±	0	14.82	±	0.25
8419	13.554	±	0.035	10.5	±	0.0155	300	±	0	300	±	0	12.55	±	0.31
10401	13.382	±	0.046	10.33	±	0.0124	300	±	0	300	±	0	16.06	±	0.27
10420	13.307	±	0.012	10.25	±	0.0116	300	±	0	300	±	0	17.95	±	0.26
10227	12.842	±	0.023	9.654	±	0.0083	300	±	0	300	±	0	33.21	±	0.25
10237	12.829	±	0.011	9.645	±	0.0073	300	±	0	300	±	0	33.48	±	0.22
10259	12.713	±	0.066	9.513	±	0.0231	300	±	0	300	±	0	37.5	±	0.73
10274	12.674	±	0.034	9.469	±	0.0263	300	±	0	300	±	0	38.91	±	0.85